Louisiana Tech University
Louisiana Tech Digital Commons

Doctoral Dissertations | Graduate School

Summer 2005

Study on poly[2-methoxy-5-(2'-ethylhexyloxy)-1,4-phenylenevinylene] polymer based photodetectors

Difei Qi

Follow this and additional works at: https://digitalcommons.latech.edu/dissertations

 Part of the Electrical and Computer Engineering Commons

Study on poly[2-methoxy-5-(2'-ethylhexyloxy)-1,4-phenylenevinylene] polymer based photodetectors
Qi, Difei
ProQuest Dissertations and Theses; 2005; ProQuest

NOTE TO USERS

This reproduction is the best copy available.

UMI®

Reproduced with permission of the copyright owner. Further reproduction prohibited without permission.

Reproduced with permission of the copyright owner. Further reproduction prohibited without permission.

STUDY ON POLY [2-METHOXY-5-(2'-ETHYLHEXYLOXY)-1,4-PHENYLENEVINYLENE] POLYMER BASED PHOTODETECTORS

By

Difei Qi, M.S.

A Dissertation Presented in Partial Fulfillment
of the Requirements for the Degree
Doctor of Philosophy in Engineering

COLLEGE OF ENGINEERING AND SCIENCE
LOUISIANA TECH UNIVERSITY

August 2005

Reproduced with permission of the copyright owner. Further reproduction prohibited without permission.

UMI Number: 3184191

INFORMATION TO USERS

The quality of this reproduction is dependent upon the quality of the copy submitted. Broken or indistinct print, colored or poor quality illustrations and photographs, print bleed-through, substandard margins, and improper alignment can adversely affect reproduction.

In the unlikely event that the author did not send a complete manuscript and there are missing pages, these will be noted. Also, if unauthorized copyright material had to be removed, a note will indicate the deletion.

UMI®

UMI Microform 3184191

Copyright 2005 by ProQuest Information and Learning Company.

All rights reserved. This microform edition is protected against unauthorized copying under Title 17, United States Code.

ProQuest Information and Learning Company
300 North Zeeb Road
P.O. Box 1346
Ann Arbor, MI 48106-1346

Reproduced with permission of the copyright owner. Further reproduction prohibited without permission.

APPROVAL FOR SCHOLARLY DISSEMINATION

The author grants to the Prescott Memorial Library of Louisiana Tech University the right to reproduce, by appropriate methods, upon request, any or all portions of this Dissertation. It is understood that "proper request" consists of the agreement, on the part of the requesting party, that said reproduction is for his personal use and that subsequent reproduction will not occur without written approval of the author of this Dissertation. Further, any portions of the Dissertation used in books, papers, and other works must be appropriately referenced to this Dissertation.

Finally, the author of this Dissertation reserves the right to publish freely, in the literature, at any time, any or all portions of this Dissertation.

Author Dilei Qi

Date 07/27/2005

GS Form 14
(5/03)

Reproduced with permission of the copyright owner. Further reproduction prohibited without permission.

ABSTRACT

This thesis is dedicated to the development of novel and efficient polymer photodetectors based on MEH-PPV conjugated polymers. The polymer-based photodetectors have the advantages of easy processing, low weight, and low cost, and thus are promising candidates for future generations of photodetectors. At present, the quantum efficiency of polymer photodetectors is still low and not comparable to inorganic photodetectors. Therefore, in this thesis we explore ways to enhance the quantum efficiency of polymer photodetectors by using different electron donors, configurations, and implementation of the diffraction optical grating into photodetector structure. We designed, fabricated, and characterized several original types of devices: Poly[2-methoxy-5-(2'-ethylhexyloxy)-1,4-phenylenevinylene](MEH-PPV)/ethyl viologen dibromide (EVD) blended photodetectors, MEH-PPV/PbSe quantum dots (QD) blended photodetectors, MEH-PPV/PCBM blended photodetectors, and MEH-PPV/PCBM blended photodetectors integrated with grating structure.

MEH-PPV/EVD blended photodetectors show a double increase in the external quantum efficiency (EQE) as compared to pure MEH-PPV devices due to ultra fast charge transfer by EVD dication. MEH-PPV/PbSe blended photodetectors demonstrate gain (EQE>1) for electric fields $E \sim 7\times10^5$ V/cm, which are comparable to inorganic photodetectors. To the best of our knowledge, we were the first to report the gain observed in polymer/nanocrystal photodetectors. The observed photocurrent gain could

Reproduced with permission of the copyright owner. Further reproduction prohibited without permission.

be attributed to the carrier multiplication in PbSe nanocrystal quantum dots via multiple exciton generation. We also designed a novel MEH-PPV/PCBM photodetector with two blended layers to enhance carrier-transport path. Such a photodetector shows a double increase in the external quantum efficiency compared to the device with only a single blended layer. Lifetime and degradation measurements have shown that the estimated lifetime of devices is from19-23 days.

Furthermore, we introduce the diffraction grating into the polymer photodetectors to improve light absorption of the devices. Unfortunately, we did not observe any significant enhancement of the external quantum efficiency in MEH-PPV/PCBM photodetectors with grating structures compared to devices without the grating. However, we have laid the initial background for future work, such as thereotical investigation, grating structure optimization, and nano-size patterning on polymer with soft lithography.

We also investigated the anisotropy of conjugated polymer optical properties with ellipsometry, which is important in designing and optimizing optoelectronics with light direction selection, such as lasing, waveguide, and the devices with grating structures.

In addition, we first established an analytical model with field dependence for the photocurrent action of a pure MEH-PPV photodetector and obtained a good fit to the measured photocurrent density. Furthermore, we used a commercial software package, TAURUS (designed mainly for inorganic semiconductors), to simulate the dark and light I-V curve for a pure polymer photodetector. We found that the simulated dark and light I-V curve of the MEH-PPV photodetector is in a good agreement with measured data at an electric field $> 2\times10^5$ V/cm.

Reproduced with permission of the copyright owner. Further reproduction prohibited without permission.

LOUISIANA TECH UNIVERSITY

THE GRADUATE SCHOOL

July 26, 2005
Date

We hereby recommend that the dissertation prepared under our supervision by DIFEI QI entitled STUDY ON POLY [2-METHOXY-5-(2'-ETHYLHEXYLOXY)-1,4-PHENYLENEVINYLENE] POLYMER BASED PHOTODETECTORS be accepted in partial fulfillment of the requirements for the Degree of DOCTOR OF PHILOSOPHY IN ENGINEERING

Sandra Selmic
Supervisor of Dissertation Research

Ray Sterling
Head of Department

Engineering and Science
Department

Recommendation concurred in:

Advisory Committee

Approved:
Director of Graduate Studies

Approved:
Dean of the Graduate School

Dean of the College

GS Form 13
(5/03)

Reproduced with permission of the copyright owner. Further reproduction prohibited without permission.

TABLE OF CONTENTS

Reproduced with permission of the copyright owner. Further reproduction prohibited without permission.

Reproduced with permission of the copyright owner. Further reproduction prohibited without permission.

Reproduced with permission of the copyright owner. Further reproduction prohibited without permission.

LIST OF TABLES

Reproduced with permission of the copyright owner. Further reproduction prohibited without permission.

LIST OF FIGURES

Reproduced with permission of the copyright owner. Further reproduction prohibited without permission.

Reproduced with permission of the copyright owner. Further reproduction prohibited without permission.

Reproduced with permission of the copyright owner. Further reproduction prohibited without permission.

Reproduced with permission of the copyright owner. Further reproduction prohibited without permission.

Reproduced with permission of the copyright owner. Further reproduction prohibited without permission.

Reproduced with permission of the copyright owner. Further reproduction prohibited without permission.

ACKNOWLEDGEMENTS

I would like thank my advisor, Dr. Sandra Selmic, for her help and advice for the last three years. Her advice was most valuable for understanding the experimental results and to determine the next steps for the research presented in this thesis.

I would like thank Dr.Marija Drndic, a professor of University of Pennsylvania, for useful discussion and suggestions.

I would like to Dr. Haifeng Ji, Dr.Yuri Lvov, Dr. Mike McShane, and Dr. Kody Varahramyan for providing the opportunity of using their lab equipment and providing their advice.

I would like to thank all my committee members, Dr. Sandra Selmic, Dr.Yuri Lvov, Dr. Haifeng Ji, Dr. Rastko Selmic, and Dr. Kody Varahramyan, who gave me their precious advice.

I would like to thank David Keith Chambers, Jie Liu, Srikanth, Joey Cannon, and Zhenchun Liu, and Fengliang Xue for helpful discussions and fabrication support.

The staff in IFM has been the backbone of my researches, especially Ji Fang, Karen Xu, Dee Tatum, John McDonald, and Scott Williams, for measurements and operation of equipment.

I would like to thank my great parents, who gave me life and encourage me to travel farther on the research road, and my loving husband Quandou and daughter. Their love and support allows me to go farther.

Reproduced with permission of the copyright owner. Further reproduction prohibited without permission.

ABBREVIATION AND SYMBOLS

MEH-PPV: Poly[2-methoxy-5-(2'-ethylhexyloxy)-1,4-phenylenevinylene]

P3HT: Poly(3-hexylthiophene)

PDMS: Polydimethylsiloxane

PEDOT: PSS: Poly(2,3-dihydrothieno(3,4-b)-1,4-dioxin/Poly(styrenesulfonate)

ITO: Indium Tin Oxide

PCBM: [6,6]-phenyl C61 butyric acid methyl ester

EVD: ethyl vilogen dibromide

EQE: External quantum efficiency

IQE: Internal quantum efficiency

D: Electron donor

A: Electron acceptor

PVs: photovoltaics

MQW: Multiple quantum well

QD: quantum dot

LED: light emitting diode

PPV: Poly[p-phenylene-vinylene]

TE mode: transverse electric mode

TM mode: transverse magnetic mode

IP: Ionization potential

Reproduced with permission of the copyright owner. Further reproduction prohibited without permission.

CHAPTER 1

MOTIVATION AND OUTLINE

The goal of this research is to develop novel photodetectors based on conjugated polymers. Our approach consists of investigating several polymer materials and the design, fabrication, and characterization of photodetectors, establishing an analytical model for photogenerated current, and simulating the electrical characteristics of a pure polymer photodetector.

In Chapter 2 we review the history, classification and operating principles of typical inorganic photodetectors. Then, we introduce organic materials and conjugated semiconducting polymers and their applications. In order to understand the underlying mechanism of polymer photodetectors, we describe the basic concept of excitones as related to photoconductivity and loss mechanisms in polymer photodetectors. In addition, we provide the list of typical polymer processes and characteristics of photodetectors.

In Chapter 3 we describe the fabrication and experimental results of poly [2-methoxy-5-(2'-ethylhexyloxy)-1,4-phenylenevinylene] and ethyl dibromide viologen (MEH-PPV/EVD) photodetectors, which are sensitive to the visible light spectrum. The thicknesses of the active polymer-organic thin films were approximately 70 nm. These polymer-organic blend photodetectors have shown a double increase in the external quantum efficiency as compared to pure MEH-PPV devices. The increase in

Reproduced with permission of the copyright owner. Further reproduction prohibited without permission.

photoconductivity of blended MEH-PPV/EVD devices may be due to ultra fast charge transfer by EVD dication. The breakdown voltage depends on the EVD concentration and ranges between -12V and -20V. Hysteresis behavior was observed in the studied devices and could be due to charge trapping.

Quantum dots are attractive to many researchers for application to optoelectronics due to quantum confinement. In Chapter 4, we have realized highly efficient photodetectors based on composites of the semiconducting polymer MEH-PPV and PbSe nanocrystal quantum dots. The external quantum efficiency in these devices is greater than 1 for electric fields $E \sim 7\times10^5$ V/cm. The observed photocurrent gain could be attributed to the carrier multiplication in PbSe nanocrystal quantum dots via multiple exciton generation, and the efficient charge conduction through the host polymer material. This photocurrent gain is observed only when the PbSe nanocrystal bandgap is at least three times larger than the energy gap of the active polymer material.

In Chapter 5 we fabricate MEH-PPV/ PCBM photodetectors based on an electron donor-acceptor dispersed heterostrucutre. In the section, we used two configurations, one is single blended layer (SBL) and the other is double blended layer (DBL). In SBL there is only one MEH-PPV-rich layer sandwiched between ITO and AL. However, in DBL there is a MEH-PPV-rich layer at the ITO side and a PCBM-rich layer at the Al side. The DBL structure is expected to establish an efficient charge carrier transferring path and thus enhances the external quantum efficiency (EQE) of the polymer photodetectors or solar cells.

In order to increase the quantum efficiency of photodetectors, we have researched a novel photodetector design with an optical grating structure inside the device. For the

Reproduced with permission of the copyright owner. Further reproduction prohibited without permission.

investigation and theoretical simulation of diffraction efficiency, we need to know and understand the optical properties, like the index of refraction and the extinction coefficient. Therefore, we performed the ellipsometry measurement of conjugated polymers like MEH-PPV and P3HT and described the relevant ellipsometric measurement data in Chapter 6. In addition, we obtained other important electrical properties such as the dielectric constant from the complex index of refraction. The dielectric constant enables us to enlarge our understanding of polymer electronic structure and photoconductivity.

Chapter 7 introduces the theory of the diffraction grating and grating fabrication techniques. We used Morf's formulation of lamellar grating as a theoretical model. Further, we developed the MathCad program for the given model (see Appendix A). By optimizing the grating depth and period, we maximized the diffraction efficiency of the first diffractive mode, which was expected to increase the optical path and then the optical absorption of the active polymer. The grating structures was designed and fabricated at the interface of ITO and PEDOT: PSS. The master mold of lamellar grating was first fabricated hollographically on the silicon substrate. Then the grating pattern was transferred to a PDMS mold with high precision. Now we can use the PDMS mold to pattern the PEDOT: PSS layer or conjugated polymer layer by soft lithography. The testing results were also given and discussed in this chapter.

Later on in Chapter 8, a theoretical model based on the exciton diffusion process and boundary conditions was derived for the photocurrent generation of intrinsic MEH-PPV polymer photodetectors in single-layer configuration. In this model, we also introduced the concept of field-dependent exciton dissociation efficiency. The calculation

Reproduced with permission of the copyright owner. Further reproduction prohibited without permission.

based on this model fits well to the measured photocurrent density. In addition, we simulated dark I-V and light I-V curve with T-CAD (TAURUS). A good simulation of dark I-V curve in the higher electric field was reached by setting up a Poole-Frenkel-like mobility model with the Physical Model and Equation Interface (PMEI) in TAURUS. For the simulation of light I-V curve, the exciton diffusion model derived before was replaced with the electron continuity equation with related exciton parameter values. Furthermore, we discussed other parameters significant for the electrical characteristics in the dark, such as density of states, zero-field mobility, mobility field dependence factor, work function of Al, and electron affinity of polymer.

Reproduced with permission of the copyright owner. Further reproduction prohibited without permission.

CHAPTER 2

BACKGROUND ON POLYMER PHOTODETECTORS

2.1 Inorganic Semiconductor Photodetectors

A photodetector is an electronic component which converts an optical signal into an electrical signal. Photodetectors are widely used in spectroscopy, photography, analytical instrumentation, optical position sensors, beam alignment, surface characterization, laser range finders, optical communication, and medical imaging systems. The photodetector structures are mainly classified into PN and PIN photodetectors [1]-[3], Schottky [5], avalanche photodetectors (APDs) [6]-[8], and quantum well (QW) photodetectors [9]-[13].

A typical PN photodetector, shown schematically in Fig.2-1, features a two-electrode, radiation-sensitive PN junction formed in a semiconductor material. The reverse current varies with illumination. A typical PIN photodetector has a large intrinsic region sandwiched between P-doped and N-doped semiconducting regions as shown in Fig.2-2. Photons absorbed in this region create electron-hole pairs that are then separated by an electric field, thus generating an electric current in a load circuit. The intrinsic region is relatively free of carrier concentration and results in an extended depletion region, which considerably enhances the quantum efficiency of the PIN photodetectors when compared to PN photodetectors.

Reproduced with permission of the copyright owner. Further reproduction prohibited without permission.

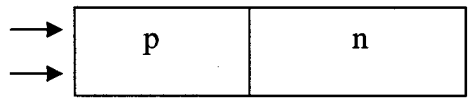

Fig.2-1 The schematic principle of a PN photodetector.

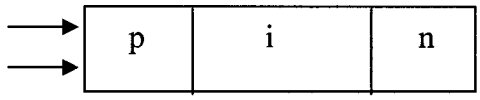

Fig.2-2 The schematic principle of a PIN photodetector.

In Fig.2-3, a Schottky barrier is formed between a metal and a semiconductor. The depletion region in the Schottky barrier is similar to the standard p-n junction. The Schottky photodetector is in either a metal-semiconductor (surface) or lateral metal-semiconductor-metal (MSM) configuration. Avalanche photodetectors (APDs) as shown in Fig.2-4 are photodetectors that can be regarded as the semiconductor analog to photomultipliers. Avalanche breakdown is due to impact ionization. Under a small reverse bias, the diode is almost non-conducting, although a very small saturation current still flows. When the reverse electric field across the p-n junction is large enough, the energy of the few electrons flowing is enough to ionize atoms in the silicon. The ionization process is self-reinforcing, causing a rapid increase in current. Avalanche breakdown is not destructive, as long as the diode is not allowed to overheat. The higher the reverse voltage the higher the gain. APDs therefore are more sensitive compared to other semiconductor photodetectors. If very high gain is needed (10^5 to 10^6), a reverse voltage above the APDs breakdown voltage can be applied if the current is limited to below the APDs latching current. This is particularly useful for single photon detection.

Reproduced with permission of the copyright owner. Further reproduction prohibited without permission.

The avalanche photodetector is characterized by high gain and could detect low-level irradiative particles, like gamma ray.

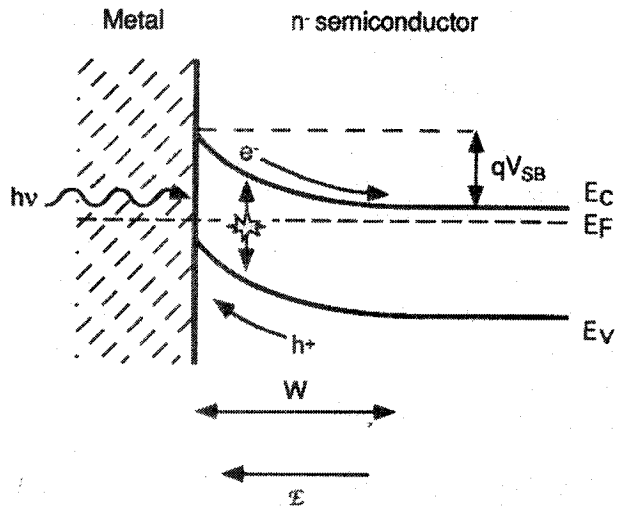

Fig.2-3 The schematic layout of a Schottky photodetector.

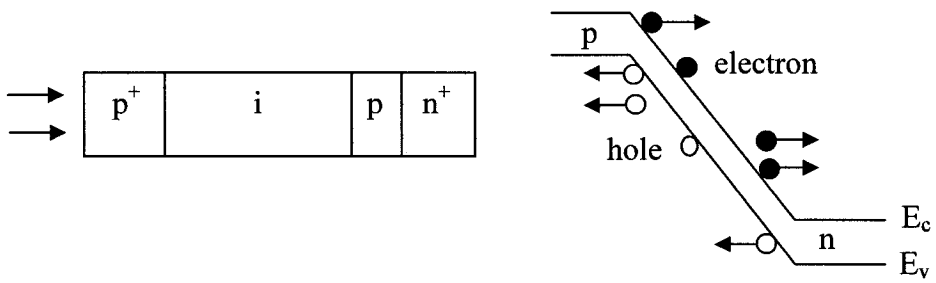

Fig.2-4 The schematic principle of a APD photodetector.

Quantum well (QW) photodetector is a layered structure with layer thicknesses controlled within about one atomic layer. When layers are made with thicknesses of about 10 nm or smaller, the resulting confinement of the electron (or hole) wavefunction leads to strong quantum-mechanical effects. Such a structure is also called a heterostructure. The quantum well is a sandwich made of a thin (e.g.≤10nm) layer of a narrow-bandgap semiconductor, surrounded by two wider-bandgap semiconductor layers. The narrow bandgap layer of the quantum-well structure shown in Fig.2-5 is a "potential

Reproduced with permission of the copyright owner. Further reproduction prohibited without permission.

well" for electrons and holes. This structure is approximated quantitatively through the "particle in a box" or "infinite quantum well" model. The QW structure can lead to the enhancement of device performance. The QW photodetectors are developed for infrared (IR) imaging systems that operate in the very long wavelength IR region (mid-IR 3–8 μm, long-IR 8–15 μm, far-IR 15–1000 μm). Presently, the QW photodetectors have widely been used for the long-distance telecommunications or for the space applications like monitoring the global atmospheric temperature profiles.

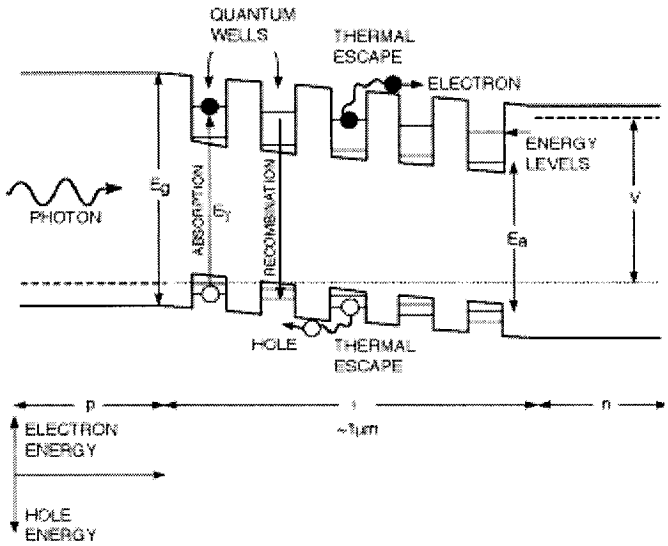

Fig.2-5 The schematic principle of a multiple quantum well photodetector.

Fig.2-6 shows the room-temperature absorption spectra widely used in photodetectors. The photodetector spectral response can be measured for X-ray, UV, visible, or IR. Typically, silicon photodetectors can be sensitive to light from 400nm to 1050nm. The GaAs/AlGaAs is perhaps the best known and most mature technology. GaAs is useful as a detector for near-infrared wavelength (<850nm) and has a sharper increase in absorption than Si due to its direct bandgap. The quaternary material, $In_{1-x}Ga_xAs_{1-y}P_y$, can also absorb near-IR light, such as 0.92 μm for InGaAsP and 1.65 μm for

Reproduced with permission of the copyright owner. Further reproduction prohibited without permission.

$In_{0.53}Ga_{0.47}As$. The PbSe absorbs from about 1 μm to 5 μm, in which InAs and InSb are also useful. And HgCdTe is an additional optical material for mid- and far-infrared photodetectors.

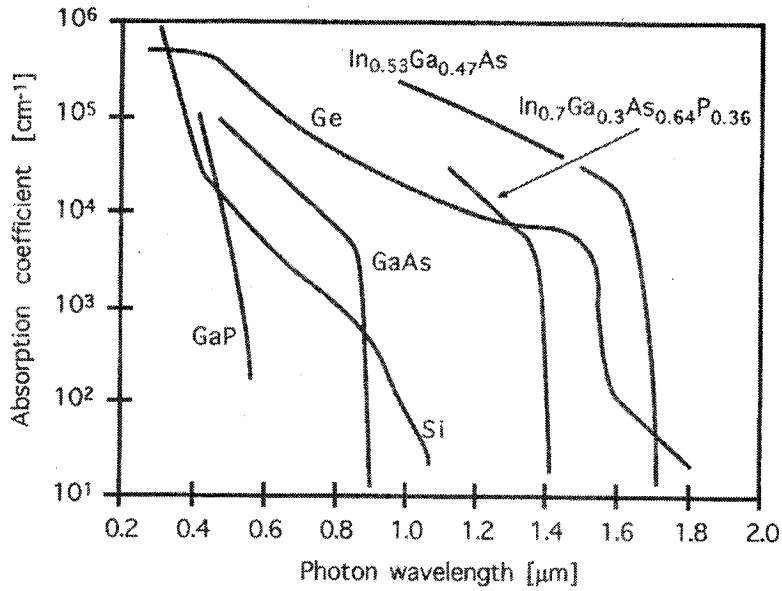

Fig.2-6 Room-temperature absorption spectra for several semiconducting materials used in photodetectors (Ref.[14]).

2.2 Conduction of Conjugated Polymers

Traditionally, polymers have been considered and applied as insulators in the electronics industry. Since then, electronically conducting materials are referred to as conjugated polymer, with framework of alternating single and double carbon-carbon (or carbon-nitrogen) bonds. Single bond is referred to as a σ-bond while the double bond consists of a σ –bond and a π-bond. All conjugated polymers have a σ-bond backbone of overlapping sp^2 hybrid orbitals as shown in Fig.2-7. The remaining out-of-plane p_z orbitals on the carbon (or nitrogen) atoms overlap with neighboring p_z orbitals to give π-bonds. In reality, the conduction of polymer results from the delocalization of the electrons in the π-bond over the entire molecule as shown in Fig.2-8.

Reproduced with permission of the copyright owner. Further reproduction prohibited without permission.

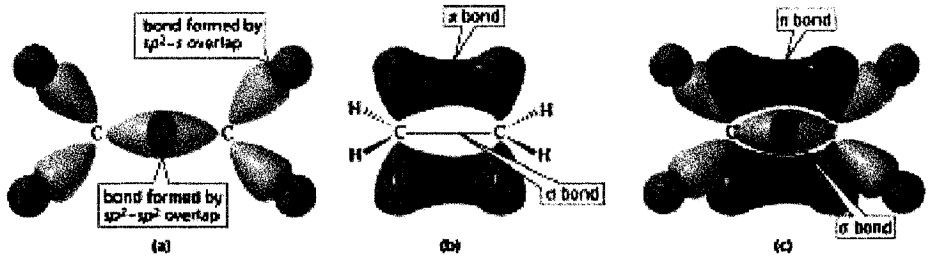

Fig.2-7 Illustration of σ-bond and π-bond in ethylene (C=C). (a) The "backbone" structure consisting of σ bonds formed from the three sp_2-hybridized orbitals on each carbon. (b) The π bonding system formed by overlap of the unhybridized *pz* orbital on each carbon. (c) A view of the combined σ and π system (Ref.[15]).

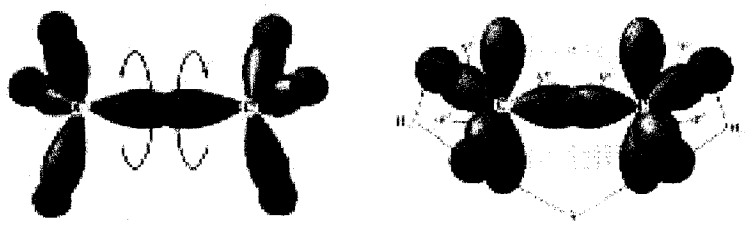

Fig.2-8 The movements of σ bonds and π bonds. σ bond symmetric about the x-axis of the molecule allows the free rotation of the two joined atoms. π bond prevents this rotation. Its electron localization of conjugated π bond can induce the electrical conductivity of conjugate polymers (Ref.[15]).

The common conjugate polymers are given in Fig.2-9.

Reproduced with permission of the copyright owner. Further reproduction prohibited without permission.

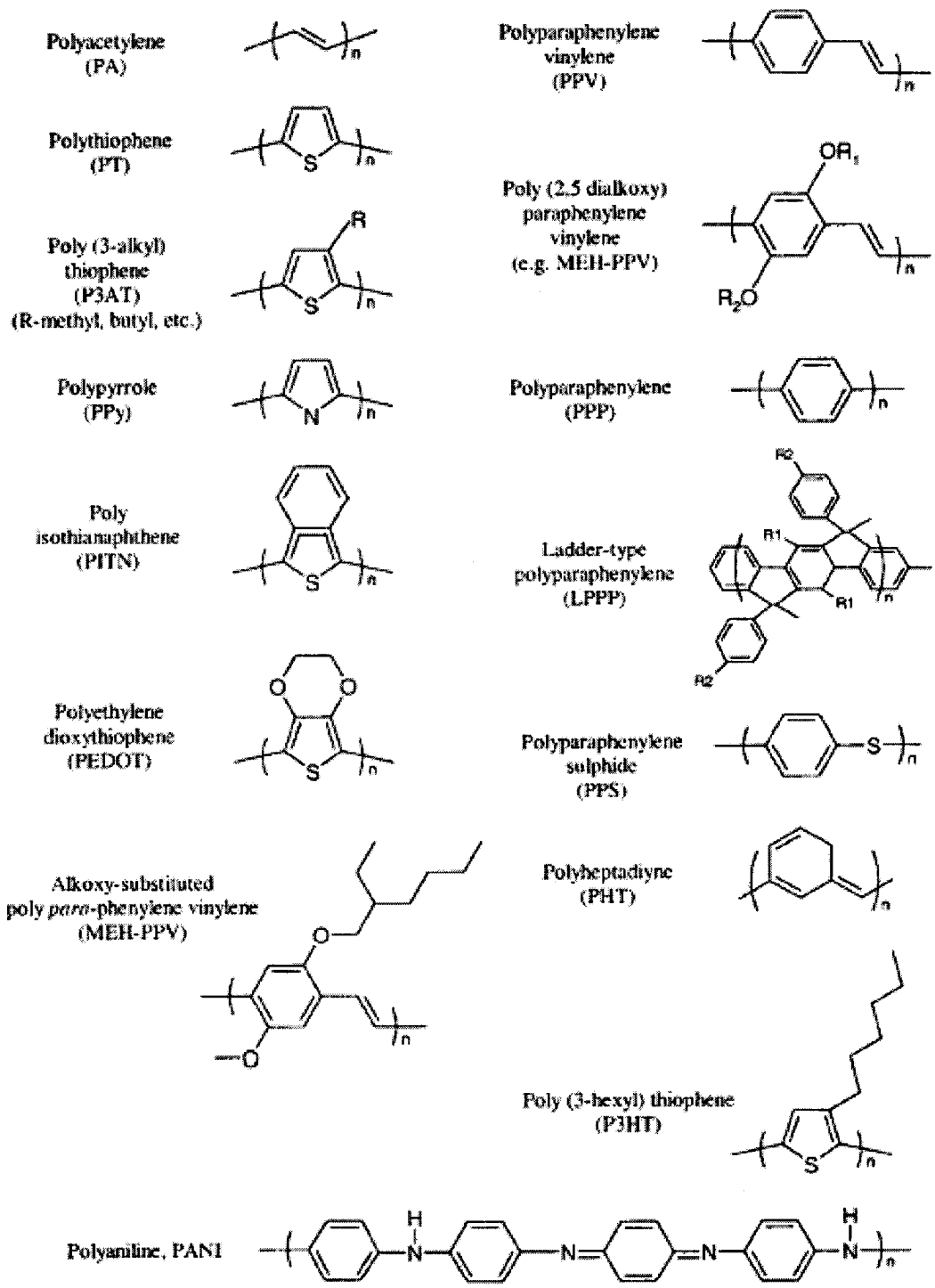

Fig.2-9 The widely used conjugate polymers.

The bandgap of most semiconducting materials typically lie between 0.1eV and 2.2eV. Such energy bands are comparable to the energies of photons falling into the

Reproduced with permission of the copyright owner. Further reproduction prohibited without permission.

visible spectrum. This property indicates their potential application to displays and photovoltaics.

In 1990, the Cambridge group first reported the light emission of LEDs from the polymer sandwiched with two electrodes [16]. This provided a new milestone for polymer-based LEDs for display and other applications. In LEDs, the injected hole from a cathode and injected electron from an anode recombine to produce luminescence with a peak wavelength $\lambda[nm] = 1240 / E_g$ [eV], where E_g is the bandgap of the conjugated polymer. Two years later, the Santa Barbara group reported the first results on polymer-based photovoltaic cells [17][18]. Photovoltaic cells (PVs), also called solar cells, work at zero bias voltage. In photovoltaic cells, an exciton is generated upon the absorption of an incident photon. Under the built-in potential field between two electrodes with asymmetric work function, the exciton is disassociated into a free charge carrier: hole and electron and collected by two electrodes. Due to low cost and easy processing, polymer based optoelectronic devices are currently a very active research area.

The importance of semiconducting polymers was stressed by awardees of the 2000 Nobel Prize in Chemistry: Dr. Heeger, Dr. Shirakawa and Dr. MacDiarmid. Since the last decade, research has focused on the application of soluble and intrinsically semiconducting polymers as active polymers in the field effect transistor (FET) [19], light-emitting diodes (LEDs) [20] [21], photodetectors [22], photovoltaics [23][24], sensors [25], and lasers[26][27]. In addition to being a good device, polymers can be deposited by inexpensive techniques, such as spin-casting, ink-jet printing [28][29], soft lithography [30], screen printing [31], and micromolding [32] onto almost any type of substrate, including flexible tpes like polyethyleneterephthalate (PET) substrates.

Reproduced with permission of the copyright owner. Further reproduction prohibited without permission.

2.3 Excitons

When light is incident on a semiconducting polymer, an exciton, a bound electron-hole pair, is generated due to photon absorption. The binding energy comes from the attractive Coulomb interaction. The exciton can transport energy, but not charge. The excitons are unstable with respect to the ultimate recombination process, if the electron relaxes into the hole. Excitons can also form complexes, such as biexciton, from two excitons.

The binding energy of excitons of polymer was reported from several kTs, 0.3-0.4eV and up to 1eV [32]-[37]. The binding energy of an exciton is equal to the difference between the energy required to create the exciton and the energy to create a free electron and a free hole, Fig.2-10.

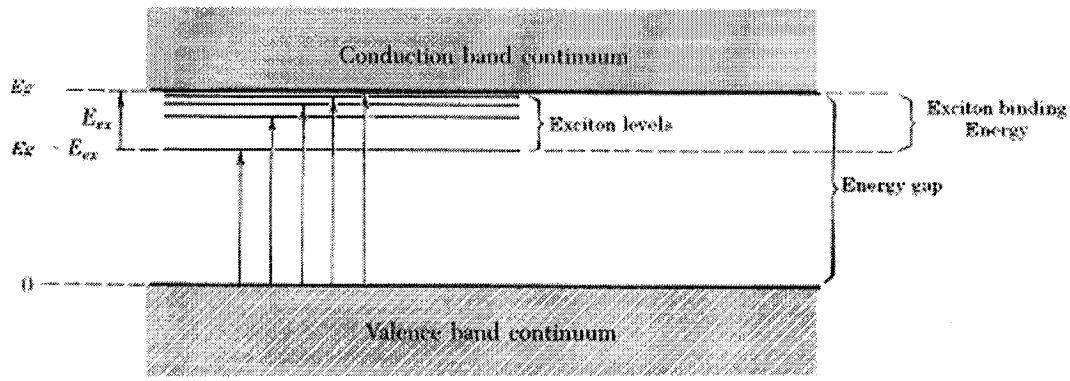

Fig.2-10 The energy levels of an exciton created in a direct process. $E_b=E_g-E_{ex}$ (Ref.[38]).

There are two kinds of excitons: Frenkel exciton and Mott-Wannier exciton [38]. The Frenkel exciton is a kind of tightly bound exciton and excitation is localized on or near a single atom. In a molecular crystal, the covalent binding within a molecule is strong compared to Van der Waals binding between molecules. Therefore the excitons in

Reproduced with permission of the copyright owner. Further reproduction prohibited without permission.

molecular crystal like MEH-PPV are Frenkel excitons [38] . The Mott-Wannier excitons are weekly bound excitons.

When incident photon energy is greater than the polymer bandgap, a free hole and a free electron will be generated with high efficiency, but they will be ultrafast bound together again. If the exictons cannot be dissociated into free charge carriers and transported away, they will recombine or annihilate beyond its lifetime. In the section below we will discuss how to enhance the exciton dissociation or splitting, and finally we can realize the goal of improving the quantum efficiency of photodetector.

2.4 Loss Mechanism

There are five primary steps in a photocurrent generation in photodetectors: optical absorption, exciton diffusion, exciton dissociation, charge transport or transfer, and charge collection, as shown in Fig.2-11.

1. **Absorption of photons**: In most semiconducting polymer detectors only a small part of the incident photons can be absorbed due to the limited thickness of the polymer layer and reflection loss. The low charge carrier motilities of polymer require layer thickness to be in the order of 100nm. For example, a 100nm MEH-PPV layer can only absorb ~79% of incident light at 500nm, and 100nm P3HT can absorb 80% of incident light at 510nm.

Reflection losses are probably another significant factor. According to the reflection calculation $R = [(n_1 - n_2)^2 + k^2]/[(n_1 + n_2)^2 + k^2]$, the reflection R between the glass and the ITO is ~0.018. This means that 1.8% of incident photons will be lost due to the difference of the refractive indices of glass and ITO (n_{glass}=1.5, n_{ITO}=1.95). Also the reflection loss between ITO and MEH-PPV for 500nm light, if there is no intermediate

Reproduced with permission of the copyright owner. Further reproduction prohibited without permission.

layer, is ~3.4%. The reflection loss will increase with the layer number. The scattering incurred from surface morphology and interference effects in a thin-film can not be ignored in optical absorption.

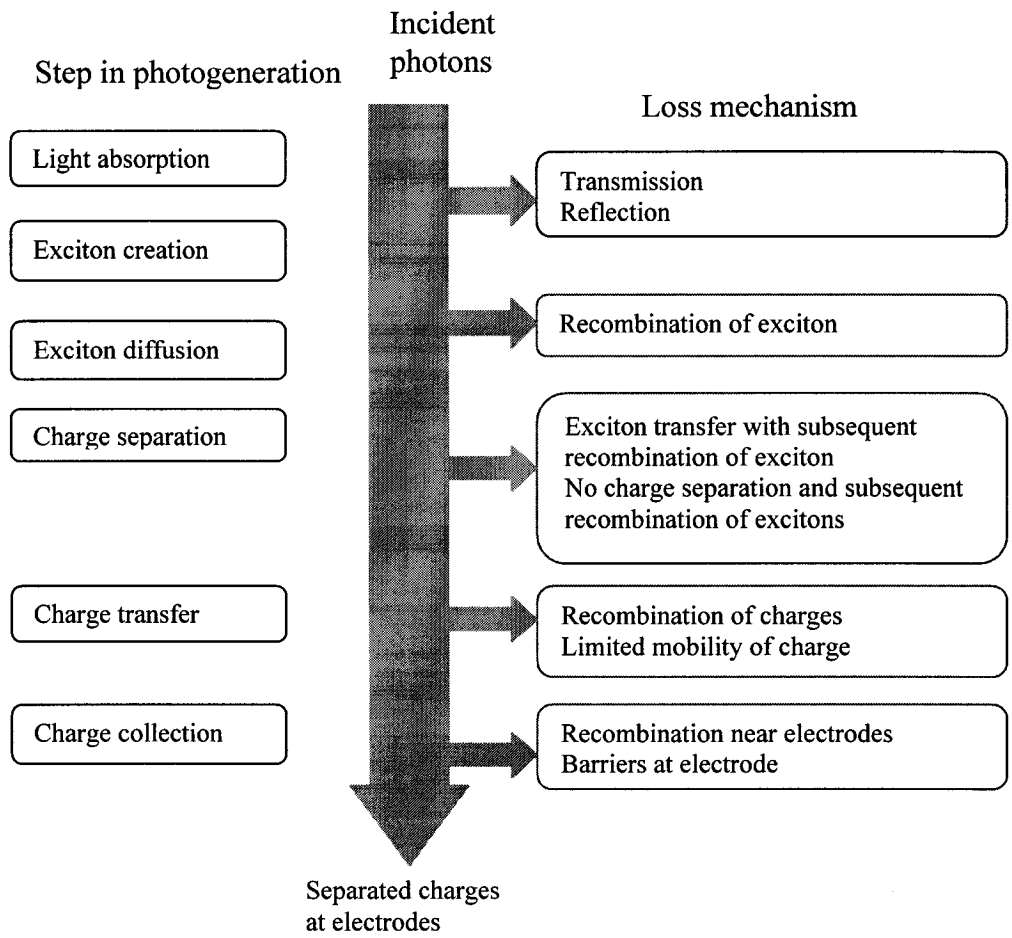

Fig.2-11 The loss mechanism of polymer photodetectors or solar cells (Ref.[39]).

2. **Exciton diffusion**: Ideally, all photoexcited excitons should reach a dissociation site before recombination. The dissociation sites can be the interface between electrode and polymer, interface between D/A, or impurities. Exciton diffusion in semiconductive polymers is shorter than optical absorption length, e.g. exciton diffusion length of MEH-PPV are typically around 20nm [40] . Thus, the device needs to be

Reproduced with permission of the copyright owner. Further reproduction prohibited without permission.

optimized such that the active layer thickness is close to the diffusion length of the polymer. However, such thickness will greatly sacrifice the light absorption and device yield.

3. **Charge separation**: Charge separation is known to occur at organic semiconductor/metal interfaces, impurities (e.g. oxygen) or electron donor-acceptor junction and defects. The electron donor should have a low ionization potential and the electron acceptor should have a high electron affinity. A bad interface and defects may work as traps or recombination sites.

4. **Charge transport**: The transport of charge carriers is affected by recombination and transport path when traveling to the electrode. For a pure polymer device, this step is ignored because the two interfaces near the contacts are exciton dissociation sites. All charge carriers inside the film are vanishing due to recombination. For D-A polymer devices, the polymer serves as a light-absorber and hole-transporting material, while the acceptor mainly acts as an electron-transporting material. The dissociated charge carriers at the D-A interface need to transport to the contacts for collection. For the non-annealed MEH-PPV film, the hole mobility is in order of 10^{-7} cm^2/V-s, two orders higher than the electron mobility [40]. It is widely accepted that MEH-PPV works like a p-type semiconductor.

5. **Charge collection**: In the structure of polymer photodetectors, the electrode close to the glass substrate (bottom electrode) must be transparent or semitransparent to allow light penetration. Transparent and conductive Indium Tin Oxide (ITO) has been widely used as a bottom-electrode in photodetectors, solar cells and LEDs. For photodetectors and PVs, the workfunction (4.8eV) of ITO requires a low workfunction

Reproduced with permission of the copyright owner. Further reproduction prohibited without permission.

metal as the top-electrode, such as Al (4.28eV), Ca (2.87eV), Mg (3.66eV), and Ag (4.26eV)[42], which can lower the Schottky barrier height. However, the atmospheric stability is another important factor for the choice of top-electrode in our experiment. Oxygen impurity in the interface can form a deeper trapping site and thus affect collection efficiency. In this thesis, we use aluminum as top electrode (cathode) due to low cost and stability in air.

2.5 Operation Principle

There are two main kinds of structures in polymer photodetectors: homojunction and heterojunction: The simplest planar structure is a layer of active polymer layer sandwiched between two different conducting contacts, typically indium tin oxide (ITO) and a low work function metal such as Al, Ca, or Mg, as schematically illustrated in Fig.2-12(a). The difference in anode and cathode work functions provides an electric field to dissociate the excitons and drive the charge carriers toward the contacts, as shown in Fig.2-12(b). For the application of photodetectors, a reverse bias is applied to enhance the quantum efficiency. Single layer solar cells of this type deliver low quantum efficiency (QE) of less 1%.

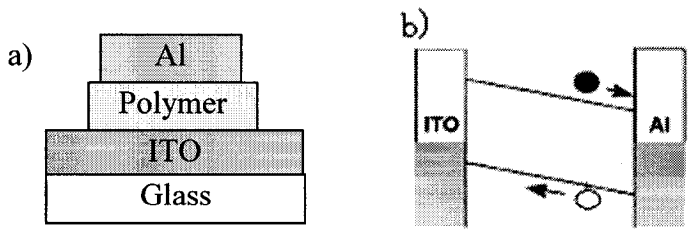

Fig.2-12 (a) Homojunction or single layer structure of a polymer photodetector; (b) The schematic diagram of the photodetector principle of operation.

Reproduced with permission of the copyright owner. Further reproduction prohibited without permission.

Other structures are the heterojunction (bilayer structure) and the dispersed heterojunction (or blend) shown in Fig.2-13(a) and (b). The most progress in polymer photodetectors has been made by heterojunctions. The electron donor with low ionization potential and an electron acceptor with high electron affinity form the heterojunction. The built-in potential in the heterojunction is strong and may split photogenerated excitons, as shown in Fig.2-13(c).

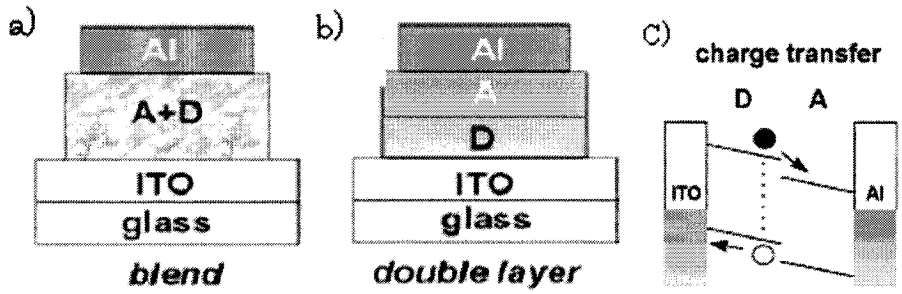

Fig.2-13 (a) Dispersed heterojunction structure or blended structure; (b) Heterojunction or bilayer structure; (c) The principle of operation diagram for heterojunction or dispersed heterojunction photodetector.

2.6 Processing Techniques

Because of the low charge mobility in polymers, the polymer thickness in photodetectors should be very thin in the order of ~100nm or less. The typical thickness of pure MEH-PPV polymer devices is around 100nm. The increase in the polymer film thickness will reduce the quantum efficiency of the device. In the blended or bilayer structure, the thickness of the blended polymer film can increase up to double the thickness of pure MEH-PPV thin film. Good quality thin polymer film is very important to the characteristics of polymer-based photodetectors, like increasing the breakdown voltage and reducing current leakage.

Reproduced with permission of the copyright owner. Further reproduction prohibited without permission.

There are some typical processes, which are widely used for the fabrication of thin polymer film. The process can be spin-casting [43]-[45], dip-coating, doctor-blading, inkjet printing, self-assembly [46][47][48], screen-printing [49] , Langmuir-Blodgett (LB) method, organic molecular beam epitaxy (MBE) etc.

Spin-coating has been accepted as the best coating method for obtaining a film with typical thickness 30-2000nm. Spin-coated films are uniform in thickness and smooth over large areas. The thickness and uniformity of polymer film can be controlled by controlling the concentration of polymer solution, spinning speed, molecular weight and used type of solvent used[43]-[45]. In general, the roughness of the polymer film surface changes with the choice of solvents. Fast atmospheric evaporation of chloroform, due to relatively low boiling point (62°C), produces a much rougher surface polymer film. However, chlorobenzene with high boiling point evaporates slowly and assists the formation of a smooth polymer film [43][44].

Dip-coating is a very simple process that binds a polymer solution to a substrate. The film is obtained by direct immersion of the substrate into the polymer solution. It is easier and faster, but produces less uniform thin films than spin-casting.

Ink-jet printing is a fabrication method in which the polymer solution is printed onto a heated substrate with a printer head of a certain diameter. One drop of polymer solution can define the size of a pixel. This technique is a future technique for the fabrication of an electronic circuit or a LED display.

Self-assembly is a thin-film fabrication technique when layers of oppositely charged polycations and polyanion are alternated via primary electrostatic force and covalent force. A well cleaned substrate is immersed into a dilute aqueous solution of a

Reproduced with permission of the copyright owner. Further reproduction prohibited without permission.

polycation, for a time optimized for adsorption of a monolayer, then rinsed and dried. The next step is the immersion of the polycationic monolayer covered substrate into a dilute dispersion of negatively charged polyanion, also for a time optimized for adsorption of a monolayer, followed by rinsing and drying. Subsequent alternating layers are self-assembled analogously. Self-assembly is now routinely employed for the fabrication of ultrathin films [46]-[48].

Langmuir-Blodgett (LB) method is another way to prepare ultrathin films. A solution of polymer is spread on a liquid subphase (normally water) to obtain a monolayer polymer film at the air/subphase interface. This monolayer, a couple of Angstroms in thickness, can be transferred to substrates, like glass, quartz, or silicon. This process can be repeated many times to obtain multilayer films with a high organization.

MBE is based on thermal evaporation of solid sources in an ultra-high vacuum environment. The evaporated material is deposited onto a heated substrate used for both mechanical support and as a template for the alignment of atoms into a crystalline structure. Typical growth rates are relatively slow. The technique is used when the required polymer thickness is less than 1 μm. MBE allows atomic-layer precision during deposition. It is commonly used to fabricate complex multi-layered structures, where each layer is typically a few nanometers thick. The technique is a basis for multiple inorganic quantum-well (MQW) laser diodes and far infrared detectors.

2.7 Characterization of the Photodetectors

The primary characteristics of photodetectors include responsivity, quantum efficiency, response time and noise-equivalent power.

Reproduced with permission of the copyright owner. Further reproduction prohibited without permission.

2.7.1 Sensitivity or responsivity

Sensitivity or responsivity is a measurement of the effectiveness of a detector in producing an electrical signal at the peak sensitivity wavelength. The responsivity is given by

$$R_e = \frac{J_{pc}}{\Phi_{in}} \tag{2-1}$$

where, R_e is responsivity in A/W, J_{pc} is photocurrent density in A/cm^2, and Φ_{in} is incident light intensity in W/cm^2.

2.7.2 The quantum efficiency

The external quantum efficiency (EQE) is the primary parameter reflecting the fundamental detection and charge transport properties of the photovoltaic and photodetectors materials and structures.

EQE η_{EQE} is defined as the ratio of electrons delivered to the external circuit per incident photon at a given wavelength. The η_{EQE} is the product of the efficiencies of four sequential steps schematically illustrated previously in Fig.2-11, 1) absorption efficiency η_A; 2) exciton diffusion efficiency η_{ED}; 3) exciton dissociation efficiency by charge transfer (CT) η_{CT}, and 4) charge collection efficiency η_{CC}.

$$\eta_{EQE} = \eta_A \eta_{ED} \eta_{CT} \eta_{CC} \tag{2-2}$$

$$\eta_{IQE} = \frac{\eta_{EQE}}{\eta_A} = \frac{\eta_{EQE}}{1 - R - T} \tag{2-3}$$

where, η_{IQE} is the internal quantum efficiency defined as the ratio of electrons delivered to the external circuit per incident photon absorbed in the device at given wavelength, R is the reflectivity, and T is transmitivity. The exicton diffusion efficiency is the probability that the photogenerated exciton diffuse to a donor-acceptor interface

Reproduced with permission of the copyright owner. Further reproduction prohibited without permission.

before it recombines. As mentioned in Chapter 2.4, the exciton diffusion length (~20nm) is typically short as compared to the film thickness (30nm~200nm). This step seems to be a restrictive factor for the EQE. For the electron D-A heterojunction, especially for the MEH-PPV and fullerene heterojunction, the CT efficiency is typically considered as ~100%. We also assume the collection efficiency at short-circuit and reverse bias is ~100%. Thus η_{EQE} is simplified as:

$$\eta_{EQE} = \eta_A \eta_{ED} \tag{2-4}$$

Therefore in the heterostructure, we can concentrate our attention on how to enhance light absorption and exciton efficiency.

2.7.3 Rise time

Rise time is a dynamic performance function of a photodetector. It is dependent on a fast and a slow component. For inorgnic semiconductor photodetectors, the fast component is the drift time of the charge carriers (electrons and holes) through the depletion region. The slow component arises from carrier diffusion. When a photodetector is operated at zero bias, the slow diffusion component dominates.

2.7.4 NEP

The sensitivity of photodetectors is usually characterized by the minimum optical signal that gives rise to a current that can be distinguished from the background current contributions from various sources of noise. Noise equivalent power (NEP) in $W/\sqrt{Hz}$ is the power of incident light, at a specific wavelength, required to produce a signal from the detector that is equal to the noise. NEP reflects the minimum detectable light power of the photodetectors. The NEP is dynamic performance, which is dependent on the bandwidth of the measuring system. It is given by

Reproduced with permission of the copyright owner. Further reproduction prohibited without permission.

$$NEP = \sqrt{\frac{2Bh\nu}{\eta} P_d} \qquad (2\text{-}5)$$

where, B is bandwidth of the system, h is Planck's constant, υ is light frequency, η is quantum efficiency.

Reproduced with permission of the copyright owner. Further reproduction prohibited without permission.

CHAPTER 3

MEH-PPV/ETHYL VIOLOGEN DIBROMIDE DEVICES

3.1 Introduction

The polymer poly(2-methoxy-5-(2′-ethylhexyloxy)-1,4-phenylenevinylene) (MEH-PPV), a soluble derivative of PPV, is widely used in polymer LEDs and photovoltaic cells due to its ease of processing and its energy gap of 2.5 eV that corresponds to the visible spectrum [51]. The MEH-PPV acts as an electron donor (p-type semiconducting polymer) with a relatively low conductivity due to a low hole and electron mobility compared to inorganic solid state semiconductor materials like Si. The relatively low conductivity of intrinsic MEH-PPV limits the quantum efficiency of pure MEH-PPV devices. A donor-acceptor heterostructure was used to enhance charge dissociation and efficiency in photodetectors and photovoltaic diodes [22]-[24][52]. Acceptors like fullerenes C60, 1-(3-methoxycarbonyl)-propyl-1-phenyl-(6,6) (PCBM) and poly(2,5,2',5'-tetrahexyloxy-7,8'-dicyanodi-p-phenylenevinylene) (CN-PPV), have greatly improved charge carrier dissociation in blended structures [53]. Due to degradation when in the presence of oxygen and moisture, most of these polymer devices were fabricated and tested in vacuum or inert ambience [53]-[57].

Methyl viologen (MV) has demonstrated ultra fast charge transfer (CT) on the order of femto seconds [58]. The radical cation of methyl viologen (MV•+) was reported

Reproduced with permission of the copyright owner. Further reproduction prohibited without permission.

to quench MV^{2+} by electron transfer from a nearby donor in 180 fs at the excitation of 296 nm pump pulse [58]. Parks et al. reported that the doping of PPV with viologen can increase photoconductivity [57], while Yang et al. reported that viologen could be used as an effective stabilizer for LEDs [59]. Thus, viologen is a good candidate for an efficient electron acceptor.

In this paper, we describe the fabrication, as well as the optical and electrical properties, of photodetectors based on thin films of blended MEH-PPV and ethyl viologen dibromide (EVD). The EVD was blended with MEH-PPV to form a donor-acceptor pair. The chemical structures of these materials are shown in Fig.3-1.

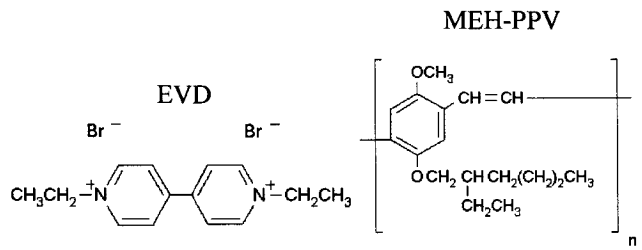

Fig.3-1 Chemical structures of MEH-PPV and EVD.

3.2 Fabrication

The devices were fabricated on 25 mm ×25 mm glass substrates which were commercially precoated with a 100 nm-thick layer of transparent, conducting indium tin oxide (ITO). We further patterned the ITO layer to a stripe of 11 mm in width. Four different solutions, made from MEH-PPV and EVD (purchased from Aldrich Co.) in weight ratio of 100%w, 98%w, 94%w, and 90%w of MEH-PPV, respectively, were spin-coated onto the patterned ITO glass substrate in air. The thin film was dried overnight in a vacuum chamber. Then the film thickness was measured with a Tencor profilometer.

Reproduced with permission of the copyright owner. Further reproduction prohibited without permission.

The thickness of the blended film was approximately 70±7nm. Then a 100 nm-thick aluminum layer was thermally evaporated onto the MEH-PPV/EVD film under 10^{-6} Torr vacuum through a shadow mask. The active area of the devices was approximately 0.09 cm^2. A corner of the blended film was swabbed to expose the ITO for electrical connection. ITO and Al electrodes were then conducted to an external circuit with silver epoxy and Al wires. The schematic diagram of such a device is shown in Fig.3-2.

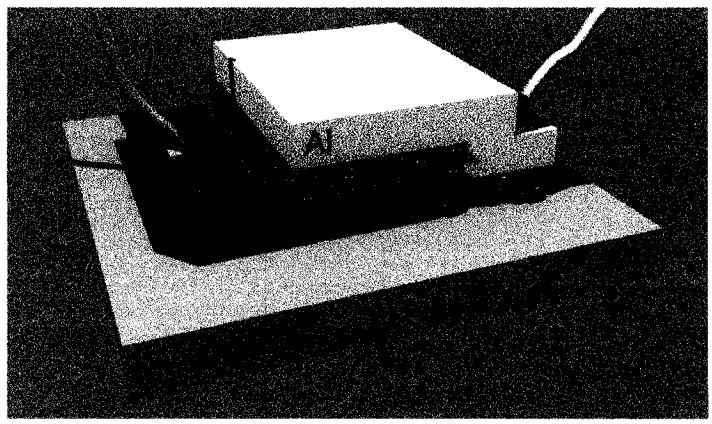

Fig.3-2. Schematic layout of the ITO/MEH-PPV:EVD/Al photodetector.

The I-V characteristics of the MEH-PPV/EVD blended devices were measured in air with a computer controlled Keithley 6487 picoammeter. The dark and light current-voltage curves were measured by sweeping the voltage between ITO and Al electrodes from positive to negative values. The incident monochromatic light was generated with a CornerStone 260 ¼ monochromator (Thermo Oriel) using a 100 W tungsten lamp. The optical power was measured with a calibrated optical power-meter (Spectra-Physics). All measurement data were collected and processed with user-customized software. The absorption spectra of MEH-PPV thin film on glass and EVD in solution were measured with a UV-visible spectrophotometer (Agilent Technologies).

Reproduced with permission of the copyright owner. Further reproduction prohibited without permission.

3.3 Results and Discussion

Fig.3-3 shows the morphology of MEH-PPV/EVD blended films and pure MEH-PPV films. We observed that the quality of the MEH-PPV/EVD blended films decreased as the concentration of EVD was increased. This is due to the fact that MEH-PPV is a non-polar polymer, soluble in toluene or chlorobezene, while EVD is polar and water-soluble. Thus EVD can cause moisture-retention and aggregation on the polymer film.

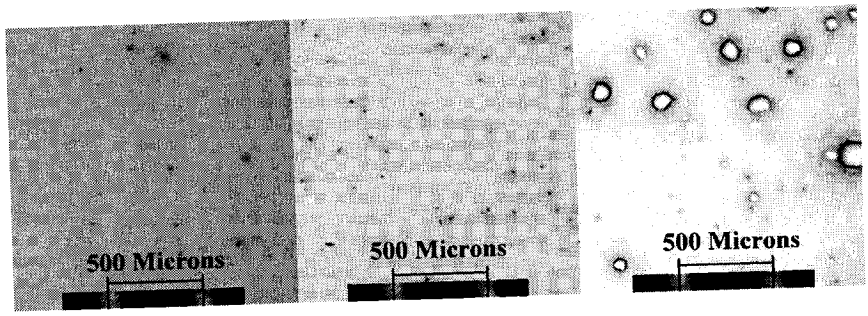

Fig.3-3 Optical microscope images of pure MEH-PPV film (left), MEH-PPV/EVD film with 10%w of EVD (middle), and MEH-PPV/EVD film with 18%w of EVD (right).

The quality of the blended films was found to significantly affect the breakdown voltage of the device. For pure MEH-PPV based devices, the breakdown voltage is ~ 21 V, while for EVD doped 98%w MEH-PPV and 94%w MEH-PPV devices, breakdown voltages are ~ 18 V and ~11 V, respectively (see the inset of Fig.3-4).

Fig.3-4 compares the current-voltage characteristics of devices with 100%w and 94%w MEH-PPV in dark conditions and under 540nm wavelength monochromatic illumination with the optical power density of 169$\mu W/cm^2$. Significant increases in photocurrent were observed when EVD was added to the active polymer layer. The increase of the dark current with EVD doping could be due to leakage.

Reproduced with permission of the copyright owner. Further reproduction prohibited without permission.

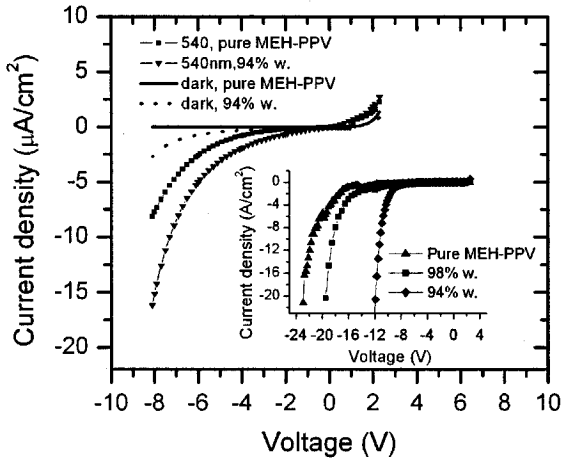

Fig.3-4 Current–voltage curves of MEH-PPV/EVD devices with 94%w and 100%w of MEH-PPV in the dark (dotted line and solid line, respectively) and under the illumination of 540 nm wavelength monochromatic light with the optical power density of 169 μW/cm^2 (triangles and squares, respectively). Inset: The devices breakdown characteristics of 100%w (triangles), 98%w (squares), and 94%w of MEH-PPV (diamonds).

Fig.3-5 shows the optical absorption of pure MEH-PPV film, MEH-PPV/EVD film (90%w) on glass, and EVD in water. The absorption edge of the MEH-PPV spectrum shown in Fig.3-5 and the EQE spectrum edge of MEH-PPV and MEH-PPV/EVD blended devices shown in Fig.3-6 are in a good agreement. The absorption of EVD peaks at ~ 267 nm and the absorption edge is ~ 300 nm as shown in Fig.3-5.

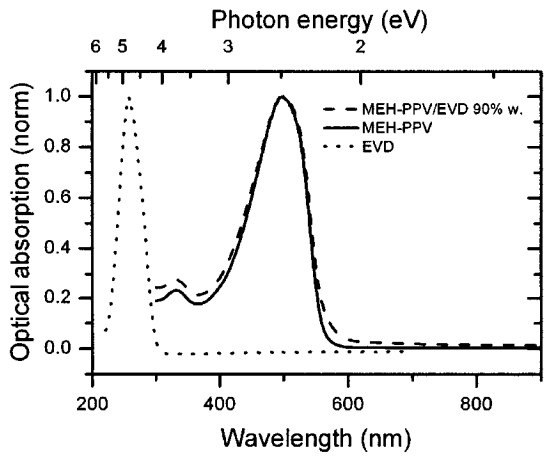

Fig.3-5 Optical absorption of EVD in water (dotted line), MEH-PPV film (solid line) and MEH-PPV/EVD 90%w film (dashed line) on glass.

Reproduced with permission of the copyright owner. Further reproduction prohibited without permission.

Fig.3-6 shows the external quantum efficiency (EQE) of devices (100% w, 98%w, 94%w, and 90%w of MEH-PPV). The maximum EQE of the MEH-PPV/EVD (94 %w of MEH-PPV) device at 4V reverse bias is ~3 %; twice the maximum EQE of the 100%w MEH-PPV device (see Fig.3-6). Compared to Park et al's work [57], our smaller EQE values could be due to the testing in air, rather than in a vacuum, or the lower doping weight percentages of EVD, in our case only 6%w of EVD (94%w of MEH-PPV) compared to 30%w of EVD (70% w of PPV) in Park et al's work [57]).

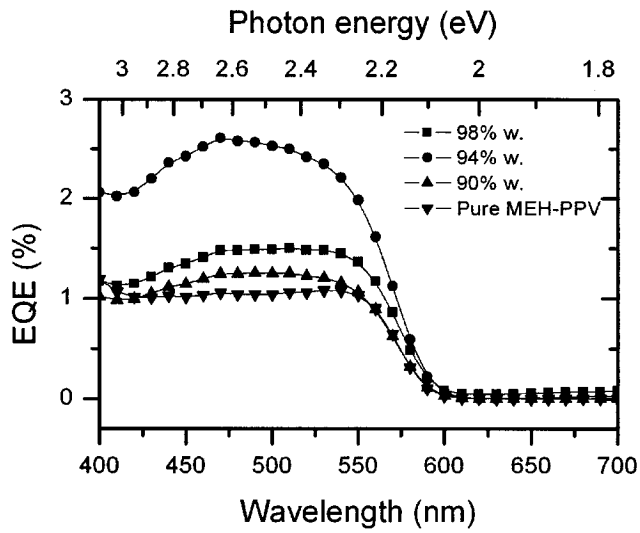

Fig.3-6 EQE versus wavelength for MEH-PPV/EVD devices: 100% w (downward triangles), 98% w (squares), 94% w (circles), and 90% w of MEH-PPV (upward triangles) at the reverse bias of 4 V.

We observed the hysteresis of the I-V characteristics of the MEH-PPV/EVD devices by sweeping the voltage between anode and cathode between -2 V and 2 V as indicated with arrows at a sweep speed of 1V/s in Fig.3-7a) and Fig.3-7b). To our knowledge this is the first report on the hysteresis in MEH-PPV-based diodes. However, the hysteresis effect has been observed for some other semiconductive polymers such as poly[3-(6-methoxyhexyl)thiophene][60] and poly(2,5-pyridinediyl) [61] and is explained

Reproduced with permission of the copyright owner. Further reproduction prohibited without permission.

by the accumulation of stored charge at the interfaces between the polymer and conductive electrode. Several reports [62]- [64] have demonstrated that in the MEH-PPV-based devices exposed to the air, MEH-PPV has trapping states due to the presence of oxygen. Therefore the hysteresis in the MEH-PPV and MEH-PPV/EVD devices that we fabricated and tested in air could be due to the charges stored in these traps.

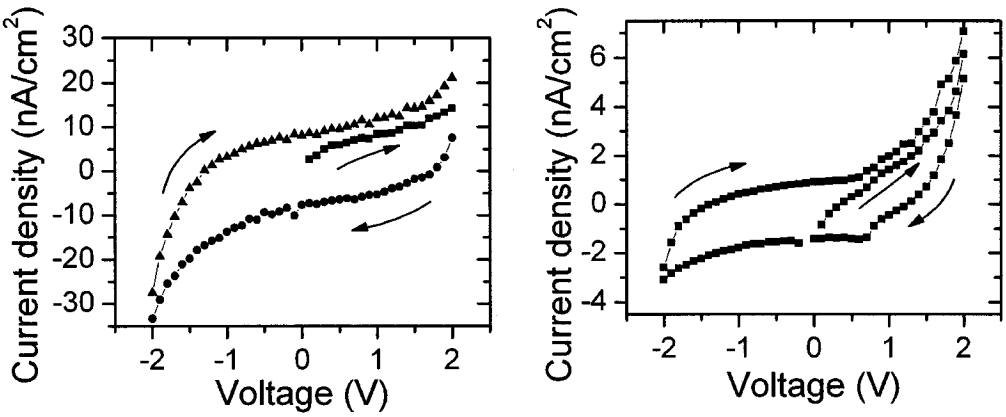

Fig.3-7 The hysteresis effect in MEH-PPV/EVD-based devices in the dark for the voltage sweep between -2V and 2V: 94% w of MEH-PPV (left); 100% w MEH-PPV (right).

3.4 Summary

In this chapter we investigated the photodetecting and electronic properties of MEH-PPV and MEH-PPV/EVD blended thin film diodes. The presence of the EVD in the MEH-PPV active layer of devices caused the external quantum efficiency of the device to double due to improved electron charge transfer. The optimum EVD content in the MEH-PPV/EVD blend was found to be around 6%w to minimize the aggregation of EVD and water-retention. Also, an interesting hysteresis phenomenon was observed in MEH-PPV and MEH-PPV/EVD devices exposed to air.

Reproduced with permission of the copyright owner. Further reproduction prohibited without permission.

CHAPTER 4

MEH-PPV/PBSE QUANTUM DOTS DEVICES

4.1 Introduction

Conjugated polymers, nanocrystal quantum dots (QDs) and their composites have attracted the attention of researchers for the development of novel optoelectronic devices, such as light emitting diodes (LEDs) [65][66], photovoltaics [67][68], and optical information memory [69]. The tunable band gap of QDs makes them attractive for tailoring the visible and infrared absorption and emission of the light-sensitive layer of optoelectronic devices. Both conjugated polymers and nanocrystals are promising candidates for novel optoelectronic devices because of their easy device fabrication processing methods such as spin-coating or doctor-blading.

The PbS, CdTe, and CdSe QDs have been investigated in LEDs and solar cells [65]-[68], [70]. Efficient excitation transfer from a conducting polymer to PbS QDs has been reported from photoluminescence measurements [71]. In comparison to CdSe or CdS QDs, the PbSe QDs show stronger quantum confinement due to their large exciton Bohr radius of ~ 40 nm and low effective hole and electron masses [72]. The bandgap of PbSe QDs is tunable from ~ 0.5 eV to ~ 1.6 eV for QD diameters ranging from 9 nm to 3 nm. Recently, Schaller et al. have demonstrated the carrier multiplication in PbSe QDs by monitoring their transient absorption [73]. These transient absorption results ha

Reproduced with permission of the copyright owner. Further reproduction prohibited without permission.

shown that the photogeneration of multiple excitons can occur via impact ionization (the inverse of Auger recombination) [74] for pumping photon energies $\geq 3 \cdot E_g$, where E_g is the bandgap of PbSe QDs. For PbSe QDs with the absorption peak of ~1900 nm and diameter ~ 8 nm, this corresponds to excitation wavelengths smaller than ~ 630 nm, still in the visible range. However, for QD sizes < 4.5 nm, corresponding to the absorption peak < 1100 nm, the carrier multiplication should not occur for excitations in the visible range. This phenomenon of carrier multiplication can be exploited to realize efficient optoelectronic devices.

In this chapter, we describe the fabrication and properties of efficient photodetectors based on the conducting polymer poly [2-methoxy-5-(2'-ethylhexyloxy)-1,4-phenylenevinylene] (MEH-PPV) and PbSe nanocrystal QDs. The optoelectronic devices made of pure MEH-PPV have limited quantum efficiency due to a low electron and hole mobility compared to those of inorganic materials [75]. When PbSe QDs are dispersed in the polymer host, with the absorption spectrum in the visible range, we observed a dramatic enhancement of the quantum efficiency of the polymer-based photodetectors.

4.2 Fabrication and Design of MEH-PPV/PbSe Photodetectors

The MEH-PPV/PbSe photodetectors were fabricated on 25mm×25mm glass substrates pre-coated with a 150-nm-thick layer of indium tin oxide (ITO) with a sheet resistance R_s=5-15Ω/□. Sheet resistance is defined as $R_s = \rho \frac{L}{A}$, where ρ is the resistivity of the sample, and L and A are its length and cross-sectional area. A 60-nm-thick layer of PEDOT/PSS (poly(2,3-dihydrothieno(3,4-b)-1,4-dioxin/poly(styrenesulfonate)) was spin-

Reproduced with permission of the copyright owner. Further reproduction prohibited without permission.

cast on the ITO substrate in order to improve the charge transport through the device. The active layer of the photodetector was also spin-cast from the MEH-PPV/PbSe mixed solution. The MEH-PPV, a soluble derivative of poly(p-phenylene vinylene) was used as a host for the PbSe QDs. PbSe QDs were capped with 2 nm-long oleic acid ligands. The MEH-PPV was dissolved in chlorobenzene and filtered with a 5 μm syringe filter. The MEH-PPV and PbSe QDs were mixed to make films with 99.7% of total weight (w), 99%w, 97%w, 95%w, 90%w, 83%w, and 50%w of MEH-PPV. Another device with pure MEH-PPV was fabricated for comparison. The average thickness of polymer-nanocrystal blended films was about 60 nm, as measured by a stylus profilometer (Tencor Alpha Setup 500). The samples were stored in vacuum overnight to completely remove the residue solvent. Finally, an aluminum top electrode was fabricated using thermal evaporation through a shadow mask. The active area of the photodetector was about 0.07 cm^2 (~ 3 mm x 2.3 mm). The schematic diagram of the fabricated devices was shown in Fig.4-1.

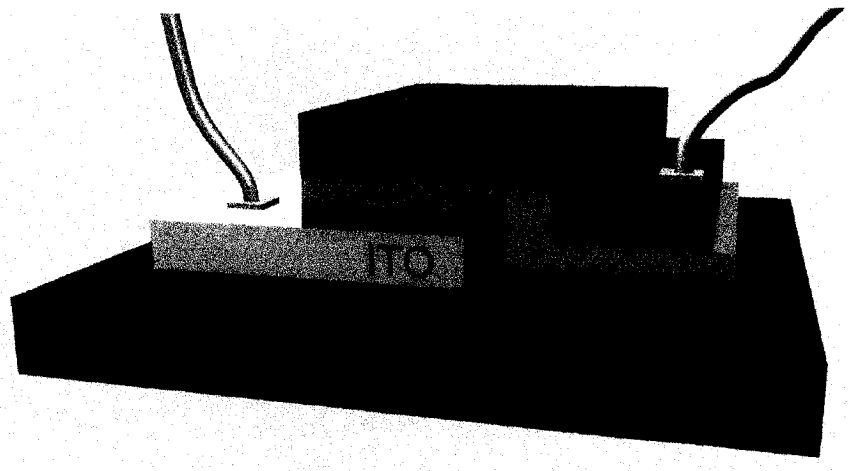

Fig.4-1 The schematic layout of the ITO/PEDOT:PSS/MEH-PPV:PbSe/Al photodetector on a glass substrate.

Reproduced with permission of the copyright owner. Further reproduction prohibited without permission.

4.3 Result and Discussion

Fig.4-2 shows the transmission electron microscope (TEM) images of PbSe QDs dispersed in MEH-PPV. The molecular weight of MEH-PPV (Mw=86,000) indicates that the average degree of polymerization of MEH-PPV is ~ 334, i.e., 334 units in one molecule backbone. One repeating unit of MEH-PPV is ~8 Å [76]. The average molecular length of MEH-PPV is ~267 nm. The size of PbSe QDs is 8 nm and the absorption peak is at 1900 nm. The PbSe QDs were capped with a 2-nm-long oleic acid ligand to prevent aggregation and to provide a good dispersion of PbSe QDs in the MEH-PPV host.

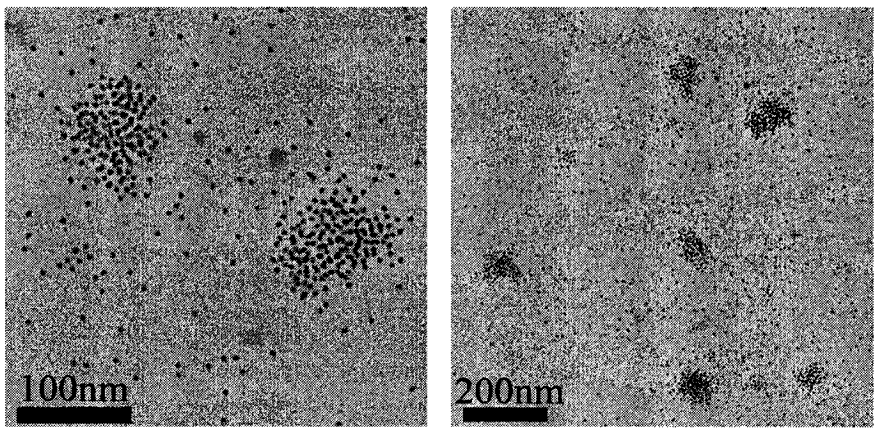

Fig.4-2 TEM images of PbSe QDs (1900 nm) in the MEH-PPV host (95%w of MEH-PPV). The scale bars in the left and right images are 100 nm and 200 nm, respectively. Some aggregation of QDs into non-ordered clusters is observed.

The current-voltage characteristics were measured in air with a picoammeter (Keithley 6487) remotely controlled via a GPIB interface (National Instrument). The samples were measured immediately after the external leads were attached to the electrodes using a silver paste. The sample degradation in air occurs on timescales longer than the timescales of our measurements. The monochromatic light was generated with a monochromator (Thermo Oriel) origininating from a 100 W tungsten lamp source. The

Reproduced with permission of the copyright owner. Further reproduction prohibited without permission.

optical power was read with a multifunction optical power-meter (Spectra-Physics). The photocurrent densities of MEH-PPV/PbSe (1900 nm, 99.7%w, 99%w, 97%w, 95%w, 90%w, 83%w, and 50%w of MEH-PPV) photodetectors and a pure MEH-PPV device in the dark and under the illumination with 510 nm, 68 $\mu W/cm^2$ monochromatic light are given in Fig.4-3 . For all the measured devices, the dark current was $< 10^{-7}$ A at reverse bias voltages 0>V>-8 V, i.e., 1 to 2 orders of magnitude lower than the photocurrent.

From Fig.4-3 we see that there is a range of polymer weight in the mixture, around 95±2%w, for which the photocurrent is optimal. This corresponds to ~ 95%w of the polymer and ~ 5%w of the QDs. In contrast, the devices with ~50%w polymer and 100%w polymer show smaller photocurrents. When the amount of QDs is large (>50%w), the photoconduction through the film decreases. We have measured the photocurrent in pure PbSe QDs arrays separately, and it is several orders of magnitude lower than in the polymer-nanocrystal films. The presence of significant amounts of the conducting polymer appears to help the charge transport, while the photogeneration occurs in both the polymer and the QDs. We speculate that the concentration of QDs should be low enough to allow for many QDs to be well separated. Fig.4-3 (inset) shows photocurrent for four devices from 97% w to 100% w of polymer. The photocurrent is largest for 97% and decreases as the polymer content is increased to 100%.

Reproduced with permission of the copyright owner. Further reproduction prohibited without permission.

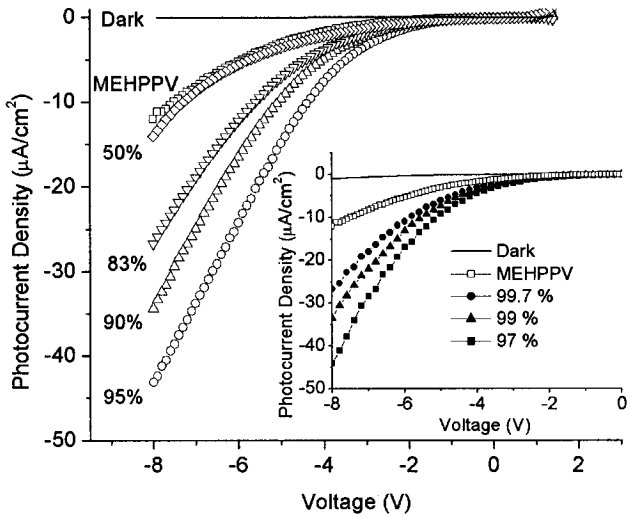

Fig.4-3 Photocurrent density of MEH-PPV/PbSe (1900 nm) photodectors with 95%w (circles), 90%w (upward triangles), 83%w (downward triangles), 50%w of MEH-PPV (diamonds), and pure MEH-PPV (squares) under the illumination with 510 nm monochromator light with power density of 68 $\mu W/cm^2$. The dark current (solid line) for all devices is similar and $<10^{-7}$A. Inset: Photocurrent density for devices with 97%w (solid squares), 99%w (solid triangles), 99.7%w (solid circles), 100%w of MEH-PPV (open squares), and dark current (solid line).

In Fig.4-4 we show the EQEs of MEH-PPV/PbSe (1900 nm) and MEH-PPV/PbSe (1100 nm) composite photodetectors with the same polymer weight percentage (95%w), but two different QD diameters. The maximum EQE of the MEH-PPV/PbSe (1900nm, 95%w of MEH-PPV) composite at –8V is ~150%, more than three times higher than the maximum EQE of a pure MEH-PPV device, as shown in Fig.4-4. The maximum EQE of the MEH-PPV/PbSe (1900nm, 95%w of MEH-PPV) composite at –4V is 30%. The gain (i.e., EQE greater than 100%) at -8 V applied to the ITO electrode was observed in the devices with MEH-PPV/PbSe 99%w, 97%w, 95%w and 90%w of MEH-PPV, and not in devices with 99.7%w, 83%w, and 50%w of MEH-PPV. It is assumed that in the MEH-PPV one photon generates only one exciton. If the photon energy is larger than the optical bandgap of the polymer, the excess energy will not contribute to generation of

Reproduced with permission of the copyright owner. Further reproduction prohibited without permission.

additional charge carriers. The EQE greater than 1 indicates that the gain could be due to the carrier multiplication via multiple excitons in PbSe QDs. This is in agreement with recent results in Ref. [73]. In MEH-PPV/PbSe (1900 nm, 95%w of MEH-PPV) composite photodetectors the EQE reaches a maximum value of ~ 150% at 510 nm, close to the reported threshold [73] for formation of triple excitons.

Fig.4-4 inset shows the optical absorption of the pure MEH-PPV film, the MEH-PPV/PbSe QD blended films, and of the solution of the pure PbSe QDs measured with a UV-Visible Spectrophotometer (Agilent Technologies). The absorption peak of MEH-PPV is ~ 498 nm. The absorption peaks of all MEH-PPV/PbSe (1900 nm) composites are red-shifted to ~ 505 nm (shift of ~35 meV on energy scale), due to the presence of PbSe QDs.

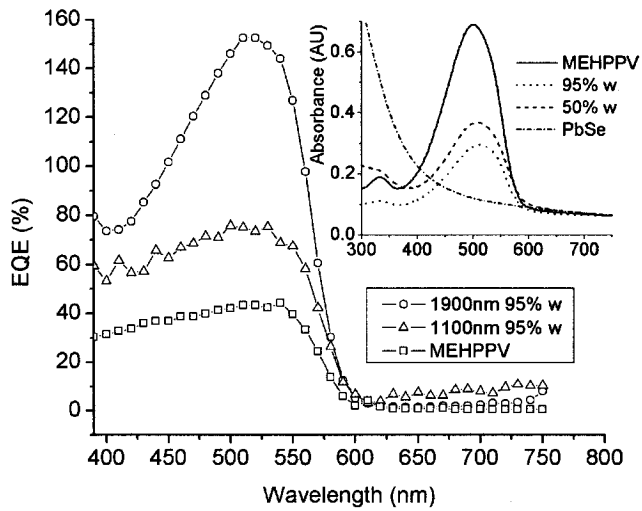

Fig.4-4 Comparison of external quantum efficiencies of the MEH-PPV/PbSe QD photodetectors at -8V: pure MEH-PPV (squares), MEH-PPV/PbSe (1100 nm) (circles), and MEH-PPV/PbSe (1900 nm) (triangles). Inset: UV/visible absorption spectrum of MEH-PPV:PbSe blended films on glass slides with 95%w (dots), 50%w (dashed line), pure MEH-PPV film (solid line), and PbSe QDs in solution (dash-dot line).

Reproduced with permission of the copyright owner. Further reproduction prohibited without permission.

In order to confirm that the observed photocurrent gain results from the appropriate choice of nanocrystal diameters, we have fabricated MEH-PPV/PbSe photodetectors with smaller PbSe QDs. For these devices, we used QDs with diameters ~ 4.5 nm, corresponding to the main absorption peak at ~1100 nm. Because the estimated onset energy for carrier multiplication in these QDs is ~ 2.38 eV or ~ 367 nm, the photocurrent gain should not exist for the light excitations in the wavelength range from ~370 nm to ~800 nm. In Fig.4-4 we show the experimental results confirming that the efficiency is less than 100 % for the MEH-PPV/PbSe (1100 nm, 95%w of MEH-PPV) composite photodetectors. We observed similar results for devices with 90%w, and 83%w of the polymer. The EQE of all the devices (1100 nm) with the polymer weight percentage of 95%w, 90%w and 83 %w is significantly less then 100%w, and so no gain is observed.

4.4 Degradation

All photodetectors were tested in the air. Device degradation cannot be avoided in the presence of oxygen and moisture. We performed the life time measurements and calculations of EQE (λ) of the MEH-PPV/PbSe QD photodetector (95%w of MEH-PPV) and pure MEH-PPV photodetector at reverse bias of 8V. The EQE peak (λ=510nm) decays with time were plotted in the Fig.4-5 and Fig.4-6. The degradation or aging of electronic devices usually obey the Weibull distribution in statistics, which is one of the most widely used lifetime distributions in reliability engineering. Standard Weibull probability density distribution (*pdf*) is described as

$$f(x) = \left[\frac{b}{\theta}(\frac{x}{\theta})^{b-1}\right]\{\exp[-(\frac{x}{\theta})^{b}\} \qquad (4\text{-}1)$$

Reproduced with permission of the copyright owner. Further reproduction prohibited without permission.

where x is variable (usually life), b is Weibull slope or "shape" parameter, θ is the characteristic life or "scale" parameter, and b=1 for random failure with mixture of several failure modes. Thus Eq.(4-1) is rewritten as:

$$f(x) = \frac{1}{\theta}\exp(-\frac{x}{\theta}) \qquad (4\text{-}2)$$

We used Eq. (4-2) to fit our degradation data of the photodetectors. Thus the lifetime of the photodetector is defined as the expectation value θ of Eq.(4-2). From the fitting results, the lifetime of the MEH-PPV/PbSe QD photodetectors (95%w of MEH-PPV) and the pure MEH-PPV photodetectors were estimated to be 455 hours and 555 hours, respectively. In the previous work [77], Zyung's group had reported that UV/Vis absorption peak decreased much more in the air than in the vacuum, and the absorption peak has shown a blueshift. Both of them suggested a scission of the polymer chain, in another words, a reduced conjugated length. This reduction in the conjugated length was also proven by the decrease of molecular weight of poly (3-alkylthiophenes) (P3AT) reported in Ref.[78] when exposed to the presence of oxygen and by the observed strengthening of the carbonyl peak of MEH-PPV film with aging in the air [79]. The energy required to break C=C double bond is about 1.51 eV, or 145 kJ/mol [80]. Therefore, the photon in visible range has enough activation energy to break the double bond in the polymer chain. In addition, the presence of oxygen and H_2O and increased temperature will greatly accelerate the degradation process of polymer film [81].

From the Fig.4-5 and Fig.4-6 we can see that the lifetime of the devices decay fast within the first three days and then the decay process slows down. After one month, the EQE peaks of the two devices are close to each other. We believe that oxygen not only scissors the MEH-PPV chain, but also scissors the organic ligand, a charge transfer path

Reproduced with permission of the copyright owner. Further reproduction prohibited without permission.

between MEH-PPV and PbSe QD. Thus, the function of PbSe QD degrades quickly and finally only QD host - MEH-PPV dominantly affects the performance of the devices.

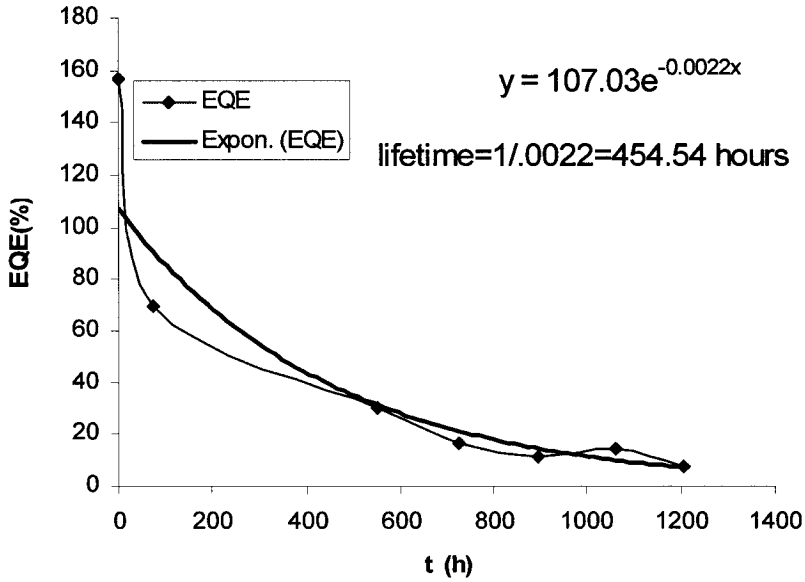

Fig.4-5 The peak EQE (reverse bias of 8V and wavelength 510nm) of the MEH-PPV/PbSe QD photodetector (95%w of MEH-PPV) decays exponentially with time.

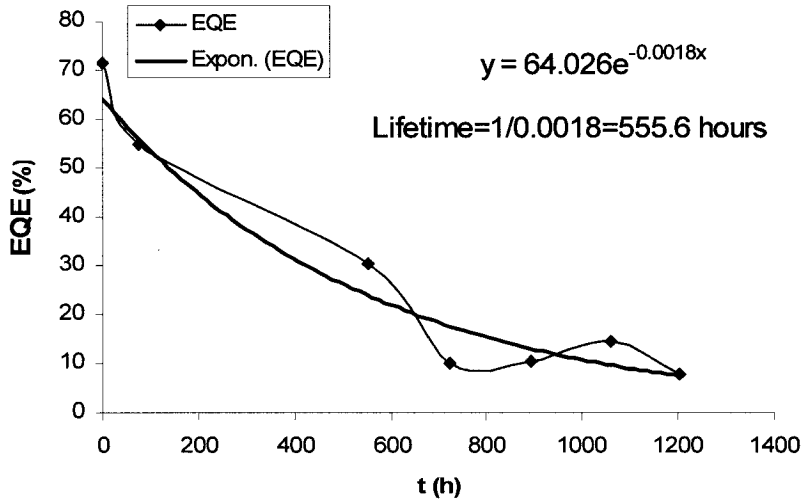

Fig.4-6 The peak EQE (at reverse bias of 8 V and wavelength of 510 nm) of the pure MEH-PPV photodetector (100%w of MEH-PPV) decays exponentially with time.

Reproduced with permission of the copyright owner. Further reproduction prohibited without permission.

4.5 Summary

In conclusion, we show the photocurrent measurements for several devices consisting of different polymer-nanocrystal mixing ratios with polymer concentrations ranging from 50% to 100% of the total mass. We used two different sizes of PbSe QDs, one with the IR absorption peak at 1100 nm (1.13 eV) and the QD diameter ~ 4.5 nm, and the second, with the absorption peak at 1900 nm (0.65 eV) and QD diameter ~ 8 nm. For excitation wavelengths from ~ 400 to 800 nm, quantum efficiencies greater than 1 (i.e. gain) are observed only in devices with the larger PbSe QDs, which is as expected. By choosing a suitable size of QDs, we can tailor the photoresponsivity spectrum of the composite devices in the visible range. The degradation measurement of the devices showed that lifetime of MEH-PPV/PbSe QD photodetectors is expected to around 19-23 days.

Reproduced with permission of the copyright owner. Further reproduction prohibited without permission.

CHAPTER 5

MEH-PPV/PCBM DEVICES

5.1 Introduction

The poly(2-methoxy-5-(2,9-ethyl-hexyloxy)-1,4-phenylenevinylene) (MEH-PPV), a soluble derivative of PPV, is widely used in polymer LEDs and photovoltaic cells due to the ease of processing and significantly higher hole mobility than electron mobility. The photodetector made of pure MEH-PPV has a relatively low quantum efficiency due to a limited exciton diffusion length of 20±3 nm [40][82] and relatively low hole mobility compared to inorganic semiconductor materials like Si. A donor-acceptor heterostructure has been used to enhance charge dissociation or charge transfer in photodetectors and photovoltaics (solar cells) [52]. Therefore, electron donors should have a low ionization potential and acceptors should have a high electron affinity. Acceptors like C60 and its derivatives{6}-1-(3-(methoxycarbonyl)propyl)-{5}-1-phenyl-[5,6]-C61(PCBM), and poly(2,5,2',5'-tetrahexyloxy-7,8'-dicyano-di-p-phenylenevinylene) (CN-PPV), have been demonstrated to greatly improve the charge carrier dissociation [52][83]. When donor and acceptor molecules form a heterjunction or dispersed heterjunction, photoinduced excitons are dissociated at the junction interface. It is energetically favorable for the dissociated electrons flowing from the donor to the acceptor and then transversing the acceptor and being collected by the cathode (like A1). Conversely, the dissociated holes

Reproduced with permission of the copyright owner. Further reproduction prohibited without permission.

are transferred in donor by hopping and finally arrive to anode. Usually, the efficiency of exciton dissociation from conjugated polymers to fullerenes or its derivatives is considered to be unity [83]. Therefore, how to establish an efficient charge transporting path to enhance quantum efficiency is well worth investigating.

In this chapter we present the experimental results for a polymer-fullerene compound photodetector in single blended layer (SBL) and double blended layer (DBL) configuration. This diode is based on MEH-PPV and PCBM. The chemical structures of MEH-PPV and PCBM are shown in Fig.5-1. In SBL photodetectors, the photoactive layer was spin-cast from a MEH-PPV-rich solution. The active layer in DBL consists of one MEH-PPV-rich composite film and an extra PCBM-rich layer. An aluminum cathode was deposited by thermal evaporation. These devices were illuminated under monochromatic light in the visible range originating from a tungsten lamp source. The increase in photoconductivity of MEH-PPV/PCBM photodetectors in DBL may be due to a more efficient charge carrier transport path than the one in SBL. The results from this work clearly demonstrate the application of the reported approach to the realization of polymer photodetectors or solar cells with increased photoconductivity characteristics.

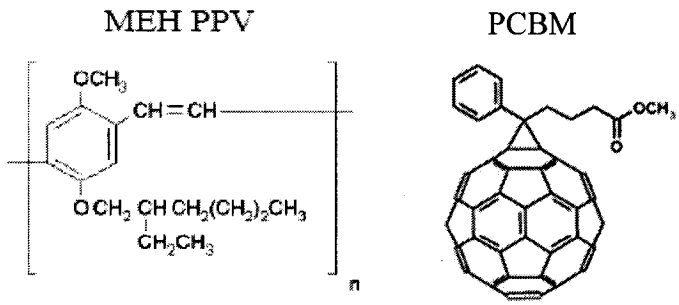

Fig.5-1 The molecule structure of MEH-PPV and PCBM.

Reproduced with permission of the copyright owner. Further reproduction prohibited without permission.

5.2 Fabrication

The cells were fabricated on 25mm×25mm glass substrates commercially precoated with a 100 nm-thick transparent conducting indium tin oxide (ITO). We further patterned the ITO layer to a stripe of 11 mm in width. Then a 60nm-thick PEDOT: PSS (Sigma Aldrich) was spincast on the ITO layer, with the purpose of reducing dark leak current and increasing device yield. Two kinds of solutions were prepared from MEH-PPV (Sigma Aldrich Co.) and PCBM (American Dye Resources, Inc.). One was MEH-PPV-rich solution with MEH-PPV and PCBM in weight ratio of 3:1 in xylene. The other PCBM-rich solution was made from MEH-PPV and PCBM in weight ratio of 1:3 in the same solvent. In SBL photodetectors, the light-sensitive layer was only spin-cast from MEH-PPV-rich solution. For DBL photodetectors, an extra PCBM-rich composite film was spin-cast on the MEH-PPV-rich composite layer. All samples were dried in a vacuum chamber overnight. A 100 nm-thick aluminum layer was thermally evaporated on the polymer composite blended film under 10^{-6} Torr vacuum through a shadow mask. The active area of the photodetectors was approximately $4\times4mm^2$. The schematic diagram of such a device is shown in Fig.5-2.

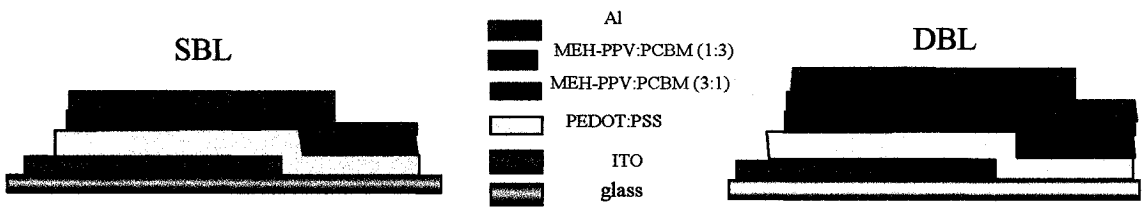

Fig.5-2 The schematic layout of ITO/PEDOT: PSS / MEH-PPV: PCBM/Al.

Reproduced with permission of the copyright owner. Further reproduction prohibited without permission.

5.3 Result and Discussion

Fig.5-3 shows the UV/Vis absorption spectrum of conjugated polymer MEH-PPV and PCBM. MEH-PPV has an absorption peak in the visible range at 497nm. The cut-off wavelength of absorption of MEH-PPV is approximately 600nm, which suggests the optical bandgap of 2.1eV. PCBM also has a certain absorption in the visible range and partially contributes to exciton generation. At this point, PCBM differs from other acceptors like EVD as mentioned previously in Chapter 3. Fig.5-4 shows the energy band diagram of the MEH-PPV/PCBM composite photodetectors. The LUMO difference of MEH-PPV and PCBM provide sufficient internal force to drive photo-generated exciton dissociation and charge transfer.

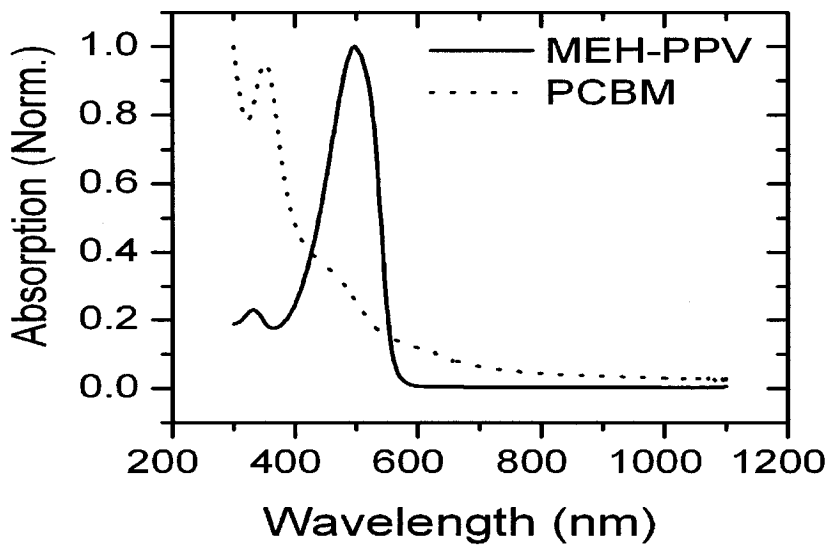

Fig.5-3 The normalized absorption spectrum of MEH-PPV solution in toluene and PCBM film (from Ref.[84]).

Reproduced with permission of the copyright owner. Further reproduction prohibited without permission.

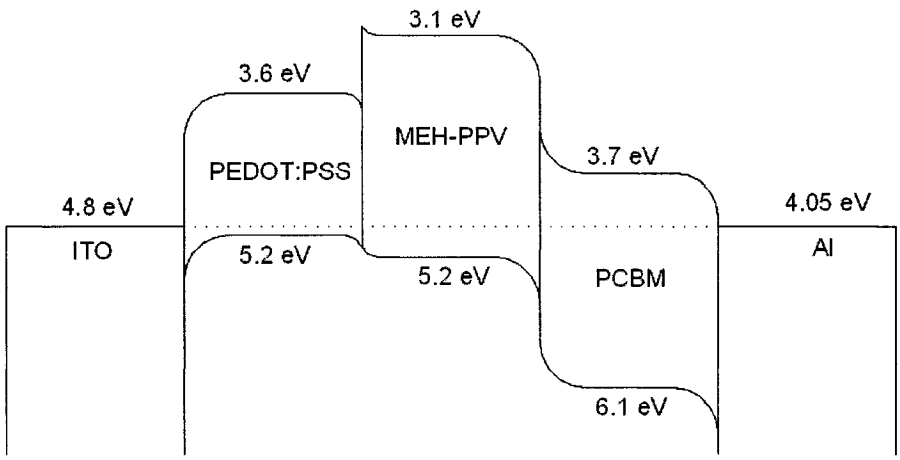

Fig.5-4 The energy band diagram of MEH-PPV/PCBM photodetectors.

Fig.5-5 shows the current of MEH-PPV/PCBM photodetectors indark and 550 nm light with intensity of 90uW/cm^2. Fig.5-6 shows external quantum efficiency (EQE) of MEH-PPV/PCBM photodetectors as a function of wavelength. From Fig.5-5, we can see the photoconductivity of the DBL photodetectors increases significantly, at a voltage >0.4V, compared to that of SBL photodetectors. There are two components in photocurrent: diffusion current and drift current. Diffusion current, arising from the charge carrier gradient, is a dominant component at low electric field. Drift current is due to charge carrier transit in the electrical medium and increases with applied bias. Drift current becomes the dominant current at high electric field. Therefore, the magnitude of current at high electric field reflects the efficiency of charge-transport. Even though the concentration of PCBM in SBL was higher than the percolation threshold of 17% for the formation of a continuous electron-transport path [82], the high EQE in DBL shown in Fig.5-6 demonstrated that the charge-transfer in DBL is more efficient than the one in SBL. The MEH-PPV-rich composite film in SBL has a good transport path for holes, but not for electrons. However, this problem is solved by introducing an additional PCBM-layer. Compared to SBL, the MEH-PPV-rich layer in DBL can ensure primary optical

Reproduced with permission of the copyright owner. Further reproduction prohibited without permission.

absorption and hole transfer, and the PCBM-rich layer in DBL can improve electron acceptance and transfer. At the interface of the two layers, the MEH-PPV and the PCBM interpenetrate due to the slow evaporation rate of the xylene. Such interpenetrating of the MEH-PPV and the PCBM can enhance the efficiency of hole-and electron-transfer.

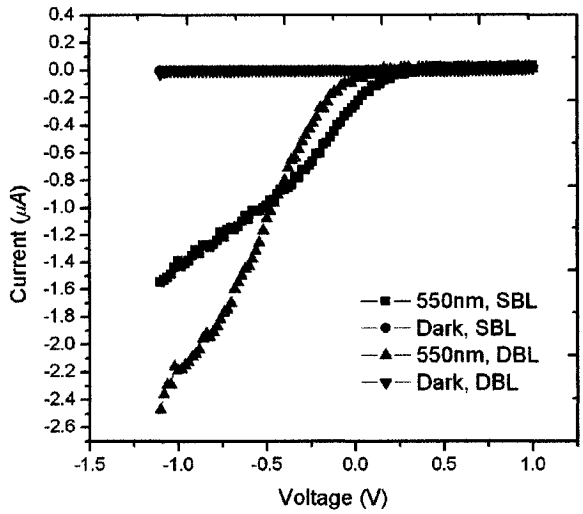

Fig.5-5 The dark and light current of MEH-PPV/PCBM photodetector in SBL and DBL configuration, at 550nm light with intensity of 90uW/cm^2.

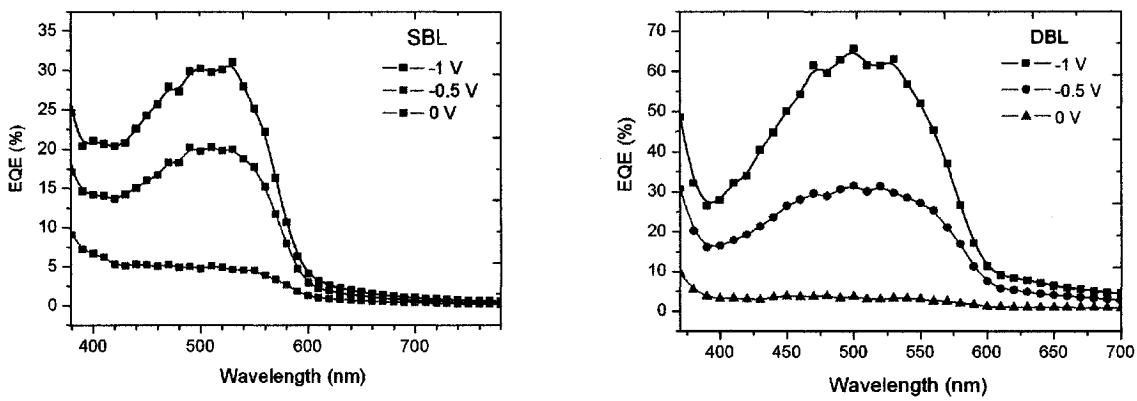

Fig.5-6 The external quantum efficiency of ITO/PEDOT: PSS/MEH-PPV: PCBM /Al in SBL (left) and in DBL (right) at the reverse bias of 0V, 0.5V and 1V, respectively.

From Fig.5-6 we can see that the EQE of the DBL photodetector is higher than that of the SBL photodetector at the reverse bias of 0.5V, and nearly double that of SBL

Reproduced with permission of the copyright owner. Further reproduction prohibited without permission.

photodetectors at the reverse bias of 1 V. At low bias the EQEs of photodetectors in SBL and DBL did not show any obvious difference.

5.4 Summary

From the experimental results presented above, we can conclude that the electron donor MEH-PPV and the electron acceptor PCBM are highly promising polymer-organic pairs for photodetectors or solar cells. The DBL configuration, with the good interpenetration of the MEH-PPV and the PCBM, significantly improves the electron transfer and the quantum efficiency of the polymer photodetector.

Reproduced with permission of the copyright owner. Further reproduction prohibited without permission.

CHAPTER 6

ELLIPSOMETRY FOR OPTICAL PROPERTY DETERMINATION

6.1 Introduction

Promising electrical and optical properties of MEH-PPV and Poly(3-hexylthiophene) (P3HT) have led to research for applications in flexible electronics and optoelectronics, e.g. LEDs [65][66] , solar cells [67][68][85][86], photodetectors [22], FETs [87], optical waveguides [88] and lasers [89].

P3HT is classified as regio-regular P3HT (rr-P3HT) and regio-random P3HT (rra-P3HT) according to the percentage of stereoregular head-to-tail attachment of hexyl side chains to the 3-position of the thiophene ring. The chemical structures of rr-P3HT and rra-P3HT are shown in Fig.6-1. Compared to rra-P3HT, the rr-P3HT in a lamellar structure has high field hole mobility up to 0.1 $cm^2/V\text{-}s$ [90]. However, the zero-field hole mobility of MEH-PPV film is 10^{-4} to 10^{-7} $cm^2/V\text{-}s$ [91][92]. Therefore, P3HT compared to MEH-PPV is more promising for photovoltaic application due to its higher hole mobility and broader solar-energy absorption.

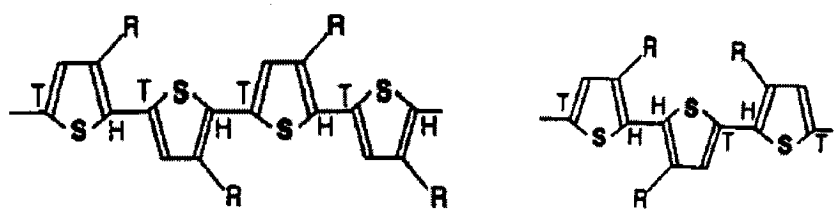

Fig.6-1 The chemical structure of rr P3HT (left) and rraP3HT (right). H denotes Head and T denotes Tail. (From Ref.[93]).

Reproduced with permission of the copyright owner. Further reproduction prohibited without permission.

Impressive results have been achieved with P3HT-based and MEH-PPV-based solar cells [67][68][85][86]. In order to design and optimize the solar cells or other optoelectronic devices, the spectral dependence of their optical and electrical properties is required. The optical properties are especially important for the design of light-trapping structures with diffraction gratings in solar cells or photodetectors. This important information for spin-cast MEH-PPV film[94], polyacetylene film[95][96], MEH-PPV/polyethylene (PE) blended film[97][98], poly (2,5-pyridinediyl) film[99] , poly(octylthiophene) film[100], fluorinated polymer film[101], PPV film [102], and poly(arylenephenylene) film[103], have been published. In this chapter, we present the spectral dependence and anisotropy of complex refractive indices, absorption coefficients, and complex dielectric constants of spin-cast rr-P3HT and MEH-PPV thin films with variable angle spectroscopic ellipsometry, which will be used for the numerical simulations of photodetectors in Chapter 8 and 9.

In this chapter we present the optical properties of MEH-PPV and P3HT obtained with optical ellipsometry. Further, we investigated the anisotropy of optical and dielectric properties of P3HT thin film, which reflect the inherent anisotropy of the electronic states.

The anisotropy of optical constants of conjugated polymer films, e.g. MEH-PPV[94][97][98], polyacetylene[95][96], poly(octylthiophene)[100], fluorinated polymer, PPV[101], poly(2,5-pyridinediyl)[99], and poly(arylenephenylene)[103], have demonstrated that the molecular chains of conjugated polymers were preferentially aligned on the substrate surface in lamellar packing. The lamellar packing of polymer chains suggests that the polymer film may be uniaxial (optical axis perpendicular to the film plane) or biaxial (one optical axis is perpendicular to the film plane and the other

Reproduced with permission of the copyright owner. Further reproduction prohibited without permission.

optical axis is in the film plane). Through adjustment of the incident angle of light, we observed the angle dependence of the optical properties of the spin-cast P3HT and MEH-PPV film, which suggests the presence of an optical axis perpendicular to the film plane. Meanwhile, we radially rotated (rotated by optical axis) the film by ~45° and no dependence of the optical properties of the film was demonstrated, suggesting that there is no optical axis in the polymer film plane. Therefore, the spin-cast P3HT and MEH-PPV films are uniaxial anisotropic films.

6.2 The Principle of Spectroscopic Ellipsometry

Ellipsometry is a very sensitive measurement technique that uses the polarized light (all light waves are vibrating in the same direction) to characterize thins films, surfaces, and microstructures of materials. By detecting the relative phase change in a beam of reflected polarized light, we can derive the information for index of refraction, and dielectric constant when the film thickness is known, or thickness of the thin film when refraction index or dielectric constant is known.

The ellipsometer, shown schematically in Fig.6-2, consists of a light source, a polarizer and a quarter wave plate which provide a state of polarization which can be varied from linearly polarized light to elliptically polarized light to circularly polarized light by varying the angle of the polarizer. When two waves with the same amplitude and 90° out of phase are combined, the tip of the combined electric field moves along the circumference of a circle. When two waves of the same optical frequency but of different amplitudes and different phases are combined, the tip of the combined electric field would appear to be moving along an ellipse. Through the change of electric field E_s and E_p, one can deduce the complex refractive index parallel to (ordinary or in-plane

Reproduced with permission of the copyright owner. Further reproduction prohibited without permission.

refractive index given in complex form $n_{\|} + ik_{\|}$) or perpendicular to the polymer sample film plane (extraordinary or out-of-plane refractive index given in complex form $n_{\perp} + ik_{\perp}$) as shown in Fig.6-3 [104].

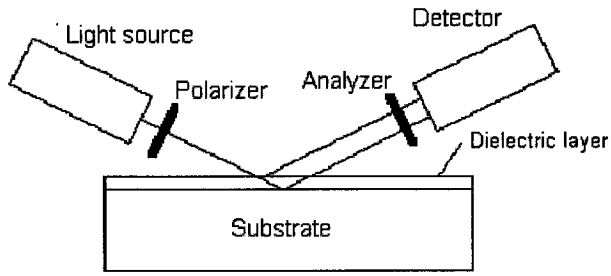

Fig.6-2 The schematic layout of a spectroscopic ellipsometer.

When an electromagnetic wave with field constant $\vec{E}$ interacts with a molecule of a semiconducting polymer, the local field strength at the polaron is different from the field strength in free space because of the interaction with the polymer chain. Through the adjustment of the angle of incident light, we can obtain the angle-dependent optical and electrical properties of the polymers.

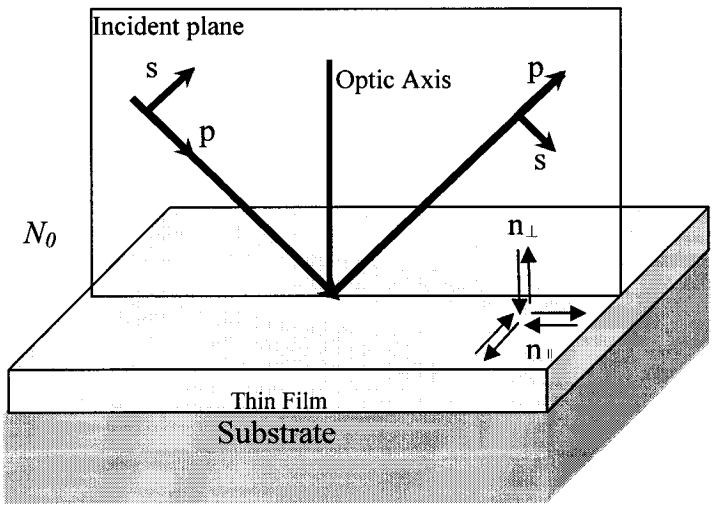

Fig.6-3 The plane of incidence is defined as the plane which contains incoming beams and outgoing beams. The electric field has two components, one parallel to the plane of incidence E_P and the other perpendicular to the plane of incidence E_S. The $n_{\|}$ and $n_{\perp}$ refer to the in-plane and out-of-plane refractive indices of a uniaxial anisotropic film, respectively. Optical axis is normal to the film plane.

Reproduced with permission of the copyright owner. Further reproduction prohibited without permission.

6.3 Sample Preparation

The P3HT thin film was spincast from purified solutions of rr-P3HT with M_W=87,000 g mol^{-1} (Sigma-Aldrich) in chloroform (5mg/ml) onto a (100) silicon wafer. Similarly, MEH-PPV with M_W=70,000-100,000 g mol^{-1}(Sigma-Aldrich) thin film was spin-cast from 8mg/ml chloroform solutions onto a (100) silicon wafer. The silicon substrate was naturally oxidized in the air with an ultra-thin oxide layer of 2.65nm, which was measured with the ellipsometer (Sentech, Germany). The angle of the polarizer was 45° and the incident angles of light were 80°, 70°, 60°, 50° and 40° with respect to the normal direction. The isotropy of the film in the film plane was also checked and proven by radially rotating (rotated by optical axis) the sample by ~45° at an incidence angle of 70°. The results for different incidence angles and radial angles demonstrated the uniaxial anisotropic behavior of the MEH-PPV and the P3HT with respect to the optical axis along the film plane normal.

6.4 Result and Discussion

In ellipsometry it is necessary to know the film thickness for the extraction of the refractive index, dielectric constant, and extinction coefficient. We determined the thickness of the P3HT film by fitting experimental data from 700-800nm, in which the extinction coefficient k is equal or very close to zero due to no optical absorption within 700-800 nm. We used the Cauchy model to find starting values of thickness and refractive index. The thickness obtained by fitting experimental data obtained from ellipsomerty is close to the thickness measured with a Tencor profilometer. The fitting process is accomplished using embedded software in the Sentech ellipsometor (Germany).

Reproduced with permission of the copyright owner. Further reproduction prohibited without permission.

Additional P3HT and MEH-PPV samples were spin-cast on a quartz slide for UV/Vis absorption measurements with a UV/Vis spectrometer (Agilent Technology).

6.4.1 MEH-PPV optical parameters obtained by ellipsometry

The complex refractive index of a material is expressed by $\vec{n} = n + ik$. For the in-plane direction, the complex refractive index is given by $\vec{n}_{\perp} = n_{\perp} + ik_{\perp}$. For out-of-plane direction, the complex refractive index is expressed by $\vec{n}_{\parallel}=n_{\parallel}+ik_{\parallel}$ The real part of complex refractive index n is usually called refractive index, and the imaginary part k is called extinction coefficient. The spectral dependence of refractive indices and extinction coefficients of MEH-PPV in the wavelength range between 350 nm and 800nm, which are plotted in Fig.6-4 and Fig.6-5, are obtained by fitting experimental results and theoretical models.

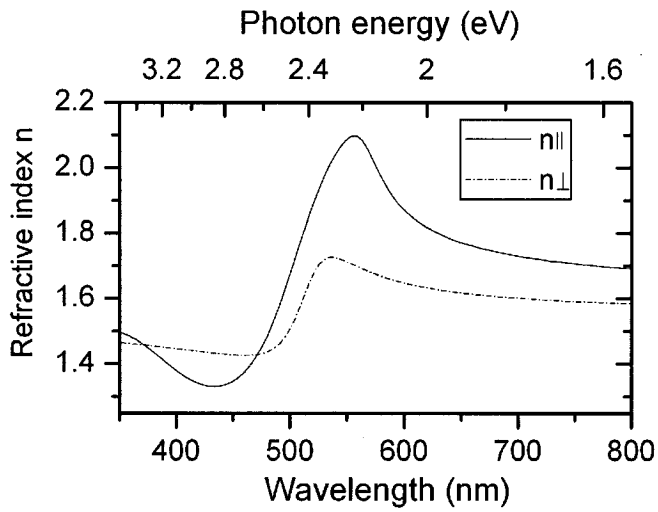

Fig.6-4 The in-plane (solid line) and out-of-plane (dashed line) refractive indices of spin-cast MEH-PPV film in the wavelength range between 350 nm and 800nm.

Reproduced with permission of the copyright owner. Further reproduction prohibited without permission.

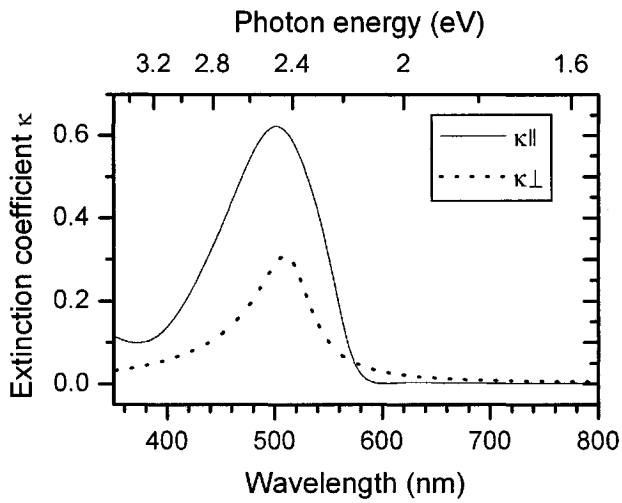

Fig.6-5 The in-plane (solid line) and out-of-plane (dotted line) extinction coefficients of spin-cast MEH-PPV film in the wavelength range between 350 nm and 800nm.

Based on Eq. (6-1) we obtained the spectral dependence of the in-plane and out-of-plane absorption coefficients of MEH-PPV as shown in Fig.6-6. We also found that this spectral curve of in-plane absorption coefficients $\alpha_{\parallel}$ using ellipsometry is in agreement with the optical density curve using UV/Vis spectrometer.

$$\alpha_{\perp} = \frac{4\pi k_{\perp}}{\lambda} \quad \text{and} \quad \alpha_{\parallel} = \frac{4\pi k_{\parallel}}{\lambda} \qquad (6\text{-}1)$$

where, λ is wavelength of incoming light. The absorption coefficient presents the ability of a material to absorb light. $I = I_0 \exp(-\alpha_{\parallel} \cdot t)$, where, I_0 is incident light intensity, t is film thickness, and I is the outgoing light intensity. For MEH-PPV, the ordinary absorption coefficient at a strong peak at 496nm is 1.56×10^5 cm^{-1} (Fig.6-6). If the thickness of the thin film is 100nm, a typical thickness for a single layer polymer device, the MEH-PPV layer will absorb 79% of the light, without taking other optical effects into consideration. If the thickness of the thin film increases to 200nm, it can almost absorb 96% of incoming light.

Reproduced with permission of the copyright owner. Further reproduction prohibited without permission.

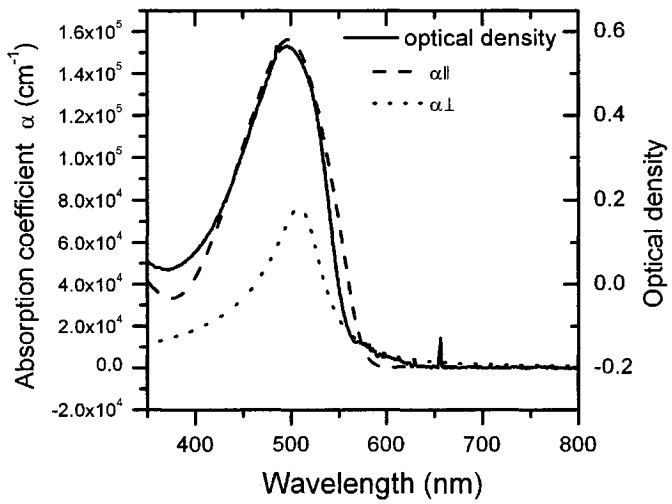

Fig.6-6 The in-plane (dashed line) and out-of-plane (dotted line) absorption coefficients and UV/Vis optical absorption of spin-cast MEH-PPV film in the range of 350nm-800nm. The absorption of MEH-PPV film (solid line) is obtained with UV/Vis spectrometer.

The in-plane and out-of-plane dielectric constants $\varepsilon_{\parallel} = \varepsilon_{1\parallel} + i\varepsilon_{2\parallel}$ and $\varepsilon_{\perp} = \varepsilon_{1\perp} + i\varepsilon_{2\perp}$, as a function of frequency or wavelength, depend sensitively on the electronic band structure of a crystal. However, these constants can not be directly obtained from experiment, but must be calculated from refractive index n and extinction coefficient k based on Eq. (6-2) to (6-4). The spectral dependences of the real part and imaginary part of the complex dielectric constant of MEH-PPV are shown in Fig.6-7 and Fig.6-8.

$$\varepsilon = n^2 \tag{6-2}$$

$$\varepsilon_1 = n^2 - k^2 \tag{6-3}$$

$$\varepsilon_2 = 2nk \tag{6-4}$$

Reproduced with permission of the copyright owner. Further reproduction prohibited without permission.

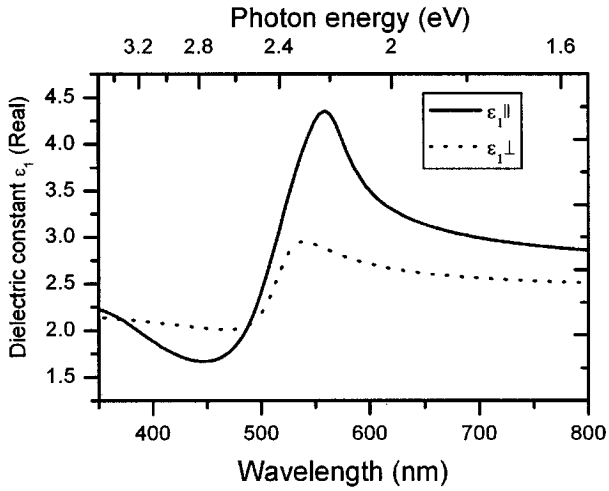

Fig.6-7 The in-plane (solid line) and out-of-plane (dotted line) real part of the complex dielectric constant of spin-cast MEH-PPV film in the wavelength range between 350 nm and 800nm.

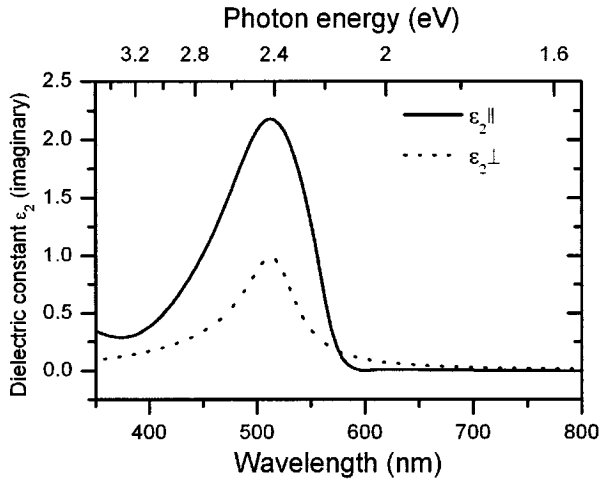

Fig.6-8 The in-plane (solid line) and out-of-plane (dashed line) imaginary part of the complex dielectric constant of spin-cast MEH-PPV film in the wavelength range between 400 nm and 800nm.

6.4.2 P3HT optical parameters obtained by ellipsometry

The spectral dependence of in-plane complex refractive indices $\vec{n}_{\|}=n_{\|}+ik_{\|}$ and out-of-plane complex refractive indices $\vec{n}_{\perp}=n_{\perp}+ik_{\perp}$ of the P3HT film are plotted in Fig.6-9 and Fig.6-10. In Fig.6-9 we can observe that in-plane refractive indices $n_{\|}$ has a minimum near 452nm (2.7eV), a shoulder at 600nm, and a maximum near 624nm (2.0eV)

Reproduced with permission of the copyright owner. Further reproduction prohibited without permission.

close to the absorption onset at 640nm (1.9 eV). The in-plane $k_{\|}$ has a shoulder that is the same as $n_{\|}$ and a peak at ~514nm (~2.4eV), which is in agreement with the optical absorption of poly(octylthiophene) shoulder reported by Ref.[100]. The out-of-plane $k_{\perp}$ may be attributed to the intermolecular transitions because of the formation of aggregation [103]. This assumption was proven through the work of Miller et al [97] and Tammer [94] .

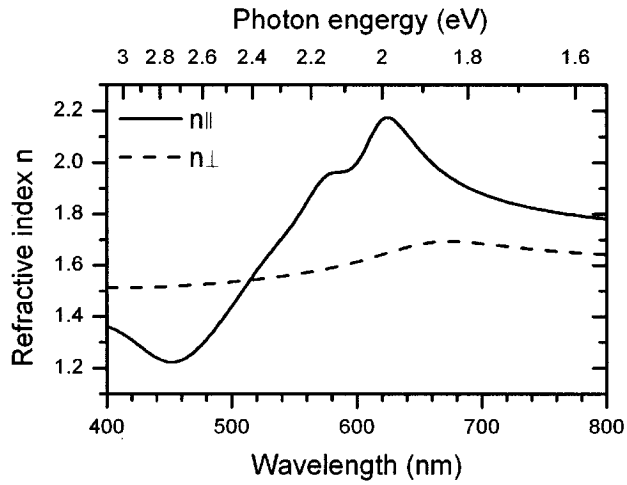

Fig.6-9 The in-plane (solid line) and out-of-plane (dashed line) refractive index of spin-cast P3HT film in the wavelength range between 400 nm and 800nm.

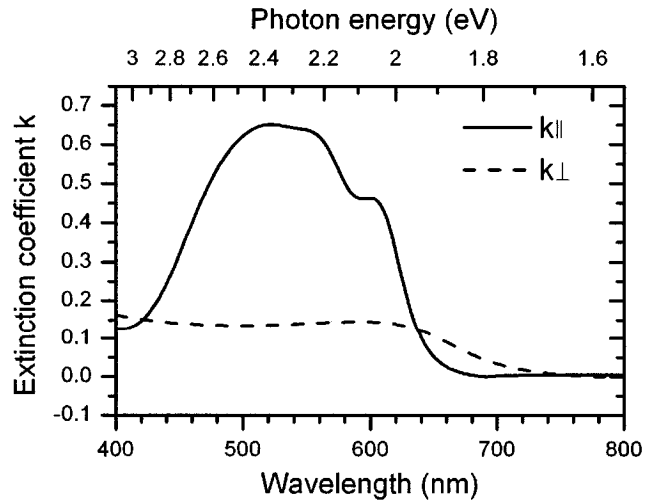

Fig.6-10 The in-plane (solid line) and out-of-plane (dashed line) extinction coefficient of spin-cast P3HT film in the wavelength range between 400 nm and 800nm.

Reproduced with permission of the copyright owner. Further reproduction prohibited without permission.

Based on Eq.(6-1) we obtained the absorption coefficient of P3HT which is shown in Fig.6-11. The in-plane absorption $\alpha_{\|}$ has a peak at ~514nm, and optical absorption onset at ~650nm, indicating an optical bandgap of ~ 1.9 eV. At around 600nm $\alpha_{\|}$ has a broad shoulder, ~15nm wide. At room temperature, such a shoulder can be observed in the $\alpha_{\|}$ of a polythiophene derivative, poly(octylthiophene), with a different side group [100]. So we can conclude that the $\alpha_{\|}$ shoulder results from the thiophene backbone, not from the side group. We also compared this absorption coefficient curve obtained from ellipsometry and the absorption spectrum obtained with UV/Vis spectrometer. We can see the absorption coefficient of P3HT film obtained by ellipsometry is blueshifted from the absorption peak of P3HT solution by ~ 8 nm (or ~0.04 eV). This indicates that the molecular chain is more extended in solution and has a longer conjugation length.

In dielectric material, there are several major microscopic mechanisms of polarization: electronic, ionic, orientational, interfacial and ferroelectric, which are frequency dependent [105]. Among these polarizations, electronic polarization is expected to occur at optical wavelength. Therefore, we can obtain the spectral dependence of complex dielectric constants according to Eq. (6-2)-(6-4).

Reproduced with permission of the copyright owner. Further reproduction prohibited without permission.

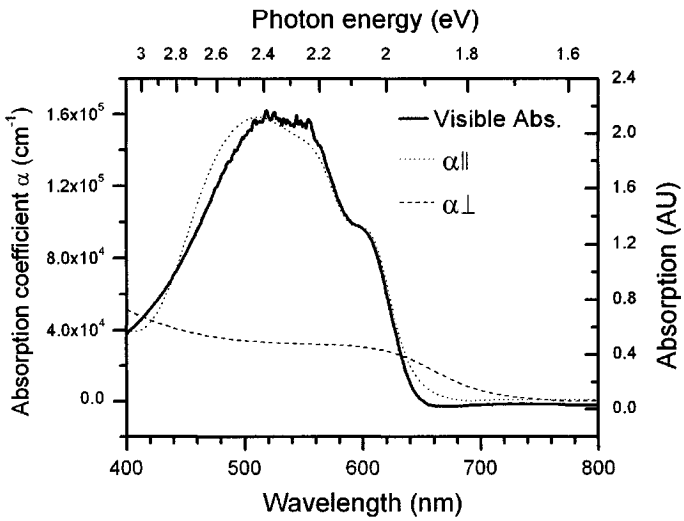

Fig.6-11 The in-plane (dashed line) and out-of-plane (dotted line) absorption coefficients and UV/Vis optical absorption of spin-cast P3HT film in the wavelength range between 400 nm and 800nm. The absorption of P3HT solution (solid line) is obtained with UV/Vis spectrometer.

Fig.6-12 depicts spectral dependence of real part of complex dielectric constant ε_1 for in-plane and out-of-plane directions. Fig.6-13 shows the spectral dependence of imaginary part ε_2 of the dielectric constants at in-plane and out-of-plane direction.

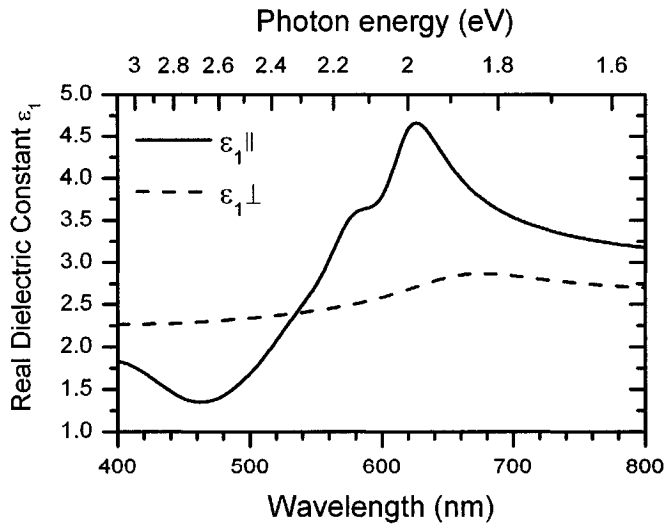

Fig.6-12 The in-plane (solid line) and out-of-plane (dashed line) real part of the complex dielectric constant of spin-cast P3HT film in the wavelength range between 400 nm and 800nm.

Reproduced with permission of the copyright owner. Further reproduction prohibited without permission.

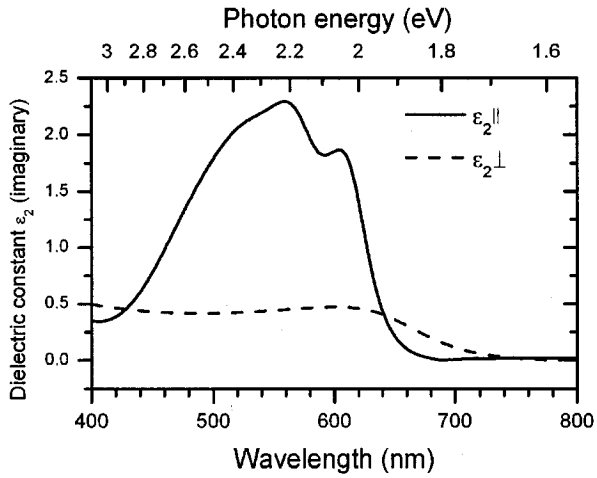

Fig.6-13 The in-plane (solid line) and out-of-plane (dashed line) imaginary part of the complex dielectric constant of spin-cast P3HT film in the wavelength range between 400 nm and 800nm.

6.4.3 Summary

Further we used the angular distribution *d* to describe chain orientation, as defined by [103][106]:

$$d = \frac{1}{1 + k_{out-of-plane} / 2k_{in-plane}} \qquad (6\text{-}5)$$

If the polymer is an isotropic material, $k_{\perp} / k_{\parallel} = 1$ and then *d*=2/3. If the chain is lamellar (molecule chain lying in the film plane), $k_{\perp} / k_{\parallel} = 0$ would approach 0 and then $d \rightarrow 1$. A much larger angular distribution *d* indicates more uniform distribution of material. The angular distribution of spincast MEH-PPV film are ~0.81 for 514.5nm light as reported by McBranch et al [106], ~0.91 from 400nm to 600nm as reported by Tammer [93], and ~0.8 at ~514nm from our ellipsometric measurements . The variation of *d* reflects the influence of processing technique on chain orientation. For our P3HT samples, *d* is from 0.86-0.9 at 400nm-600nm, which strongly supports that P3HT is a rigid rod-like polymer, with approximately same level of chain order as in the MEH-PPV

Reproduced with permission of the copyright owner. Further reproduction prohibited without permission.

film reported by Ref. [93]. The spin-coating process can not provide a highly oriented rr-P3HT film as the method with polyethylene (PE) mentioned in [97][98].

In Table 6-1 and Table 6-2 we will give the optical and electrical properties of MEH-PPV and P3HT at specific wavelengths. The parameters will be used for the optimization of the device structure discussed in Chapter 8 and 9 and for the comparison of P3HT and MEH-PPV.

Table 6-1 The refractive indices, extinction coefficients, complex dielectric constants, absorption coefficients, and angular distributions of spin-cast P3HT film at specific wavelengths.

Wavelength →	496 nm	514 nm(peak)	600 nm(shoulder)
$n_{\parallel}$	1.41	1.54	2.00
$n_{\perp}$	1.53	1.54	1.61
$k_{\parallel}$	0.61	0.65	0.46
$k_{\perp}$	0.14	0.14	0.15
$\varepsilon_{1\parallel}$	1.62	1.94	3.79
$\varepsilon_{1\perp}$	2.33	2.36	2.59
$\varepsilon_{2\parallel}$	1.72	1.99	1.85
$\varepsilon_{2\perp}$	0.42	0.42	0.47
$\alpha_{\parallel}(cm^{-1})$	$1.5x10^5$	$1.6x10^5$	$0.97 x10^5$
$\alpha_{\perp}(cm^{-1})$	$0.34 x10^5$	$0.33 x10^5$	$0.31 x10^5$
d	0.90	0.90	0.86

In Table 6-3 we summarize the anisotropy ratio of refractive indices, dielectric constants and absorption coefficients of MEH-PPV and P3HT at the absorption peak. For the absorption peak for P3HT at 514nm, the ratio of in-plane to out-of-plane refractive index, extinction coefficient, absorption coefficient, real dielectric constant and imaginary dielectric constant is 1, 4.6, 4.85, 0.82, and 4.7, respectively. For MEH-PPV at the absorption peak of 496nm, these values became as 1.1, 2.3, 2.3, 1.1 and 2.48, respectively. The anisotropy ratio of the extinction coefficient of P3HT is higher than that of MEH-PPV. As we discussed in Section 7.4.2, the higher anisotropy ratio of the

Reproduced with permission of the copyright owner. Further reproduction prohibited without permission.

extinction coefficient indicates a stronger intermolecular transition and more molecular aggregation. Therefore, P3HT should have a higher self-organization than MEH-PPV, which is in good agreement with the experimental results of P3HT obtained with x-ray diffraction measurement [90].

Table 6-2 The refractive indices, extinction coefficients, complex dielectric constants, absorption coefficients, and angular distributions of spin-cast MEH-PPV film at specific wavelengths.

Wavelength →	496 nm (peak)	520 nm	560 nm
$n_{\parallel}$	1.63	1.89	2.10
$n_{\perp}$	1.48	1.68	1.70
$k_{\parallel}$	0.62	0.56	0.21
$k_{\perp}$	0.27	0.27	0.08
$\varepsilon_{1\parallel}$	2.27	3.27	4.36
$\varepsilon_{1\perp}$	2.12	2.74	2.88
$\varepsilon_{2\parallel}$	2.01	2.14	0.86
$\varepsilon_{2\perp}$	0.81	0.92	0.27
$\alpha_{\parallel}(cm^{-1})$	1.6×10^5	1.4×10^5	4.6×10^5
$\alpha_{\perp}(cm^{-1})$	0.69×10^5	0.66×10^5	0.18×10^5
d	0.82	0.81	0.84

Table 6-3 The anisotropy ratio of refractive indices, dielectric constants, and absorption coefficients of MEH-PPV and P3HT.

Polymer →	MEH-PPV (496 nm)	P3HT (514 nm)
$n_{\parallel}/n_{\perp}$	1.1	1
$k_{\parallel}/k_{\perp}$	2.3	4.6
$\alpha_{\parallel}/\alpha_{\perp}$	2.3	4.6
$\varepsilon_{1\parallel}/\varepsilon_{1\perp}$	1.1	0.8
$\varepsilon_{2\parallel}/\varepsilon_{2\perp}$	2.48	4.7

6.5 Conclusion

In this chapter we introduced the principle of spectroscopic ellipsometry and the basic configuration of an ellipsometer. We prepared MEH-PPV and P3HT thin film through spin-casting. With the measurement results at an incident angle of 40°, 50°, 60°, 70°, 80°, we deduced the index of refractive and extinction coefficient of MEH-PPV and

Reproduced with permission of the copyright owner. Further reproduction prohibited without permission.

P3HT at extraordinary (out-of-plane) and ordinary (in-plane) directions. We found that both MEH-PPV and P3HT films show a strong anisotropy due to the orientation of the molecule chain. We reported the spectral dependence of complex refractive indices, complex dielectric constants, and absorption coefficients of spin-cast P3HT film and MEH-PPV film. The high angular distribution demonstrates that the P3HT and MEH-PPV film are rigid rod-like polymers. This information will be used in the optical design of the diffraction grating in solar cells and photodetectors.

Reproduced with permission of the copyright owner. Further reproduction prohibited without permission.

CHAPTER 7

PHOTODETECTORS WITH GRATING STRUCTURES

7.1 Introduction

Photo-generated excitons need to be dissociated to free charge carriers under applied electric field. The efficient dissociation of the excitons in the polymer always happens at the interface between donor (D) and acceptor (A), or the interface between polymer and metal contact. If the width of such an interface is comparable to an exciton diffusion length (L_D), the exciton dissociation efficiency can approach unity for a D/A structure like MEH-PPV and PCBM. However, the diffusion length L_D of an exciton of polymer is typically shorter (L_D=20nm for MEH-PPV) than its optical absorption length (~200nm for MEH-PPV). This requires the use of highly folded interfaces or multiple optical path length for incident light through the thin light-absorbing polymer film. The diffraction grating is the kind of structure that can meet both requirements. With the grating structure or light-trapping structure, higher efficiencies have been attained at EQE≈ IQE.

The diffractive grating has been widely used in lasers and waveguides for the application of optical communication. It can couple incoming light at different diffractive angles. By choosing the suitable period and depth, we can couple the light, as we desired, to be parallel to the longitudinal direction of thin film which is what we desire. The light

Reproduced with permission of the copyright owner. Further reproduction prohibited without permission.

absorption is not limited by the thin film thickness, but by the cell size. The diffractive grating has been used in Si-based solar cells [107]. This approach has been applied to polymer-based solar cells and lead to promising results [108][109]. Based on the optical properties of the diffraction grating, the photoconductivity in solar cells and photodetectors for a certain interval of spectrum are expected to increase.

7.2 Principle of Optical Grating

A beam of light which falls on a grating will be diffracted into one or several beams as shown schematically in the Fig.7-1. The directions of these beams depend on the wavelength and the direction of the incident beam, and on the groove period of the grating. The relationship between the incidence and diffraction angles and the wavelength is given by

$$\sin\alpha + \sin\beta_m = -m\lambda/\Lambda \qquad (7\text{-}1)$$

where: α is the angle of incidence; β_m is the angle of diffraction. The angles are positive if they are directed counter-clockwise, and negative otherwise; m is the order number of the diffracted beam; m is an integer number, positive, negative or zero; Λ is the groove period of the grating; λ denotes the wavelength of the light in the medium surrounding the grating.

For the reflection grating, the equation reduces to $\alpha=\beta_0$ or the law of reflection when m=0. There will always be this solution and therefore a reflected beam, which is usually not desirable. For the transmission grating, the solution at m=0 corresponds to a transmitted beam. The reflected or transmitted beam is the major cause of light losses in the reflection or transmission grating. The diffracted order with m=1 is the order normally

Reproduced with permission of the copyright owner. Further reproduction prohibited without permission.

used in monochromators, spectrographs, and spectrometers, and is also the order that we want in the polymer photodetectors or solar cells.

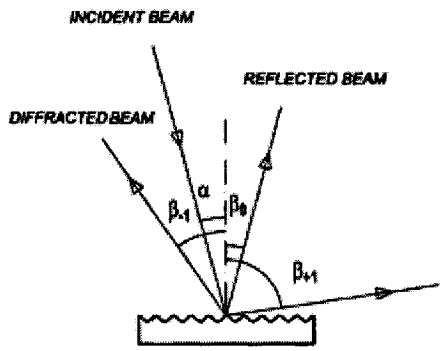

Fig.7-1 Diffraction at the surface of a plane grating. The grating is depicted with the grating grooves perpendicular to the paper and the collimated monochromatic beams are propagating in the plane of the paper.

The grating can be classified into three groups: blazed grating, sinusoidal grating and laminar (or binary) grating according to the profile of the grating cross-section, as illustrated in Fig.7-2. According to the function of the grating, the grating can also be classified as reflection and transmission gratings. The transmission grating does not have a reflective metal coating and the incident light is diffracted upon transmission through the grating. The grating used in our polymer photodetectors acts as a transmission grating in the visible light range.

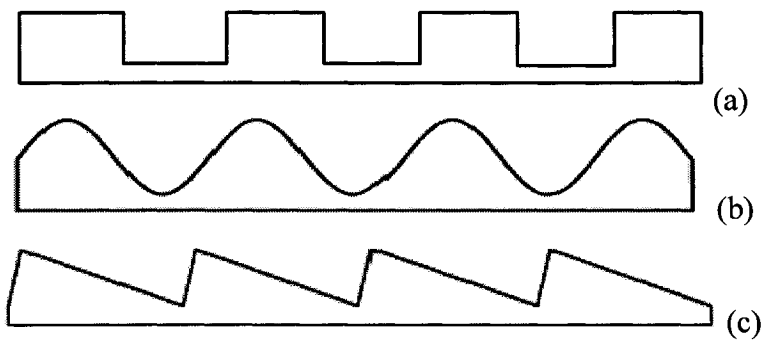

Fig.7-2 Three common groove profiles (the grating is shown in cross-section). (a) a laminar (or binary) profile; b) a sinusoidal profile; (b) a triangular (or blazed) profile.

Reproduced with permission of the copyright owner. Further reproduction prohibited without permission.

7.3 Fabrication of Devices

A silicon master grating was patterned through interference photolithography and fabricated with reactive ion etching (RIE) (Courtesy of Southern Methodist University). The grating stamp was made of polydimethylsiloxane (PDMS) elastomer with the method mentioned in Ref.[110]. Later, we used the PDMS stamp to pattern PEDOT: PSS layer. Once PEDOT: PSS film was spin-cast, in short duration, to keep some residual solvent, we placed the PDMS stamp on the polymer film surface and left the samples in air for 24 hours to completely remove the residual solvent. The morphology of the grating structure was scanned with Atomic Force Microscope (AFM). When the PEDOT:PSS grating was completed, a light-sensitive blended polymer film was spincast from a MEH-PPV (Sigma-Aldrich) and PCBM (ADS) mixture solution (weight ratio of 3 to 1 in chlorobenzene) onto the grating surface. After overnight drying in a vacuum chamber, a 100 nm Al film was thermally evaporated onto the light-sensitive polymer film. The configuration of polymer photodetectors with grating structure is shown in Fig.7-3. The devices were tested in air. The testing followed the procedures described in Section 3.2 of this thesis.

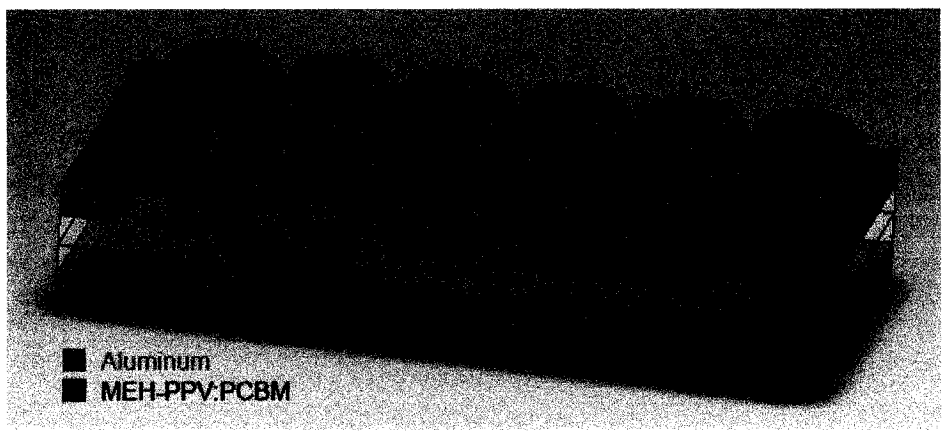

Fig.7-3 The configuration of Glass/ITO/PEDOT:PSS (with grating)/MEH-PPV:PCBM (3:1)/Al photodetectors.

Reproduced with permission of the copyright owner. Further reproduction prohibited without permission.

7.4 Theoretical Model and Numerical Simulation of Structure with Optical Grating

Lamellar gratings have been applied in spectrometry and optical communication. The theoretical model of the lamellar grating had been first investigated by Moharam and Gaylord using the rigorous coupled-wave analysis (RCWA) method [111]. RCWA has been demonstrated to be an effective and accurate method to obtain the information for backward and forward diffraction space-harmonic wave since twenty years. In 1995, Moharam further developed a general formulation in matrix form under TM mode, TE mode and cone mode [112], which is given in the Appendix A of this thesis. By using a conventional eigenvalue solver, we can solve the magnitudes for a space-harmonic field.

However, the groove profile of the fabricated silicon master was not exactly lamellar as we had designed, but more like a quadrangle due to the over-cutting effect of the RIE process, which may be the cause of the disagreement between the theoretical and experimental results.

There are several decisive parameters that need to be considered when designing a grating, e.g. the dielectric function of the material (determined using ellipsometry), the wavelength (λ), the incident angle (α), the shape, the depth (d) and the period of the grating (Λ).

The simulation results give the diffraction efficiency in the existing modes and the fraction of light traveling at diffractive angles. In order to illustrate the simulation clearly, we redraw the grating structure surrounding the media of PEDOT:PSS and MEH-PPV shown in Fig.7-3 to that of Fig.7-4.

Reproduced with permission of the copyright owner. Further reproduction prohibited without permission.

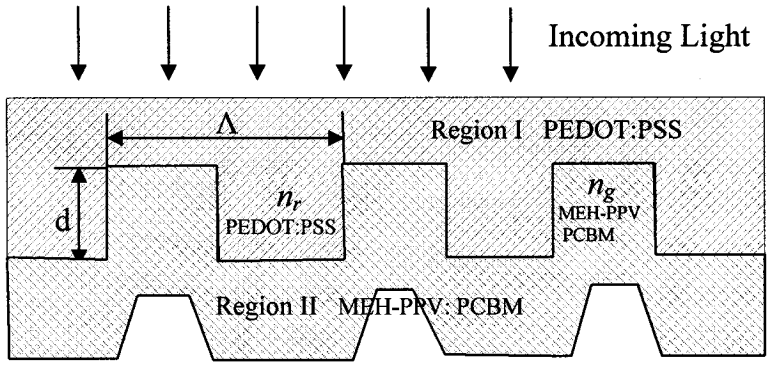

Fig.7-4 The schematic structure of grating on PEDOT: PSS surface, where n_r and n_g is the refractive index of the ridge and the groove, respectively, and d is the groove depth.

It has been shown that the PEDOT: PSS improves the quantum efficiency of polymer solar cells due to the enhancement of charge transport and the reduction of recombination [113]. The surface of ITO is microporous and the porosities can be recombination sites for charge carriers. PEDOT film doped with PSS shows high uniformity and good hole-transport. Thus, the application of PEDOT: PSS layer can reduce the effect of defects in the light-sensitive layer, such as voids, and thus increase the device yield. In Fig.7-4, the grating structure between PEDOT:PSS and MEH-PPV works as a transmission grating. The refractive index n of PEDOT is ~ 1.48 and its extinction constant k is 0.04 at 520nm (for the definition see Section 7.4.1) [114]. As mentioned above, we intentionally used the first diffraction mode (parallel to the film plane) in the polymer photodetector. We can optimize the groove depth by maximizing the diffraction efficiency of the first mode diffractive light. In Fig.7-5 , we present the simulation results of the zero-mode and the first-mode diffraction efficiency of the grating at 520nm using monochromatic light.

Reproduced with permission of the copyright owner. Further reproduction prohibited without permission.

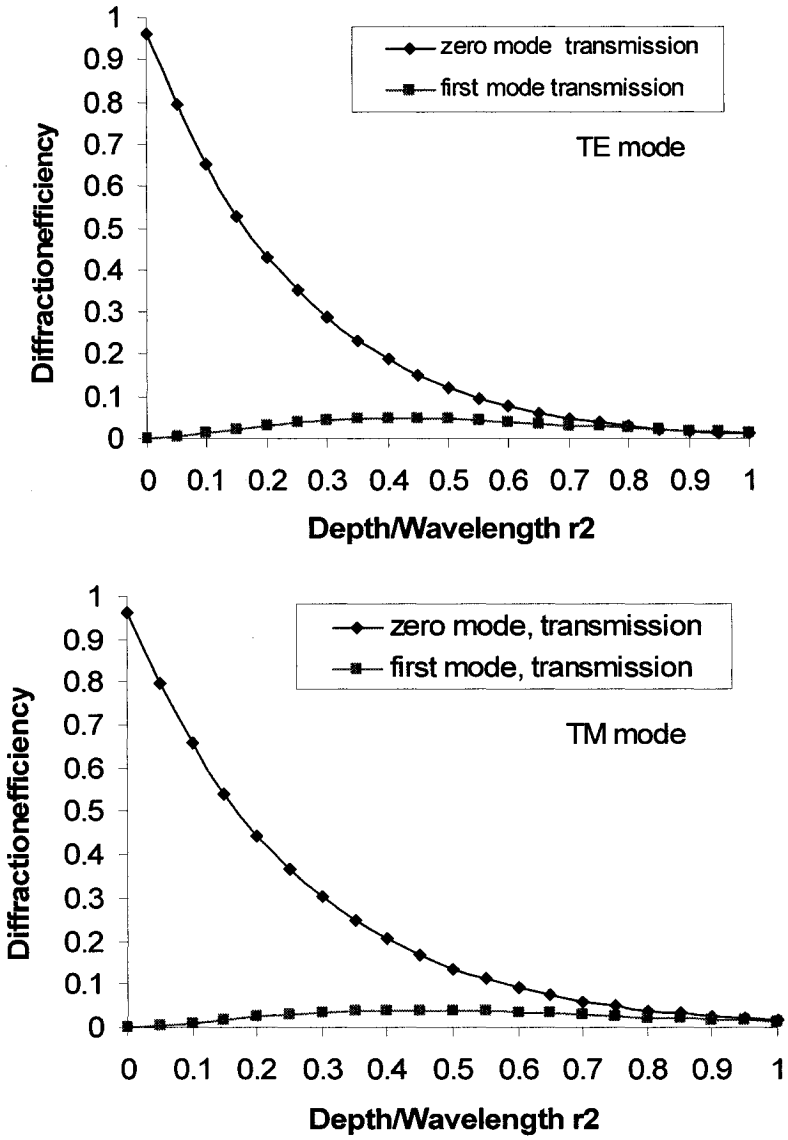

Fig.7-5 The zero-mode and first-mode diffraction efficiency of the grating structure on PEDOT: PSS layer (θ=0, λ=520, Λ/λ=1, f=0.5) at TE mode (upper plot) and at TM mode (lower plot).

From the simulation results in the Fig.7-5 we found that the diffraction efficiency of first mode diffractive light was maximized at the ratio of depth to wavlength r_2=0.4. Thus the groove depth is obtained by $d = r_2 \times \lambda = 208$ nm. Therefore the grating is designed with the period Λ = 520 nm and the depth d = 208 nm.

Reproduced with permission of the copyright owner. Further reproduction prohibited without permission.

7.5 Experimental Results and Analysis

Fig.7-6 shows the 3D morphology of the silicon master, PDMS stamp and PEDOT grating scanned with the AFM. Due to difficulty with the fabrication process, the actual depth of silicon grating is 64±2 nm, much less than we designed for. The depth of the PDMS stamp and PEDOT grating are 58±2 nm and 44±2 nm. The replication accuracy in making PDMS stamp is around 91%. The replication accuracy can be further increased by tailoring the viscosity of the PDMS. When stamping the grating on the PEDOT layer, we can apply suitable pressure to ensure good contact between the PDMS stamp and the PEDOT film.

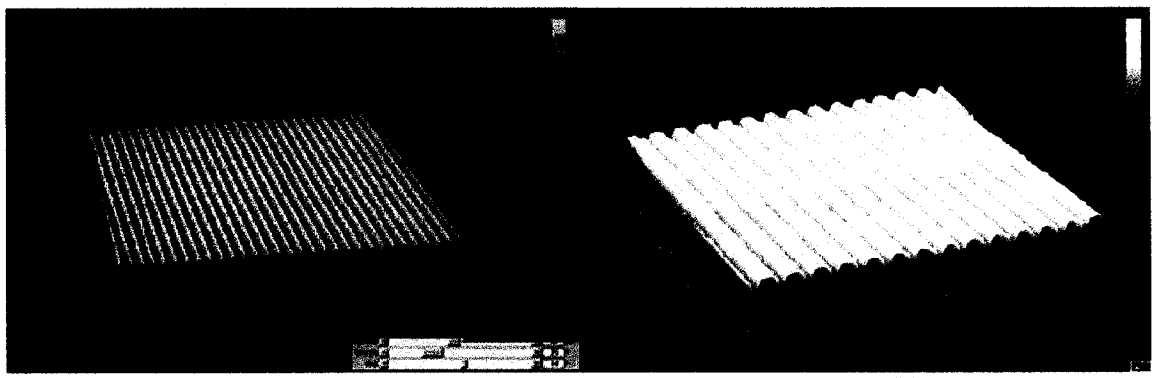

(a) (b)

(c)

Fig.7-6 The AFM image of the Silicon master (a), the PDMS stamp (b), and the PEDOT grating (c).

Reproduced with permission of the copyright owner. Further reproduction prohibited without permission.

Fig.7-7 shows dark and light current-voltage characteristics for MEH-PPV: PCBM photodetectors with/without grating structure at 490 nm with light intensity of 362 $\mu W/cm^2$. Fig.7-8 shows the spectral dependence of EQE for MEH-PPV: PCBM photodetectors with/without grating structure on the PEDOT:PSS layer. From Fig.7-7 and Fig.7-8 we can not see any enhancement of photoconductivity after introducing the grating structure. The possible reasons are: a) The groove is not deep enough. The fabricated grating in the polymer is shallower then the grove we designed; b) incoming light deviated from the normal of the substrate plane and is refracted when traveling through the medium of glass substrate and ITO layer and thus the incident angle at the grating interface is not along the normal of the surface. The deviation of incident angle at the grating interface leads to an expected deviation from the theoretical model; c) The actual profile of the PEDOT grating is not highly consistent with the profile used in numerical simulation, thereby the actual grating profile affects the dielectric matrix ε_h (ε_h is the h^{th} Fourier component of the relative permittivity in the grating region, see Appendix A) that results in the deviation in theoretical and experimental results; d) This theoretical model had been proven to be in good agreement with experimental results for lossless grating. However, one medium of the grooves surrounding the grating region, as shown in Fig.7-4, is a light-absorbing material, MEH-PPV. Therefore, whether this model is suitable for our case with a lossy grating merits further investigation.

Reproduced with permission of the copyright owner. Further reproduction prohibited without permission.

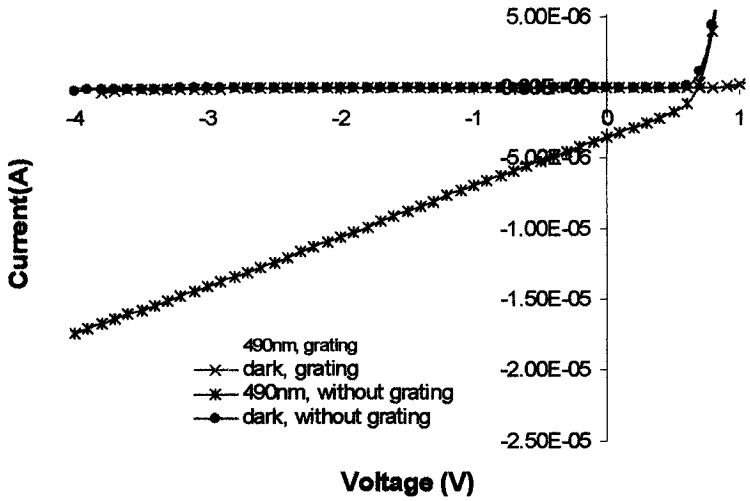

Fig.7-7 The dark and light IV curve of MEH-PPV:PCBM photodetectors with/without the grating structure on PEDOT:PSS layer. The incident monochromatic light is at 490nm with light power density of 362 $\mu W/cm^2$.

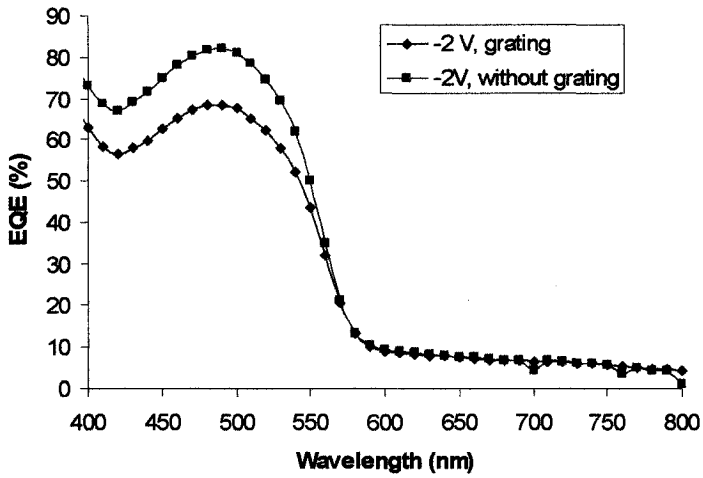

Fig.7-8 The EQE curve, as a function of wavelength, of MEH-PPV: PBCM device with/without grating on the PEDOT: PSS layer.

7.6 Conclusion and Future Work

In this chapter, we designed and simulated diffraction grating on the PEDOT:PSS layer, and successfully realized the grating pattern transferring from silicon master to PEDOT layer in the MEH-PPV:PCBM photodetectors by soft lithography. From the IV

Reproduced with permission of the copyright owner. Further reproduction prohibited without permission.

characteristics and EQE curve of polymer photodetectors with/without grating we can not find enhancement of photoconductivity. The possible reasons may be: a) the groove is not as deep as what we designed due to difficulty with fabrication process; b) the incoming light is not perpendicular to the grating interface because the refraction happens at the interfaces of air/glass, glass/ITO and ITO/PEDOT; c) the actual profile of the PEDOT grating is not highly consistent with the profile used in numerical simulation; d) this theoretical model is in good agreement with experimental results for lossless grating, but not for a lossy grating. In the future works, we may increase the replication accuracy of the grating structure and make modifications to the theoretical model for lossy grating.

Reproduced with permission of the copyright owner. Further reproduction prohibited without permission.

CHAPTER 8

THE SIMULATION OF POLYMER PHOTODETECTOR ELECTRICAL CHARACTERISTICS

8.1 Introduction

We have designed, fabricated and tested several kinds of polymer photodetectors, described in Chapter 3-5 and Chapter 7. In this chapter we investigated the mechanisms of charge drift and diffusion in the polymer-based photodetector. It is important for us to have deeper understanding of the electrical characteristics of polymer photodetectors. We discussed the electrical characteristics in two ways: by establishing analytical model and by using the commercial simulation package T-CADs (Synopsys Company).

In the first part of the chapter, we mainly paid attention to establish the analytical model for photogenerated current density with the steady-state continuity equation. The diffusion model has been used in modeling the photocurrent action of polymer solar cells. However, for polymer photodetector that is operated at reverse bias, the photocurrent and quantum efficiency show an electrical field dependence from our measurement results. Therefor we introduced a field-dependent factor into the model for photocurrent density of the photodetector.

Later we used T-CAD distributed by Synopsys Company to simulate the dark and light current-voltage characteristics of a pure MEH-PPV photodetector. MEDICI and TAURUS can be both used to simulate the electrical characteristics of semiconductor

Reproduced with permission of the copyright owner. Further reproduction prohibited without permission.

devices. However, the second-development power or customer-defined models in TAURUS is more powerful than that of MEDICI. The very important models like the mobility model, which can significantly affect the electrical performance of semiconductor devices, need to be carefully established. It has widely been reported that the charge carrier mobility in polymers is electric-field dependent [115]-[120]. The most used mobility model is the Poole-Frenkel-like form [120]. MEDICI provides many mobility models such as concentration-dependent models, temperature-dependent, and field-dependent models. However, these model formulations are not suitable for the case of the Poole-Frenkel-like form. Through the Physical Model and Equation Interface (PMEI) available in TAURUS, we can develop our mobility model and photogeneration model. We used these models to simulate the dark current-voltage characteristics of the single-layer pure MEH-PPV photodetector. Furthermore, we discussed the significant factors that affect the dark I-V characteristics of the detector. For the simulation of light I-V curve, we have a detailed description in Section 8.3.2. Finally, we correlated the simulation results and the measurement results.

8.2 The Analytical Model for Polymer Photodetector

8.2.1 Formulation

The derivation of photocurrent density for a pure MEH-PPV photodetector sandwiched between ITO and Al is described here. The schematic layout of the photodetector is shown in Fig.8-1.

Reproduced with permission of the copyright owner. Further reproduction prohibited without permission.

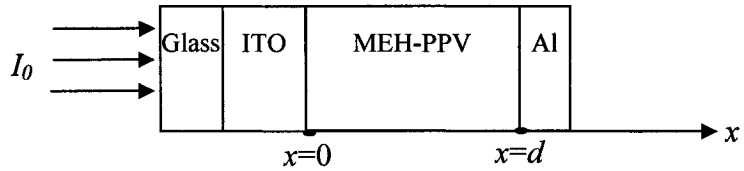

Fig.8-1 The schematic layout of a single layer MEH-PPV photodetector.

This analytical model is derived by the steps: 1) calculating exciton generation rate, 2) setting up steady-state continuity equation, 3) defining the boundary conditions, 4) solving the steady-state continuity equation and giving photocurrent density equation, and 5) modifying the photocurrent density equation with a field-dependent factor.

8.2.1.1 Exciton generation rate

The light absorption of the light-sensitive polymer layer is given by

$$I(\lambda,x) = I_0 \exp[-\alpha(\lambda)\cdot x] \tag{8-1}$$

where, $I(\lambda,x)$: the outgoing optical power density at a specific wavelength (λ) as a function of distance x from the light-active polymer surface (W/cm^2); I_0 (λ): incoming optical power density at a specific wavelength (W/cm^2); $\alpha(\lambda)$: the absorption coefficient at a specific wavelength (cm^{-1}).

After taking the reflection of substrate glass and ITO and absorption efficiency into consideration, the optical power density as a function of distance x from the light-active polymer surface is rewritten as:

$$I(\lambda,x) = \eta_A I_0 \exp[-\alpha(\lambda)\cdot x] \tag{8-2}$$

where η_A is the absorption efficiency, which come from the reflection loss in stacked layers. We assume that one absorbed photon can only generate one exciton (bound hole-electron pair). Thus the generation rate of excitons in the polymer film is obtained by

Reproduced with permission of the copyright owner. Further reproduction prohibited without permission.

$$G_p(\lambda,x)=\frac{\lambda}{hc}\cdot\eta_A\cdot\alpha(\lambda)\cdot I_0(\lambda)\cdot\exp[-\alpha(\lambda)\cdot x]=G_0\exp[-\alpha(\lambda)\cdot x] \qquad (8\text{-}3)$$

where, $G_p(x)$ is the generation rate of exciton at distance x from the surface in $1/(cm^3s)$, h is Plank constant, c is the light velocity, and G_0 is light flux given by:

$$G_0=\frac{\lambda}{hc}\cdot\eta_A\cdot\alpha(\lambda)\cdot I_0(\lambda) \qquad (8\text{-}4)$$

8.2.1.2 Exciton steady-state continuity equation

The absorbed light can generate electron-hole pairs (EHPs). Assuming one absorbed photon can only generate one exciton, no exciton complex like biexciton will be taken into account in the exciton diffusion process [121]. Hereby we assume that the exciton diffusion length is assumed to be independent of the electric field.

We used the 1D steady-state continuity equation to describe the 1D distribution of exciton concentration $e(x)$ in the light-sensitive layer.

$$D_e\frac{d^2e(x)}{dx^2}-\frac{e(x)}{\tau_e}+G_p(\lambda,x)=0 \qquad (8\text{-}5)$$

Eq. (8-5) can be rewritten as

$$-L_e{}^2\frac{d^2e(x)}{dx^2}+e(x)=G_p(\lambda,x)\tau_e \qquad (8\text{-}6)$$

where D_e is the exciton diffusion coefficient, τ_e is the exciton lifetime, $L_e=\sqrt{D_e\tau_e}$ is the exciton diffusion length. The solution of Eq. (8-6) can be found as the sum of the homogeneous and particular solution. The general solution for exciton concentration in the polymer photodetector is given by

Reproduced with permission of the copyright owner. Further reproduction prohibited without permission.

$$e(x) = c_1 e^{-x/L_e} + c_2 e^{x/L_e} + \frac{1}{1 - L_e^{\,2}\alpha^2(\lambda)} G_p(\lambda, x)\tau_e \qquad (8\text{-}7)$$

where c_1 and c_2 are constants determined by the boundary conditions.

8.2.1.3 Boundary conditions

The exciton binding energy is high in polymer photodetectors. From thermodynamics, excitons can only be split into free charges at the interface with enough energy offset. For the pure MEH-PPV photodetector sandwiched between two electrodes, the exciton dissociation sites are only the two interfaces near the electrodes [121] [122]. The boundary condition assumed here is that the interfaces of the active polymer layer near the electrodes act as the perfect sink for the diffused excitons, i.e., all excitons can either recombine or dissociate into free charges at the interfaces, $e(x) = 0\big|_{x=0}$ and $e(x) = 0\big|_{x=d}$, where d is the thickness of the polymer film.

Thus, c_1 and c_2 can be solved according to the boundary condition given above and given by Eq.(8-8).

$$c_1 = \frac{1}{1 - L_e^{\,2}\alpha^2(\lambda)} \frac{e^{d/Le} - e^{-\alpha(\lambda)d}}{e^{-d/Le} - e^{d/Le}} G_0\tau_e$$

$$c_2 = \frac{1}{1 - L_e^{\,2}\alpha^2(\lambda)} \frac{e^{-\alpha(\lambda)d} - e^{-d/Le}}{e^{-d/Le} - e^{d/Le}} G_0\tau_e \qquad (8\text{-}8)$$

and rewrite Eq.(8-7) into

$$e(x) = \frac{1}{1 - L_e^{\,2}\alpha^2(\lambda)} \frac{e^{d/Le} - e^{-\alpha(\lambda)d}}{e^{-d/Le} - e^{d/Le}} G_0\tau_e e^{-x/L_e} + \frac{1}{1 - L_e^{\,2}\alpha^2(\lambda)} \frac{e^{-\alpha(\lambda)d} - e^{-d/Le}}{e^{-d/Le} - e^{d/Le}} G_0\tau_e e^{x/L_e} + \frac{1}{1 - L_e^{\,2}\alpha^2(\lambda)} G_0 e^{-\alpha(\lambda)\tau_e} \qquad (8\text{-}9)$$

Reproduced with permission of the copyright owner. Further reproduction prohibited without permission.

We plot the exciton concentration profile and the gradient of exciton concentration in Fig.8-2 using Eq.(8-9). The parameters used in Fig.8-2 are listed in Table 8-1.

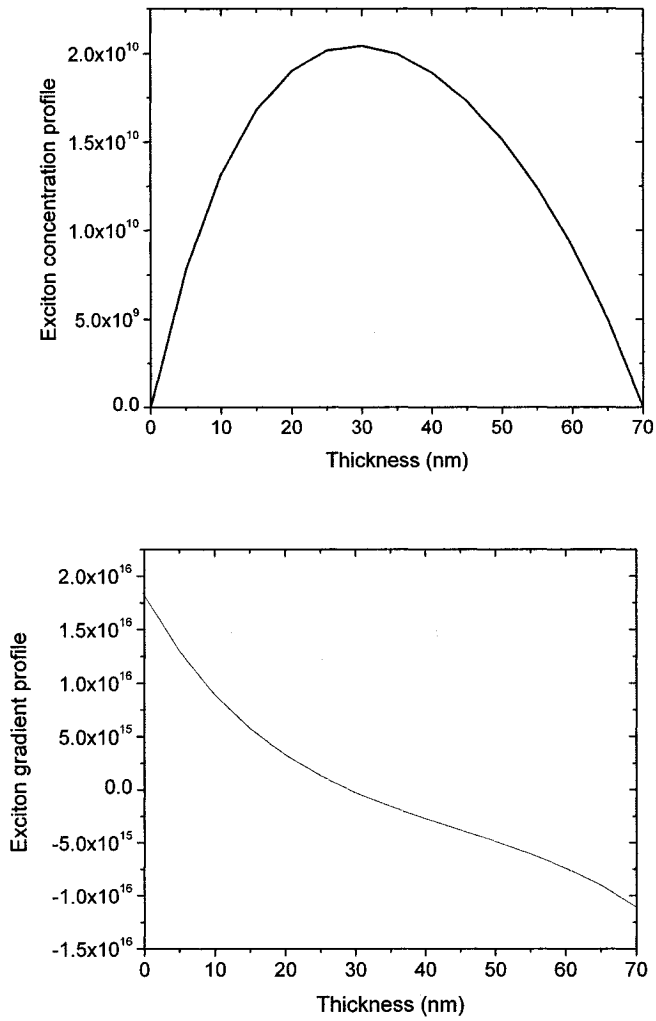

Fig.8-2 The 2D exciton distribution profile (top) and 2D absolute gradient of exciton concentration (bottom) along x-axis (thickness) using Eq.(8-9). The parameters used here are listed in Table 8-1.

In reality, some excitons can be dissociated into free charge carriers in the bulk due to the presence of impurities. These charge carriers in the bulk will finally recombine due to low mobility. Therefore, we only consider that the charge carriers are generated

Reproduced with permission of the copyright owner. Further reproduction prohibited without permission.

within the interfaces. The photocurrent by the diffusion process at the two interfaces is given by (Ref.[121] [122])

$$J_{photo} = \eta_{ED} \cdot \eta_{ES} \cdot \eta_{CC} \cdot q \cdot \frac{L_e^{\,2}}{\tau_e} \cdot \left(\frac{de(x)}{dx}\Big|_{x=0} - \frac{de(x)}{dx}\Big|_{x=d}\right) \tag{8-10}$$

where η_{ED}, η_{ES} and η_{CC} are the exciton diffusion efficiency, exciton dissociation efficiency and charge collection efficiency. According to Peumans's formula [121],

$$\eta_{ED} = \frac{L_e}{d} \frac{[1-\exp(-2d/L_e)]}{[1+\exp(-2d/L_e)]} \tag{8-11}$$

η_{ED} ≈10% for L_e=20nm and d=70nm.

8.2.1.4 Field-dependent factor

From the measured photocurrent data, we found that the photocurrent shows field-dependence. Because EQE is proportional to the photocurrent density, we can determine how the photocurrent density is affected by reverse bias by finding the relationship of EQE versus reverse bias. We found that the semi-log EQE versus voltage bias shows a good linearity, as shown in Fig.8-3. After linearly fitting semi-log EQE vs bias curve for the wavelength range of 400 and 600nm, the relationship of EQE versus bias can be expressed by

$$\eta_{EQE}(V,\lambda) = A(\lambda) \cdot e^{BV} \tag{8-12}$$

where $A(\lambda)$ and B are the empirical values obtained by the linear fitting of semi-log of EQE vs bias for the pure MEH-PPV photodetector. At the same time we also found that parameter A shows spectral dependence and follows the EQE curve pattern, as shown in Fig.8-4. However, parameter B shows a relatively low spectal independence and a factor

Reproduced with permission of the copyright owner. Further reproduction prohibited without permission.

related to reverse bias. Averaged B is about -0.623 V for the wavelength range of 400nm to 600nm.

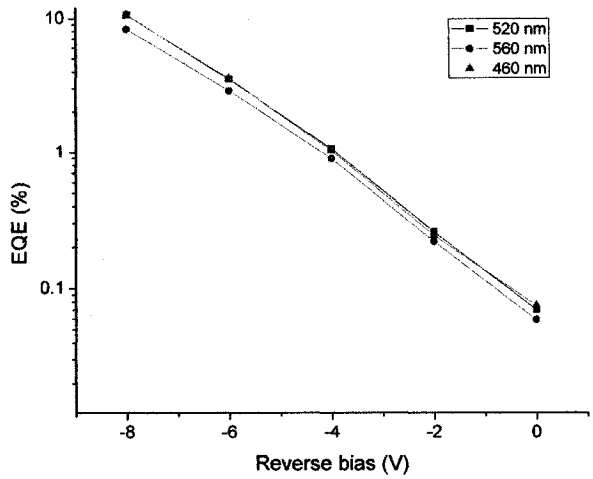

Fig.8-3 The semi-log EQE versus reverse bias at monochromatic wavelength of 460nm, 520nm, and 560nm.

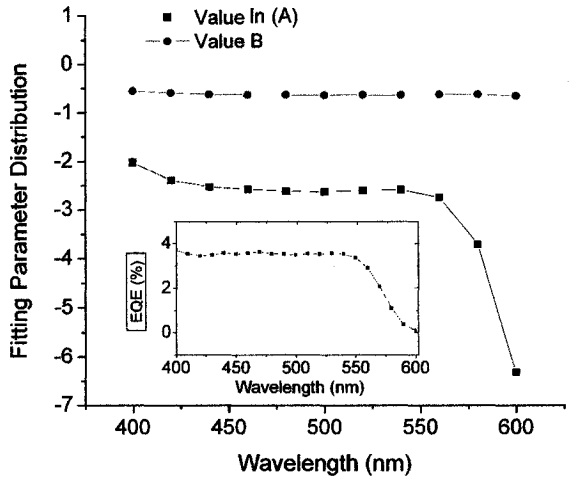

Fig.8-4 The spectral distribution of fitting parameters A and B. Inset is the spectral dependence of EQE.

8.2.2 Simulation results and discussion for the analytical model

Using Eq.(8-10) and Eq.(8-12), we plot the fitted photocurrent density of the ITO/MEH-PPV/Al photodetector, as shown in Fig.8-5. It is in very good agreement with

Reproduced with permission of the copyright owner. Further reproduction prohibited without permission.

the measurement data. In summary, the photocurrent generation process can be explained in the following way: After light absorption, the photogenerated excitons diffuse in two opposite directions to the interfaces near the contacts. At the interface the excitons can be efficiently dissociated into charge carriers and quickly be collected by the contacts. While the charge carriers are generated inside the film and finally vanish due to recombination from many factors such as low mobility, disordered structure, oxygen-trapping sites etc. The parameters and values used in the fitting process are listed in Table 8-1.

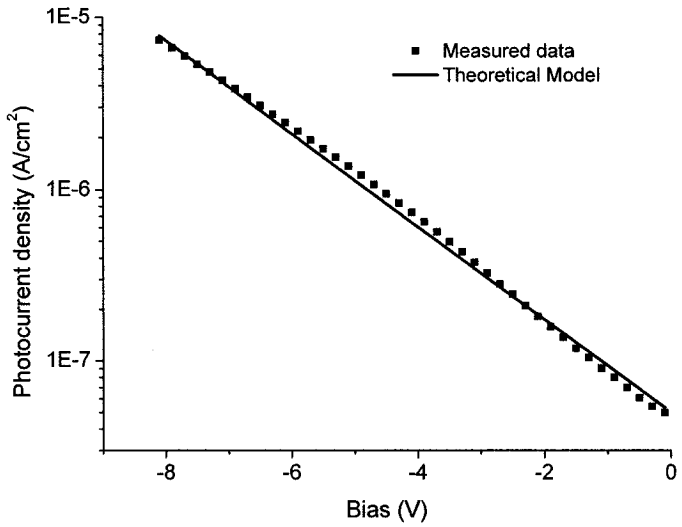

Fig.8-5 The fitting of the photocurrent density of a single-layer intrinsic MEH-PPV photodetector with exciton diffusion model using Eq. (8-10) and Eq. (8-12).

Table 8-1 The parameters and values used in fitting process

Parameter	Symbol	Value	Reference
Diffusion length	L_e	20±3 nm	[40]
Exciton lifetime	τ_e	10^{-9} s	assumed
The wavelength of incident light	λ	520 nm	
MEH-PPV film thickness	d	70 nm	
Light flux	G_0	4.1×10^{14} EHPs/s	
Absorption coefficient	α	137677 cm^{-1}	
Absorption efficiency	η_a	0.85	
Exciton diffusion efficiency	η_{ED}	0.1	assumed
Exciton separation efficiency	η_{ES}	0.12	assumed
Collection efficiency	η_{CC}	0.22	assumed

Reproduced with permission of the copyright owner. Further reproduction prohibited without permission.

8.3 The Simulation with TAURUS

8.3.1 Introduction

We have established an analytical model for the photocurrent density of an ITO/MEH-PPV/Al photodetector. We still need to know the electrical characteristics of the photodetector. We did not establish any analytical model for the current-voltage characteristics of the photodetector. However, we also try to use TAURUS software to simulate the current-voltage characteristics of the device at dark and light.

For simulation of electrical characteristics of inorganic semiconductor devices with TAURUS, three main equations are involved in the simulation process. The symbols and their meanings are listed in Table 8-2.

Poisson's equation

$$\varepsilon\nabla^2\psi = -q(p - n + N_D^{+} - N_A^{-}) - \rho_s \tag{8-13}$$

Continuity equation

$$\frac{\partial n}{\partial t} = \frac{1}{q}\vec{\nabla}\cdot J_n - (U_n - G_n) = F_n(\psi, n, p)$$

$$\frac{\partial p}{\partial t} = \frac{1}{q}\vec{\nabla}\cdot J_p - (U_p - G_p) = F_p(\psi, n, p) \tag{8-14}$$

Boltzman transport theory

$$\vec{J}_n = q\mu_n n\vec{E}_n + qD_n\vec{\nabla}\cdot n$$
$$\vec{J}_p = q\mu_p p\vec{E}_p - qD_p\vec{\nabla}\cdot p \tag{8-15}$$

The mobility in conjugated polymer is not constant. The charge carrier mobility in polymers is commonly considered as field dependent, in Poole-Frenkel-like form described in [115]. This field dependence is the special case of the mobility field

Reproduced with permission of the copyright owner. Further reproduction prohibited without permission.

dependence of $E^{n/n+1}$ at n=1 resulting from the potential energy with r^{-n} dependence [123], where r is radial distance from the charged site.

$$\mu(E) = \mu_0 \exp(\sqrt{\frac{E}{E_0}}) \tag{8-16}$$

where μ_0 is zero-field hole mobility in cm^2/Vs, E is electron field in V/cm, and E_0 is the field dependence constant. In a polymeric material, the hole mobility is much higher than electron mobility. For MEH-PPV, $\mu_p = 0.01\mu_n$ [115].

Table 8-2 The meaning of symbols listed in Poisson's equation, Boltzman transport theory, and continuity equation.

Parameter	Symbol	Unit
Permittivity	ε	
Electric potential	ψ	V
Electron charge	q	C
Acceptor concentration	p	number/cm^3
Donor concentration	n	number/cm^3
Donor doping	N_D^+	number/cm^3
Acceptor doping	N_A^-	number/cm^3
Charge density	ρ_s	C/cm^3
Divergence operator	$\vec{\nabla}\cdot$	
Current density of electron	J_n	A/cm^2
Current density of hole	J_p	A/cm^2
HoleElectron recombination rate	U_p	number/cm^3/s
Electron recombination rate	U_n	number/cm^3/s
Hole generation rate	G_p	number/cm^3/s
Hole generation rate	G_n	number/cm^3/s
Hole mobility	μ_p	cm^2/V-s
Electron mobility	μ_n	cm^2/V-s
Electric field for hole	E_p	V
Electric field for electron	E_n	V

Because the carrier mobility in polymeric polymers is different from the mobility models provided by TAURUS, we need to establish new mobility model in TAURUS. The formula for our mobility model is described in Eq. (8-16). The TAURUS simulation

Reproduced with permission of the copyright owner. Further reproduction prohibited without permission.

codes are given in Appendix C. The drift current is proportional to charge carrier mobility.

8.3.2 Simulation results and discussion

The simulation of the dark I-V curve is based on the 2D structure as shown in Fig.8-6. The energy level diagram of the pure MEH-PPV photodetector is plotted in Fig.8-7. In the simulation, we found that there are several significant parameters that greatly affect the current-voltage curve simulation: density of states of the conduction band and valance band N_C and N_V, zero field mobility μ_0, field-dependence factor E_0, work function of the metal contact (Al), and electron affinity (χ) or intrinsic Fermi level of MEH-PPV.

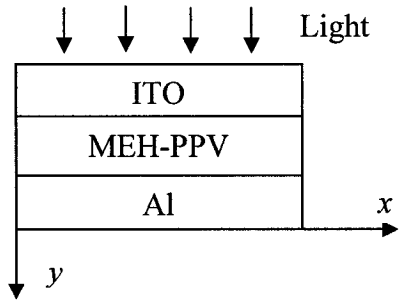

Fig.8-6 The device 2D structure

N_C and N_V affect the intrinsic concentration of polymers by $n_i = \sqrt{N_C N_V}\exp(-\frac{E_g}{2kT})$. In Ref. [117]-[119] values for N_C and N_V for MEH-PPV were reported to be somewhere between 10^{19} and 10^{21} cm^{-3}. However, from our simulation results, the conduction band density of state N_C and valence band density of state N_V are very high, around 5×10^{26} cm^{-3}. This value was obtained when the simulated dark I-V curve is in good agreement with the measured dark I-V curve. For a typical inorganic semiconductor like silicon, N_C and N_V is in the order of 10^{19} cm^{-3}, and its

Reproduced with permission of the copyright owner. Further reproduction prohibited without permission.

intrinsic concentration n_i is in the order of 10^{10} cm^{-3} at 300° K. For MEH-PPV, the intrinsic concentration n_i is about 1.4×10^{9} cm^{-3} for E_g=2.1 eV. Our devices were fabricated and tested in the air and so the intrinsic concentration may be higher due to the presence of impurities. The magnitude of the intrinsic concentration affects the current density at zero bias. Its effect on the dark I-V curve can be observed in Fig.8-8.

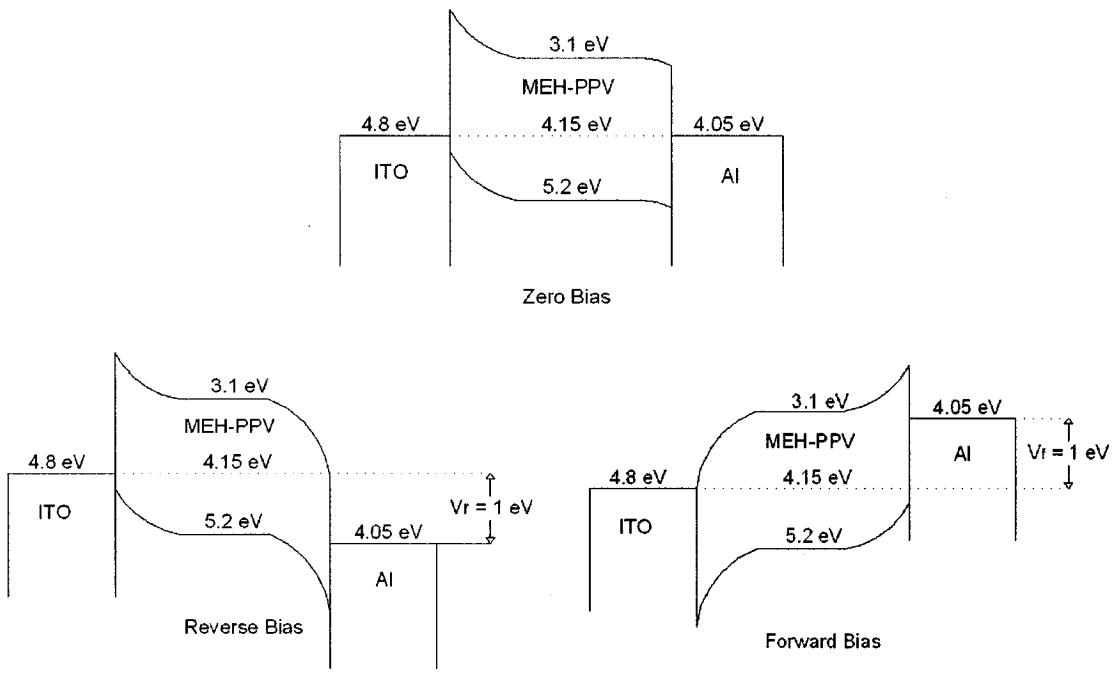

Fig.8-7 The energy level diagram of a polymer photodetector sandwiched between ITO and Al.

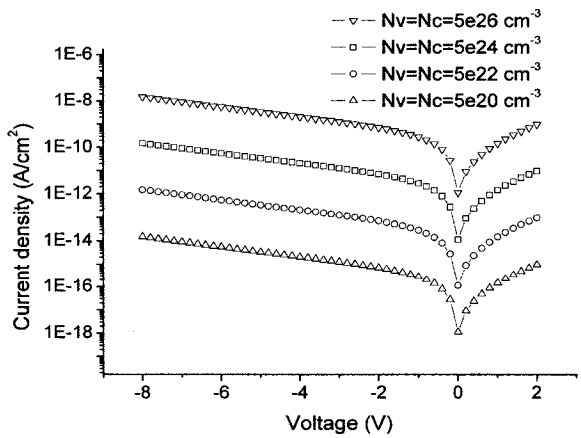

Fig.8-8 The effect of N_C and N_V of MEH-PPV on dark I-V curve of a pure MEHPPV photodetector for the case of W_f=4.05eV, μ_0=$1.8\times10^{-4}$$cm^2$/V-s, E_0=2×10^{9} V/cm, χ=3.1eV.

Reproduced with permission of the copyright owner. Further reproduction prohibited without permission.

Zero-field mobility of polymeric material is lower than the mobility of inorganic semiconductor materials. For example, the zero-field electron and hole mobility for silicon is 1350 and 480 $cm^2/V\text{-}s$, respectively. The mobility of MEH-PPV was reported in the range of 1.3×10^{-4} to 10^{-7} $cm^2/V\text{-}s$ [91][119]. Our simulated I-V curve indicates higher zero-field mobility as like N_C and N_V. It directly affects the current density at zero bias. Its effect on the dark I-V curve is shown in Fig.8-9.

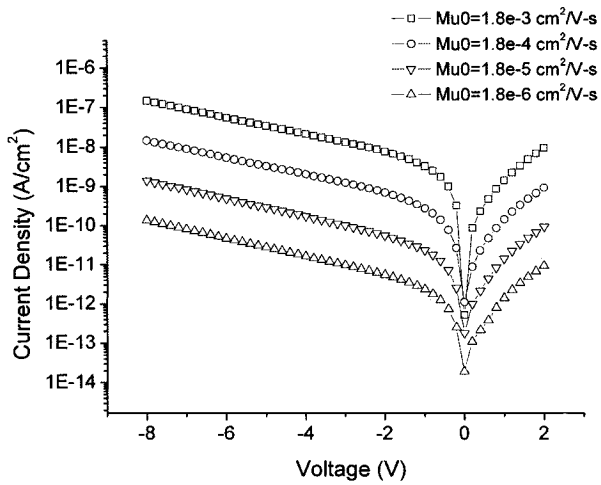

Fig.8-9 The effect of zero-field mobility μ_0 on the dark I-V curve of a pure MEH-PPV photodetector for the case of W_f =4.05 eV, E_0=21.8×10^9 V/cm, N_V =N_C =5×10^{26} /cm^3 χ=3.1 eV.

Zero-field factor, E_0, determines the slope of the current density curve in the semi-log coordinate system, as shown in Fig.8-10. The higher E_0, the less steeper the slope. So the smaller value suggests lower field dependence. In our simulation the value of E_0 is pretty high, ~2×10^9 V/cm, higher than the 4.8×10^4 V/cm reported by [91]. It may be attributed to exposure to the air and degradation of the device.

Reproduced with permission of the copyright owner. Further reproduction prohibited without permission.

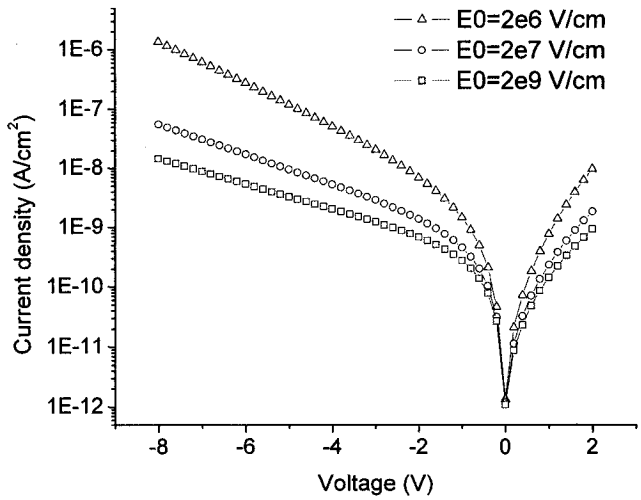

Fig.8-10 The effect of field-dependence factor E_0 on the dark I-V curve of a pure MEHPPV photodetector for the case of W_f =4.05 eV, N_V =N_C =5×10^{26} /cm^3, χ=3.1 eV, μ_0=1.8×10^{-4} cm^2/V-s.

The ITO/MEH-PPV/Al photodetector is a Schottky diode. The band diagram of the device at zero bias, reverse bias and forward bias is depicted in Fig.8-7. The MEHPPV/Al and MEHPPV/ITO interface forms a Schottky barrier. At reverse bias, electrons are injected to LUMO level (~electron affinity) of MEH-PPV from the ITO contact and holes are injected to HOMO level (~ ionization potential). Because the hole mobility of MEH-PPV is two orders higher than electron mobility, the hole drift current should be much higher than electron drift current. The change of barrier height between MEH-PPV and Al has a more obvious effect on the I-V curve. The I-V curve greatly changes with the work function of Al and electron affinity, as shown in Fig.8-11 and Fig.8-12.

Reproduced with permission of the copyright owner. Further reproduction prohibited without permission.

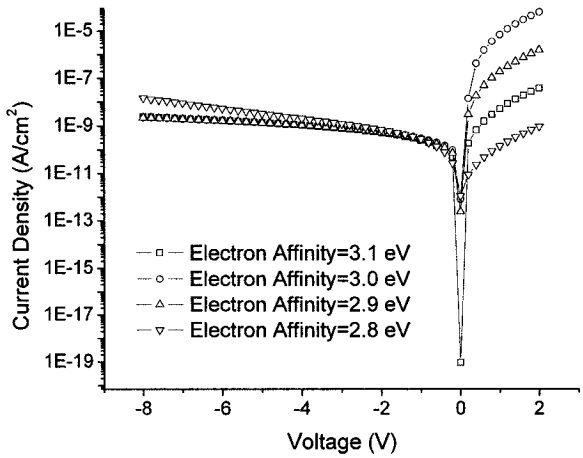

Fig.8-11 The effect of electron affinity χ of MEH-PPV on the dark I-V curve for the case of W_f=4.05, E_0=21.8×10^9 V/cm, N_V=N_C=5×10^{26} /cm^3, μ_0=1.8×10^{-4} cm^2/V-s.

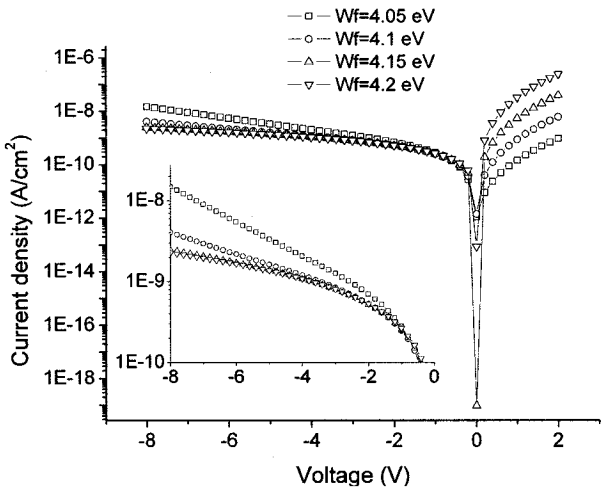

Fig.8-12 The effect of work function W_f of Al contact and electron affinity of MEH-PPV on dark I-V curve.

For TAURUS simulation, there is one important concept different from the exciton diffusion model discussed in Section 8.2. In Section 8.2, the photogenerated exciton in a pure MEH-PPV device will diffuse to the interfaces, only at which the exictons can be efficiently split into charge carrier and quickly collected by the contact. The excitons dissociated in the bulk finally recombine due to low mobility. For the mechanism of TAURUS simulation, the built-in photogeneration function, as shown in

Reproduced with permission of the copyright owner. Further reproduction prohibited without permission.

Eq.(8-14) will directly convert exciton to free electron and hole. These charge carriers participate in the diffusion and drift process. Therefore, the hole and electron concentration can locally change due to photogenerated excess charges. We use the photogeneration function and two carrier solver to simulate the light I-V curve. But the simulated light I-V is much different from the measured light I-V curve. This indicates that photogeneration mechanism in inorganic semiconductor photodetector is different from that of the polymer photodetector. As mentioned in Section 2.3, the exciton binding energy of the inorganic semiconductor is only several kTs, and the exciton binding energy for polymer is from 0.3 eV to 1 eV. The exciton in polymer can only be dissociated at the interfaces. Therefore, the most mobile species inside the polymer film are exciton, but not free charge carriers like hole and electron. The exciton moves by means of a diffusion process. Thus, we need a continuity equation for exciton. We use the electron continuity equation or hole continuity equation, shown in Eq.(8-14), to replace the exciton continuity equation. The parameters used in Eq.(8-14) and Eq.(8-15) are replaced by exciton parameters, like lifetime and mobility (related to diffusion length) given in Table 8-3. The mobility given for light I-V simulation is not for electron or hole mobility. This mobility is used to obtain exciton diffusion length with the Einstein equation. Therefore, the mobility model for the simulation of light I-V curve is the constant mobility model. The problem is, that we can get the exciton concentration with either hole or electron continuity equation, but in TAURUS this concentration is only assigned for hole or electron, but not for the third particles. The solved concentration will change the local potential according to Poisson's equation given in Eq.(8-13), and correspondingly change current density according to Eq.(8-15). Therefore, we believe

Reproduced with permission of the copyright owner. Further reproduction prohibited without permission.

that there is a certain deviation of the simulated I-V curve from the measured I-V curve. The quantization of the deviation is still not well understood. The dark I-V and light I-V curves simulation with TAURUS are plotted in Fig.8-13. There still exists some problems at lower electric fields. We believe that the measured current at lower electric field cannot truly reflect the device characteristics due to the hysteresis effect reported in Chapter 3. The important parameters and values used in the simulation are listed in Table 8-3.

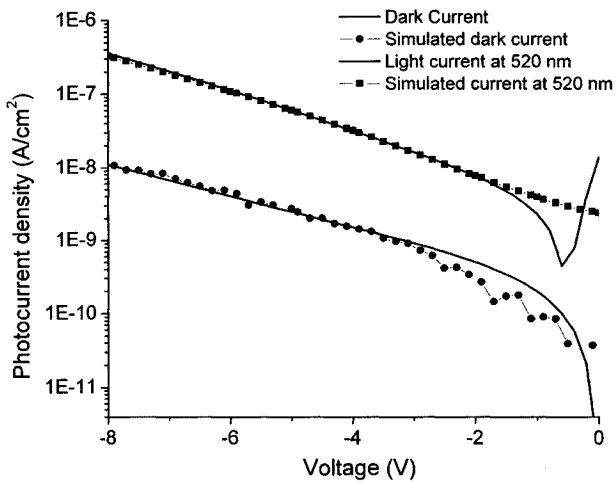

Fig.8-13 The comparison between the simulated and measured dark and light I-V curve of a pure MEH-PPV photodetector with TAURUS.

Table 8-3 The parameters and values used in TAURUS simulation of dark and light I-V curves of a pure MEH-PPV photodetector

Meaning	Symbol	value	unit
Dark I-V simulation			
Valence band density of states	N_V	5×10^{26}	cm^{-3}
Conduction band density of states	N_C	5×10^{26}	cm^{-3}
Zero-field mobility	μ_0	1.8×10^{-4}	$cm^2/V\text{-}s$
Field-dependence factor	E_0	21.8×10^{9}	V/cm
Work function of Al	W_f	4.05	eV
Electron affinity of MEH-PPV	χ	3.1	eV
Light I-V simulation			
Lifetime		10^{-9}	s
Mobility		0.005	$cm^2/V\text{-}s$
Recombination rate	As silicon		

Reproduced with permission of the copyright owner. Further reproduction prohibited without permission.

8.4 Conclusion

In this chapter we modeled the photocurrent action with an ITO/MEH-PPV/Al photodetector using an analytical model. The model uses the detailed diffusion process of exciton and is derived for photocurrent density for a polymer based ITO/MEHPPV/Al diode. The fit of the results from using this model was in a very good agreement with the measured photodetector photocurrent for reverse bias.

We also simulate the dark and light I-V curve based on the TAURUS simulation package, with our built-in Poole-Frenkel mobility model for the polymer diode into the PMEI module in TAURUS. For the photogeneration function we realized the exciton diffusion process by only using the electron continuity equation. All parameters for excitons were set in Physics_data of TAURUS. The simulation of dark and light current-voltage characteristics of a single-layer intrinsic MEH-PPV photodetector matched the measurement data at higher electric fields > 2×10^5 V/cm.

Reproduced with permission of the copyright owner. Further reproduction prohibited without permission.

CHAPTER 9

CONCLUSIONS AND FUTURE WORK

In this thesis, we investigate photodetecting and electronic properties of several kinds of blended polymer photodetectors based on MEH-PPV; aiming to increase the external quantum efficiency of the photodetectors. The EQE for MEH-PPV/EVD devices with 6%w of EVD is doubled compared to the pure MEH-PPV device due to improved electron charge transfer. However, the aggregation of EVD limits the maximum allowble concentration of the EVD in the working device. For MEH-PPV/PbSe devices, quantum efficiencies greater than 1 (i.e. gain) are observed only in devices with the PbSe QDs in the size of 8 nm. The degradation measurement of these devices showed that the expected lifetime of MEH-PPV/PbSe QD photodetectors is from 19-23 days without encapsulation.

MEH-PPV/PCBM devices, with good interpenetration of the MEH-PPV and PCBM, demonstrated the presence of an enhanced carrier-transfer path, and a significant improvement in the quantum efficiency was observed. In addition, nano-patterning of polymer thin films has been realized through the fabrication of MEH-PPV/PCBM integrated with a diffraction grating structure. Examination of the IV characteristics and EQE curves of polymer photodetectors with/without a diffraction grating showed that there was not any observable photoconductivity enhancement.

Reproduced with permission of the copyright owner. Further reproduction prohibited without permission.

We also investigate the detailed diffusion process of excitons and derived an analytical model with the steady-state exciton continuity equation. This model is based on the theory that mobile excitons can only dissociate in the interfaces with enough energy offset. A field dependence factor was used for photocurrent density for ITO/MEH-PPV/Al photodetectors. The results from the measured photodetector photocurrent for reverse bias were in good agreement with the analytical photodetector model. The second technique was using the TAURUS simulation package for inorganic materials to simulate dark and light I-V curves. We built a Poole-Frenkel mobility model for a polymer photodetector with PMEI provided by TAURUS. The simulation of dark current-voltage characteristics of a single-layer intrinsic MEH-PPV photodetector matched the measurement data at higher electric fields ($>2\times10^5$ V/cm) and has shown some deviation for lower electrical fields, probably due to a hysteresis effect.

In the future, several improvements can be made:

1) Optimization of the D-A concentration.

2) Simulation of D-A device with TAURUS, theoretical modeling, and complete simulation of dark and light current-voltage characteristics at lower electric fields ($<2\times10^5$ V/cm).

3) Better control of the morphology of dispersed heterojunction or phase separation like the usage of a porous template, such as a polystyrene sphere

4) Self-assembly or LBL of monlayers in order to modify substrate surfaces and control the segregation of blend components.

5) Improvement of photodetector stability by encapsulation.

Reproduced with permission of the copyright owner. Further reproduction prohibited without permission.

6) Improvement of the theoretical model for lossy grating structure and further enhancement of replication efficiency of the grating pattern.

Reproduced with permission of the copyright owner. Further reproduction prohibited without permission.

APPENDIX A

THE GENERAL FORMULATION FOR TE AND TM MODES

Reproduced with permission of the copyright owner. Further reproduction prohibited without permission.

In order to better understand the formulations used in the numerical simulation of Chapter 7. We abstracted the deduction of general formulation for TE and TM mode from Ref. [147].

The general three-dimensional binary grating diffraction problem is depicted in Fig.A-1. Linearly polarized electromagnetic wave is obliquely incident at an arbitrary angle of incidence θ and at an azimuthal angle Φ upon a binary dielectric or lossy grating. The grating period is, in general, composed of several regions with differing refractive indices. The grating is bound by two different media with refractive indices n_I and n_{II}. In the formulation presented in Appendix A, without any loss of generality, the normal to the boundary is in the z direction, and the grating vector is in the x direction. In the grating region ($0<z<d$) the periodic relative permittivity is expandable in a Fourier series of the form

$$\varepsilon(x) = \sum_h \varepsilon_h \exp(j\frac{2\pi h}{\Lambda}) \qquad \text{(A.1)}$$

where ε_h is the h^{th} Fourier component of the relative permittivity in the grating region, which is complex for lossy or nonsymmetric dielectric gratings.

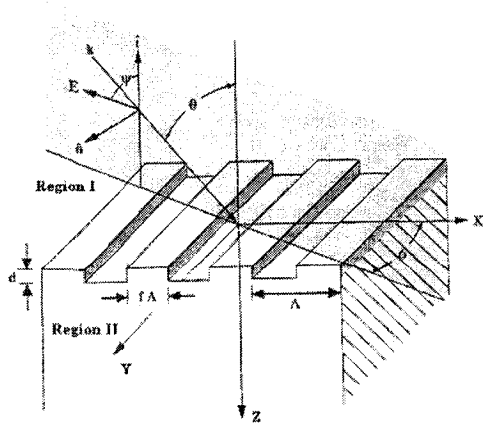

Fig. A-1 The geometry for the binary rectangular-groove grating diffraction (Ref.[147]).

Reproduced with permission of the copyright owner. Further reproduction prohibited without permission.

For simple grating structures with alternating regions of refractive indices n_{rd} (ridge) and n_{gr} (groove) the Fourier harmonics are given by

$$\varepsilon_0 = n_{rd}^{\ 2} f + n_{gr}^{\ 2}(1-f) \qquad \varepsilon_h = (n_{rd}^{\ 2} - n_{gr}^{\ 2})\frac{\sin(\pi h f)}{\pi h} \tag{A.2}$$

Where, f is the fraction of the grating period occupied by the region of index n_{rd} and ε_0 is the average value of the relative permittivity, not the permittivity of free space. The general approach for solving the exact electromagnetic-boundary-value problem associated with the diffraction grating is to find solutions that satisfy Maxwell's equations in each of the three (input, grating, and output) regions and then match the tangential electric and magnetic-field components at the two boundaries. For the case of planar diffraction (Φ=0) the incident polarization may be decomposed into a TE and TM polarization problem, which are handled independently.

Section A.1: The TE polarization

The incident normalized electric field that is normal to the plane of incidence is given by

$$E_{inc,y} = \exp[-jk_0 n_I(\sin\theta x + \cos\theta z)] \tag{A.3}$$

where $k_0 = 2\pi/\lambda_0$ and λ is the wavelength of the light in free space. The normalized solutions in region I ($0<z$) and in region II ($z>d$) are given by

$$E_{I,y} = E_{inc,y} + \sum_i R_i \exp[-j(k_{xi}x - k_{I,zi}z)] \tag{A.4}$$

$$E_{II,y} = \sum_i T_i \exp\{-j[k_{xi}x - k_{II,zi}(z-d)]\} \tag{A.5}$$

where k_{xi} is determined from the Floquet condition and is given by

$$k_{xi} = k_0[n_I \sin\theta - i(\lambda_0/\Lambda)] \tag{A.6}$$

Reproduced with permission of the copyright owner. Further reproduction prohibited without permission.

and where

$$k_{l,zi} = \begin{cases} +k_0[n_l{}^2 - (k_{xi}/k_0)^2]^{1/2} & k_0 n_l > k_{xi} \\ -jk_0[(k_{xi}/k_0)^2 - n_l{}^2]^{1/2} & k_{xi} > k_0 n_l \end{cases} \quad \textit{l=I, II} \qquad \text{(A.7)}$$

R_i is the normalized electric filed amplitude of the ith backward-diffracted (reflected) wave in region *I*. T_i is the normalized electric-field amplitude of the forward-diffracted (transmitted) wave in regions *II*. The magnetic fields in regions *I* and *II* may be obtained from Maxwell's equation

$$H = (\frac{j}{\omega\mu})\nabla \times E \qquad \text{(A.8)}$$

where u is the permeability of the region and ω is the angular optical frequency.

In the grating region ($0 < z < d$) the tangential electric (y-component) and magnetic (x-component) fields may be expressed with a Fourier expansion in terms of the space-harmonic fields as:

$$E_{gy} = \sum S_{yi}(z)\exp(-jk_{xi}x) \qquad \text{(A.9)}$$

$$H_{gx} = -j(\frac{\varepsilon_0}{\mu_0})^{1/2}\sum_i U_{xi}(z)\exp(-jk_{xi}x) \qquad \text{(A.10)}$$

where ε_0 is the permittivity of free space. $S_{yi}(z)$ and $U_{xi}(z)$ are the normalized amplitudes of the ith space harmonic fields such as that E_{gy} and H_{gz} satisfy Maxwell's equation in the grating region, i.e.

$$\frac{\partial E_{gy}}{\partial z} = j\omega\mu_0 H_{gx} \qquad \text{(A.11)}$$

$$\frac{\partial H_{gx}}{\partial z} = j\omega\varepsilon_0\varepsilon(x)E_{gy} + \frac{\partial H_{gz}}{\partial x} \qquad \text{(A.12)}$$

Reproduced with permission of the copyright owner. Further reproduction prohibited without permission.

Substituting Eq.(A.9) and (A.10) and into Eq. (A.11) and (A.12) and eliminating H_{gz}, we obtain the coupled-wave equations

$$\frac{\partial S_{yi}}{\partial z} = k_0 U_{xi}$$

$$\frac{\partial U_{xi}}{\partial z} = (\frac{k_{xi}^{\ 2}}{k_0}) S_{yi} - k_0 \sum_p \varepsilon_{(i-p)} S_{yp} \tag{A.13}$$

or, in matrix form

$$\begin{bmatrix} \partial S_y / \partial(z') \\ \partial U_x / \partial(z') \end{bmatrix} = \begin{bmatrix} 0 & I \\ A & 0 \end{bmatrix} \begin{bmatrix} S_y \\ U_x \end{bmatrix} \tag{A.14}$$

which may be reduced to

$$\left[\partial^2 S_y / \partial(z')^2\right] = [A][S_y] \tag{A.15}$$

where $z' = k_0 z$ and

$$A = K_x^{\ 2} - E \tag{A.16}$$

where E is the matrix formed by the permittivity harmonic components, with the i,p element being equal to $\varepsilon_{(i-p)}$; $\boldsymbol{K_x}$ is diagonal matrix, with the i, i element being equal to k_{xi} / k_0 and $\boldsymbol{I}$ is the identity matrix. Note that $\boldsymbol{A}$, $\boldsymbol{K_x}$ and $\boldsymbol{E}$ are (n×n) matrices, where n is the number of space harmonics retained in the field expansion, with the ith row of the matrix corresponding to the ith space harmonic. The (2n×2n) matrix in Eq.(A.14) thus becomes an (n×n) matrix in Eq.(A.15).

We solve the set of coupled-wave equations by calculating the eigenvalues and the eigenvectors associated with the matrix $\boldsymbol{A}$ (The eigenvalues and eigenvectors can be solved with some softwares, such as Matlab and Mathmatics). The simplification step taken from Eq. (A.14) to Eq.(A.15) effectively reduces the overall computational time of

Reproduced with permission of the copyright owner. Further reproduction prohibited without permission.

the eignevalue problem by a factor of 8. The space harmonics of the tangential electric and magnetic fields in the grating region are then given by

$$S_{yi}(z) = \sum_{m=1}^{n} w_{i,m}\{c_m^{+} \exp(-k_0 q_m z) + c_m^{-} \exp[k_0 q_m (z-d)]\} \tag{A.17}$$

$$U_{xi}(z) = \sum_{m=1}^{n} v_{i,m}\{-c_m^{+} \exp(-k_0 q_m z) + c_m^{-} \exp[k_0 q_m (z-d)]\} \tag{A.18}$$

where $w_{i,m}$ and q_m are the elements of the eigenvector matrix $\boldsymbol{W}$ and the positive square root of the eigenvalues of the matrix $\boldsymbol{A}$, respectively. The quantity $v_{i,m}=q_m w_{i,m}$ is i, m element of the matrix $\boldsymbol{V}=\boldsymbol{WQ}$, where $\boldsymbol{Q}$ is a diagonal matrix with the elements q_m. The quantities c_m^{+} and c_m^{+} are unknown constants to be determined from the boundary conditions. Note that the exponential terms involving the positive square root of the eigenvalues are normalized to prevent possible numerical overflow, as is shown below.

We calculate the amplitudes of the diffracted fields R_i and T_i (together with c_m^{+} and c_m^{+}) by matching the tangential electric and magnetic filed components at the two boundaries. At the boundary ($z = 0$)

$$\delta_{i0} + R_i = \sum_{m=1}^{n} w_{i,m}[c_m^{+} + c_m^{-} \exp(-k_0 q_m d)] \tag{A.19}$$

$$j[n_I \cos\theta\delta_{i0} - (k_{I,zi}/k_0)R_i] = \sum_{i=1}^{n} v_{i,m}[c_m^{+} - c_m^{-} \exp(-k_0 q_m d)] \tag{A.20}$$

or, in matrix form,

$$\begin{bmatrix} \delta_{i0} \\ jn_I \cos\theta\delta_{i0} \end{bmatrix} + \begin{bmatrix} I \\ -jY_I \end{bmatrix}[R] = \begin{bmatrix} W & WX \\ V & -VX \end{bmatrix}\begin{bmatrix} c^{+} \\ c^{-} \end{bmatrix} \tag{A.21}$$

and at boundary $z = d$

$$\sum_{i=1}^{n} w_{i,m}[c_m^{+} \exp(-k_0 q_m d) + c_m^{-}] = T_i \tag{A.22}$$

Reproduced with permission of the copyright owner. Further reproduction prohibited without permission.

$$\sum_{i=1}^{n} v_{i,m}[c_m^{+}\exp(-k_0 q_m d) - c_m^{-}] = j(k_{II,zi}/k_0)T_i \tag{A.23}$$

or in matrix form,

$$\begin{bmatrix} WX & W \\ VX & -V \end{bmatrix}\begin{bmatrix} c^{+} \\ c^{-} \end{bmatrix} = \begin{bmatrix} I \\ jY_{II} \end{bmatrix}[T] \tag{A.24}$$

where δ_{i0}=1 for i=0 and δ_{i0}=0 for $i\neq 0$ and $\boldsymbol{X}$, $\boldsymbol{Y_I}$, and $\boldsymbol{Y_{II}}$ are diagonal matrices with the diagonal elements $\exp(-k_0 q_m d)$, $(k_{I,zi}/k_0)$, and $(k_{II,zi}/k_0)$, respectively. Eqs. (A.21) and (A.24) and are solved simultaneously for the forward-and the backward-diffracted amplitudes T_i and R_i. The diffraction efficiencies are defined as

$$DE_{ri} = R_i R_i^{*}\,\mathrm{Re}\left(\frac{k_{I,zi}}{k_0 n_I \cos\theta}\right)$$

$$DE_{ti} = T_i T_i^{*}\,\mathrm{Re}\left(\frac{k_{II,zi}}{k_0 n_I \cos\theta}\right) \tag{A.25}$$

The sum of the reflected and transmitted diffraction efficiencies given by Eq. (A.25) must be unity for loss-less gratings. This sum is independent of the number of space harmonics retained in the field expansion, which determines the accuracy of the individual diffracted orders.

Section A.2: TM polarization

The incident normalized magnetic field is normal to the incidence plane and may be written as

$$H_{inc,y} = \exp[-jk_0 n_I(\sin\theta x + \cos\theta z)] \tag{A.26}$$

The normalized solution the region I ($0 < z$) and region II ($z > d$) are given respectively by

$$H_{I,y} = H_{inc,y} + \sum_i R_i \exp[-j(k_{xi}x - k_{I,zi}z)] \tag{A.27}$$

Reproduced with permission of the copyright owner. Further reproduction prohibited without permission.

$$H_{II,y} = \sum_i T_i \exp\{-j[k_{xi}x + k_{II,zi}(z-d)]\} \tag{A.28}$$

where k_{xi}, $k_{I,zi}$, $k_{II,zi}$ and are defined as in Eqs (A.6) and (A.7).

R_i is the normalized magnetic-field amplitude of the ith backward—diffracted (reflected) wave in region *I*. T_i is the normalized magnetic-field amplitude of the forward-diffracted (transmitted) wave in region *II*. The magnetic-field vectors in the two regions can be obtained from Maxwell's equation

$$E = (\frac{-j}{\omega\varepsilon_0 n^2})\nabla \times H \tag{A.29}$$

In the modulated region ($0< z < d$) the tangential magnetic (y-component) and electric (x-component) fields may be expressed as a Fourier expansion:

$$H_{gy} = \sum_i U_{yi}(z)\exp(-jk_{xi}x) \tag{A.30}$$

$$E_{gx} = j(\frac{\mu_0}{\varepsilon_0})^{1/2}\sum_i S_{xi}(z)\exp(-jk_{xi}x) \tag{A.31}$$

where $U_{yi}(z)$ and $S_{xi}(z)$ are the normalized amplitudes of the ith space-harmonic fields such that H_{gy} and E_{gx} satisfy Maxwell's equation in the grating region, i.e.,

$$\frac{\partial H_{gy}}{\partial z} = -j\omega\varepsilon_0\varepsilon(x)E_{gx} \tag{A.32}$$

$$\frac{\partial E_{gx}}{\partial z} = -j\omega\mu_0 H_{gy} + \frac{\partial E_{gx}}{\partial x} \tag{A.33}$$

Substituting Eqs. (A.30) and (A.31) into Eqs. (A.32) and (A.33) and eliminating H_{gz}, we find that the set of coupled-wave equations, in matrix form, is

$$\begin{bmatrix} \partial U_y/\partial(z') \\ \partial S_x/\partial(z') \end{bmatrix} = \begin{bmatrix} 0 & E \\ B & 0 \end{bmatrix}\begin{bmatrix} U_x \\ S_x \end{bmatrix} \tag{A.34}$$

which may be reduced to

Reproduced with permission of the copyright owner. Further reproduction prohibited without permission.

$$\left[\partial^2 U_y / \partial(z')^2\right] = [EB][U_y] \tag{A.35}$$

where

$$B = K_x E^{-1} K_x - I \tag{A.36}$$

with $\boldsymbol{E}$ and $\boldsymbol{K_x}$ being defined as in Eq. (A.16). As in the TE case, the above set of coupled-wave equations is solved by calculation of the eigenvalues and the eigenvectors associated with the $(n \times n)$ matrix $\boldsymbol{EB}$, where n is the number of harmonics retained in the field expansion. The $(2n \times 2n)$ matrix in Eq. (A.34) is reduced to an $(n \times n)$ matrix in Eq.(A.35), thus reducing the overall computational time of the eigenvalue problem by a factor of 8. The space harmonics of the tangential magnetic and electric fields are then given by

$$U_{yi}(z) = \sum_{m=1}^{n} w_{i,m}\{c_m^{+} \exp(-k_0 q_m z) + c_m^{-} \exp(k_0 q_m (z-d)]\} \tag{A.37}$$

$$S_{xi}(z) = \sum_{m=1}^{n} v_{i,m}\{-c_m^{+} \exp(-k_0 q_m z) + c_m^{-} \exp(k_0 q_m (z-d)]\} \tag{A.38}$$

where $w_{i,m}$ and q_m are the elements of the eigenvector matrix $\boldsymbol{W}$ and the positive square root of the eigenvalues of the matrix $\boldsymbol{EB}$, respectively. The quantities $v_{i,m}$ are the elements of the product matrix $V = E^{-1}WQ$, with $\boldsymbol{Q}$ is being a diagonal matrix with the diagonal elements q_m. The quantities c_m^{+} and c_m^{-} are unknown constants to be determined from the boundary conditions. Again, note that the exponential terms involving the positive square root of the eignevalues are normalized so that potential numerical overflow is preempted.

As in the TE-polarization case, one calculates the amplitudes of the diffracted fields R_i and T_i (together with c_m^{-} and $c_m^{+)}$ by matching the tangential field components at

Reproduced with permission of the copyright owner. Further reproduction prohibited without permission.

the two boundaries. In matrix form the set of equations for tangential field matching at the input boundary ($z = 0$) is

$$\delta_{i0} + R_i = \sum_{m=1}^{n} w_{i,m}[c_m^{+} + c_m^{-} \exp(-k_0 q_m d)] \tag{A.39}$$

$$j[(\frac{\cos\theta}{n_I})\delta_{i0} - (\frac{k_{I,zi}}{k_0 n_I^{\,2}})R_i] = \sum_{m=1}^{n} v_{i,m}[c_m^{+} - c_m^{-} \exp(-k_0 q_m d)] \tag{A.40}$$

or, in matrix form,

$$\begin{bmatrix} \delta_{i0} \\ j\delta_{i0}\cos\theta / n_I \end{bmatrix} + \begin{bmatrix} I \\ -jZ_I \end{bmatrix}[R] = \begin{bmatrix} W & WX \\ V & -VX \end{bmatrix}\begin{bmatrix} c^{+} \\ c^{-} \end{bmatrix} \tag{A.41}$$

and at $z = d$

$$\sum_{m=1}^{n} w_{i,m}[c_m^{+} \exp(-k_0 q_m d) + c_m^{-}] = T_i \tag{A.42}$$

$$\sum_{m=1}^{n} v_{i,m}[c_m^{+} \exp(-k_0 q_m d) + c_m^{-}] = j(\frac{k_{II,zi}}{k_0 n_{II}^{\,2}})T_i \tag{A.43}$$

or in matrix form

$$\begin{bmatrix} WX & W \\ VX & -V \end{bmatrix}\begin{bmatrix} c^{+} \\ c^{-} \end{bmatrix} = \begin{bmatrix} I \\ jz_{II} \end{bmatrix}[T] \tag{A.44}$$

where $\boldsymbol{X}$ is as defined previously and $\boldsymbol{Z_I}$ and $\boldsymbol{Z_{II}}$ are diagonal matrices with the diagonal elements $(k_{I,zi}/k_0 n_I^{\,2})$ and $(k_{II,zi}/k_0 n_{II}^{\,2})$, respectively.

Eqs. (A.41) and (A.44) are solved simultaneously for the forward- and the backward-diffracted amplitudes T_i and R_i. The diffraction efficiencies are defined as

$$DE_{ri} = R_i R_i^{*} \mathrm{Re}(\frac{k_{I,zi}}{k_0 n_I \cos\theta})$$

$$DE_{ti} = T_i T_i^{*} \mathrm{Re}(\frac{k_{II,zi}}{n_{II}^{\,2}}) / (\frac{k_0 \cos\theta}{n_I}) \tag{A.45}$$

Reproduced with permission of the copyright owner. Further reproduction prohibited without permission.

APPENDIX B

THE NUMERICAL SIMULATION PROGRAM DEVELOPED WITH MATHCAD

Reproduced with permission of the copyright owner. Further reproduction prohibited without permission.

$\kappa := 1.818$ $n := 0.803$ $\theta := 0$ $\lambda 0 := 520$ $r1 := 0.7, 0.71 .. 1.4$ $nI := 2.04$	$\varepsilon := n^2 - \kappa^2 - i \cdot 2 \cdot n \cdot \kappa$ * $\Lambda(r1) := r1 \cdot \lambda 0$ * $r2 := 0.21$ $nII := 0.72$ $k0 := 2\frac{\pi}{\lambda 0}$ *	$d := r2 \cdot \lambda 0$ * $N := 40$ $nrd := 0.72$ $i := 0, 1 .. N - 1$ $r3 = 0.51$	$r3 := \frac{\left[(1-n)^2 + \kappa^2\right]}{(1+n)^2 + \kappa^2}$ * $\sigma := 10^{-8}$ * $f := 0.5$ $ngr := 2.04$
$\varepsilon 0 := nrd^2 \cdot f + ngr^2 \cdot (1 - f)$ *		$\varepsilon(h) := \left(nrd^2 - ngr^2\right) \frac{\sin(\pi \cdot h \cdot f)}{\pi \cdot h}$ *	

$$kx(i, r1) := k0 \cdot nI \cdot \sin(\theta) - k0\frac{i}{r1}$$

$$\text{Range2Vec}(r1, s, e, i) := \left| \begin{array}{l} \text{count} \leftarrow 0 \\ \text{for } i \in s, s + i .. e \\ \quad \left| \begin{array}{l} v_{\text{count}} \leftarrow \frac{kx(i, r1)}{k0} \\ \text{count} \leftarrow \text{count} + 1 \end{array} \right. \\ v \end{array} \right.$$

$$kz(L, x) := \left| \begin{array}{l} \text{if } L = 1 \\ \quad \left| \begin{array}{l} \left[k0 \cdot \sqrt{nI^2 - \left(\frac{x}{k0}\right)^2}\right] \text{ if } |x| < k0 \cdot nI \\ \left[-i\left[k0 \cdot \sqrt{\left[\left(\frac{x}{k0}\right)^2 - nI^2\right]}\right]\right] \text{ otherwise} \end{array} \right. \\ \text{if } L = 2 \\ \quad \left| \begin{array}{l} \left[k0 \cdot \sqrt{nII^2 - \left(\frac{x}{k0}\right)^2}\right] \text{ if } |x| < k0 \cdot nI \\ \left[-i\left[k0 \cdot \sqrt{\left[\left(\frac{x}{k0}\right)^2 - nII^2\right]}\right]\right] \text{ otherwise} \end{array} \right. \end{array} \right.$$

$$\text{Mat}(low, upp, incr) := \left| \begin{array}{l} r \leftarrow 0 \\ \text{for } i \in (low, low + incr .. upp) \\ \quad \left| \begin{array}{l} c \leftarrow 0 \\ \text{for } j \in (low, low + incr .. upp) \\ \quad \left| \begin{array}{l} M_{r,c} \leftarrow \varepsilon 0 \text{ if } i = j \\ M_{r,c} \leftarrow \varepsilon(i - j) \text{ otherwise} \\ c \leftarrow c + 1 \end{array} \right. \\ r \leftarrow r + 1 \end{array} \right. \\ M \end{array} \right.$$

TE mode

$$E := \text{Mat}(0, N - 1, 1)$$

Reproduced with permission of the copyright owner. Further reproduction prohibited without permission.

$$Kx(r1) := \mathrm{diag}\left(\mathrm{Range2Ved}\left(r1, 0, N-1, 1\right)\right)$$

$$A(r1) := Kx(r1)^2 - E$$

$$Q(r1) := \mathrm{diag}\left(\sqrt{\mathrm{eigenvals}(A(r1))}\right)$$

$$W(r1) := \mathrm{eigenvecs}(A(r1))$$

$$X(r1) := \mathrm{diag}\left(e^{-k0 \cdot d \sqrt{\mathrm{eigenvals}(A(r1))}}\right)$$

$$V(r1) := W(r1) \cdot Q(r1)$$

$$\mathrm{Range3Ved}(r1, s, e, i) := \left| \begin{array}{l} count \leftarrow 0 \\ \text{for } i \in s, s+i \mathinner{..} e \\ \quad \left| \begin{array}{l} v_{count} \leftarrow \dfrac{kz\left(1, kx(i, r1)\right)}{k0} \\ count \leftarrow count + 1 \end{array} \right. \\ v \end{array} \right.$$

$$\mathrm{Range4Ved}(r1, s, e, i) := \left| \begin{array}{l} count \leftarrow 0 \\ \text{for } i \in s, s+i \mathinner{..} e \\ \quad \left| \begin{array}{l} v_{count} \leftarrow \dfrac{kz\left(2, kx(i, r1)\right)}{k0} \\ count \leftarrow count + 1 \end{array} \right. \\ v \end{array} \right.$$

$$YI(r1) := \mathrm{diag}\left(\mathrm{Range3Ved}\left(r1, 0, N-1, 1\right)\right)$$

$$YII(r1) := \mathrm{diag}\left(\mathrm{Range4Ved}\left(r1, 0, N-1, 1\right)\right)$$

$$\delta 0(i) := \left| \begin{array}{ll} 1 & \text{if } i = 0 \\ 0 & \text{otherwise} \end{array} \right.$$

$$\mathrm{Range5Ved}(s, e, i) := \left| \begin{array}{l} count \leftarrow 0 \\ \text{for } i \in s, s+i \mathinner{..} e \\ \quad \left| \begin{array}{l} v_{count} \leftarrow \delta 0(i) \\ count \leftarrow count + 1 \end{array} \right. \\ v \end{array} \right.$$

$$\delta 0 := \mathrm{Range5Ved}\left(0, N-1, 1\right)$$

$$C(r1) := \left(i \cdot YI(r1) \cdot W(r1) + V(r1)\right) + \left(i \cdot YI(r1) \cdot W(r1) \cdot X(r1) - V(r1) \cdot X(r1)\right) \cdot \left(i \cdot YII(r1) \cdot W(r1) + V(r1)\right)^{-1} \cdot \left(V(r1) \cdot X(r1) - i \cdot YII(r1) \cdot W(r1) \cdot X(r1)\right)$$

$$C1(r1) := C(r1)^{-1} \cdot \left(i \cdot YI(r1) \cdot \delta 0 + i \cdot nI \cdot \cos(\theta) \cdot \delta 0\right)$$

Reproduced with permission of the copyright owner. Further reproduction prohibited without permission.

$$C2(r1) := (i \cdot YII(r1) \cdot W(r1) + V(r1))^{-1} \cdot (V(r1) \cdot X(r1) - i \cdot YII(r1) \cdot W(r1) \cdot X(r1)) \cdot C1(r1)$$

$$R(r1) := W(r1) \cdot C1(r1) + W(r1) \cdot X(r1) \cdot C2(r1) - \delta 0$$

$$T(r1) := W(r1) \cdot X(r1) \cdot C1(r1) + W(r1) \cdot C2(r1)$$

$$DEr(r1, i) := \left(\left| R(r1)_i \right| \right)^2 Re\left(\frac{kz(1, kx(i, r1))}{k0 \cdot nI \cdot \cos(\theta)} \right)$$

$$DEt(r1, i) := \left(\left| T(r1)_{i,0} \right| \right)^2 \cdot Re\left(\frac{kz(2, kx(i, r1))}{k0 \cdot nI \cdot \cos(\theta)} \right)$$

TM mode

$$I := identity(N)$$

$$B(r1) := Kx(r1) \cdot E^{-1} \cdot Kx(r1) - I$$

$$QM((r1)) := diag\left(\sqrt{eigenvals(E \cdot B(r1))}\right)$$

$$WM(r1) := eigenvecs(E \cdot B(r1))$$

$$VM(r1) := E^{-1} \cdot WM(r1) \cdot QM(r1)$$

$$Range3MVec(r1, s, e, i) := \left| \begin{array}{l} count \leftarrow 0 \\ \text{for } i \in s, s + i .. e \\ \quad \left| \begin{array}{l} v_{count} \leftarrow \dfrac{kz(1, kx(i, r1))}{k0 \cdot nI^2} \\ count \leftarrow count + 1 \end{array} \right. \\ v \end{array} \right.$$

$$Range4MVec(r1, s, e, i) := \left| \begin{array}{l} count \leftarrow 0 \\ \text{for } i \in s, s + i .. e \\ \quad \left| \begin{array}{l} v_{count} \leftarrow \dfrac{kz(2, kx(i, r1))}{k0 \cdot nII^2} \\ count \leftarrow count + 1 \end{array} \right. \\ v \end{array} \right.$$

$$ZI(r1) := diag(Range3MVec(r1, 0, N - 1, 1))$$

$$ZII(r1) := diag(Range4MVec(r1, 0, N - 1, 1))$$

$$CM(r1) := (i \cdot ZI(r1) \cdot WM(r1) + VM(r1)) + (i \cdot ZI(r1) \cdot WM(r1) \cdot X(r1) - VM(r1) \cdot X(r1)) \cdot (i \cdot ZII(r1) \cdot WM(r1) + VM(r1))^{-1} \cdot (VM(r1) \cdot X(r1) - i \cdot ZII(r1) \cdot WM(r1) \cdot X(r1))$$

Reproduced with permission of the copyright owner. Further reproduction prohibited without permission.

$$CM1(r1) := CM(r1)^{-1} \cdot \left(i \cdot ZI(r1) \cdot \delta 0 + i \cdot \cos(\theta) \frac{\delta 0}{nI} \right)$$

$$CM2(r1) := \left(i \cdot ZII(r1) \cdot WM(r1) + VM(r1) \right)^{-1} \cdot \left(VM(r1) \cdot X(r1) - i \cdot ZII(r1) \cdot WM(r1) \cdot X(r1) \right) \cdot CM1(r1)$$

$$RM(r1) := WM(r1) \cdot CM1(r1) + WM(r1) \cdot X(r1) \cdot CM2(r1) - \delta 0$$

$$TM(r1) := WM(r1) \cdot X(r1) \cdot CM1(r1) + WM(r1) \cdot CM2(r1)$$

$$DEMr(r1, i) := \left(\left| RM(r1)_i \right| \right)^2 Re\left(\frac{kz(1, kx(i, r1))}{k0 \cdot nI \cdot \cos(\theta)} \right)$$

$$DEMt(r1, i) := \left(\left| TM(r1)_i \right| \right)^2 \frac{Re\left(\frac{kz(2, kx(i, r1))}{nII^2} \right)}{\left(k0 \frac{\cos(\theta)}{nI} \right)}$$

Reproduced with permission of the copyright owner. Further reproduction prohibited without permission.

APPENDIX C

TAURUS SIMULATION CODE

Reproduced with permission of the copyright owner. Further reproduction prohibited without permission.

There are fives files involved in TAURUS simulation. First, the device structure and mesh are defined in file Detector_stru.pdm. Detector_physics.pdm was specially used to define the physical and electrical properties of polymer material and contacts. Detector_simu.pdm and Detector_simu1.pdm were used to obtain current-voltage characteristics at dark and under illumination. The carrier mobility model in polymer material was established in mobility.pdm.

```
################### Detector_stru.pdm ######################
# Structure Generation
Taurus {device}
DefineDevice (
name=Polymer
minX=0.0 maxX=3.000
minY=0.0 maxY=0.27
Region (material=silicon name=MEHPPV)
Region (material=oxide name=sourcereg)
Region (material=aluminum name=drainreg)
x=0 dx=0.100
y=0 dy=0.05
y=0.1 dy=0.01
y=0.17 dy=0.05)
#Device MEH-PPV region
DefineBoundary
(   region="MEHPPV",
   polygon2d( Point (x=0.0 y=0.1) Point (x=3.000  y=0.1)
Point (x=3.000 y=0.17) Point (x=0 y=0.17)
  ))
# define ITO region
DefineBoundary
( region="sourcereg",
   polygon2d(
Point (x=0.0 y=0.0) Point (x=3.000  y=0.0)
Point (x=3.000 y=0.1) Point (x=0 y=0.1)
))
# define aluminum region
DefineBoundary
( region="drainreg",
   polygon2d(
Point (x=0.0 y=0.17) Point (x=3.000  y=0.17)
Point (x=3.000 y=0.27) Point (x=0 y=0.27)
 ))
```

Reproduced with permission of the copyright owner. Further reproduction prohibited without permission.

```
  # refine the mesh structure
  Regrid (
   GridProgram="NonLevelSet",
   minDelta=0.05um, maxDelta=0.05um)
  # Contacts
  DefineContact (name=source
   X (min=0.0  max=3um)   Y (min=0.0   max=0.1um ))
  DefineContact (name=drain
  X (min= 0um max=3um)   Y (min=0.17  max=0.27um ))

  # save mesh structure
  save (meshFile=mesh.tdf)
#########    Detector_physics.pdm        ########################

# set contact type and work function of ITO contact
setAttributes {Contact (name=source,
                        type=schottky,
                        transparent=true
                        workfunction=4.8,
                        barrierlowering=true,
                        alpha=0,
                        vsurfn=1e7, vsurfp=1e7){Polymer(region=sourcereg)}}


# set contact type and work function of Aluminum contact
setAttributes {Contact (name=source,
                        workfunction=4.1
                        ){Polymer(region=drainreg)}}

#Define the fixed charge in the interfaces
setAttributes{interface(
                        qf=5e10
                        sn=1e7 #recombination velocity of electron)
                        sp=1e7 #
                        material(m0=silicon m1=oxide)
                        addup
                        ){Polymer}}

# define optical properties of ITO
Physics (Oxide (
                OpticsModels(
                        RefractiveIndex
                                (useIndexTable=false
                                nrReal=1.95
                                nrImag=0.01 ))
                Global(Permittivity=4)
```

Reproduced with permission of the copyright owner. Further reproduction prohibited without permission.

```
))){Polymer(region=sourcereg)}

# define optical properties of Aluminium
Physics (Aluminum (
                OpticsModels(
                        RefractiveIndex         (
                                useIndexTable=false
                                nrReal=0.13
                                nrImag=6.08 )
                        Absorption(useconstabsorption=true,
                                constabsorption=2093))
                Global(Permittivity=36)
))){Polymer(region=drainreg)}

# define optical and physical properties of MEH-PPV
Physics (Silicon (
                 Global (
                Density=1.06 #unit g/cm3 #have ignorable effect
                        MolecularWeight=28#unit # at.unit
                        SurfaceDisorder=5e-4 #default value
                        Permittivity=3.61
                electronAffinity=2.9) # [eV]

        # Define the density of states
                Poissons (
                        ValenceDensityofStates
                        ( AtRoomTemperature=2e26)
                        ConductionDensityofStates
                        ( AtRoomTemperature=2e26)
                        Bandgap (Eg300=2.1)
                        ElectronEffectiveMass(me=0.067)   #default 0.067
                        holeEffectiveMass(me=0.4868) #  default 0.4868
                        )
                Electroncontinuity (
                    Recombination (
                        SRHActive=True
                                AugerActive=True
                                srhRecombination (
                                ElectronLifeTime
                                (taun0=1e-5)
                                        HoleLifeTime
                                (taup0=1e-7)))

                        #AugerRecombination(AugN=0E0, AugP=0e0))

        # active the photogeneration function for illumination
```

Reproduced with permission of the copyright owner. Further reproduction prohibited without permission.

```
                PhotogenActive=True)

        OpticsModels(
                RefractiveIndex(useIndexTable=false
                nrReal=1.9
                nrImag=0.01))
                ))){Polymer(region=MEHPPV)}

# activate our mobility model for low and high electric field
Physics(Silicon(
        HoleContinuity(
                Mobility(
                lowFieldMobility (PMEImodel=myholemobility)
                highFieldMobility (PMEIModel=myholemobilityhigh)
        ))))

Physics(Silicon(
        ElectronContinuity(
                Mobility(
                LowFieldMobility(PMEIModel=myelectronmobility)
                highFieldMobility (PMEIModel=myelectronmobilityhigh)
                ))))

Physics(Silicon(mymobility( Mup0=3.2e-4
                        Mun0=3.2e-6
                        myholemobility( Ep0=1)
                        myholemobilityhigh(Ep1=2e9)
                        myelectronmobility( En0=1)
                        myelectronmobilityhigh( En1=2e9)
                )))

##############    Detector_simu.pdm  ###################

Taurus {device}

# define area factor to match real device area
define (width=1680000)

# call mesh file saved in Detector_stru.pdm
DefineDevice (name=Polymer meshFile="mesh.tdf" areafactor=$width)

# call  physics_definition saved in Detector_physics.pdm
include (Detector_physics.pdm)

Symbolic (carriers=0)
Solve {init}
```

Reproduced with permission of the copyright owner. Further reproduction prohibited without permission.

```
Symbolic (carriers=2 Newton)

# set contact bias to be zero

setBias (value=0.0) {Contact(name=drain  type=contactVoltage)}
setBias (value=0.0) {Contact(name=source  type=contactVoltage)}

Solve {}
#Ramp drain
Ramp (logfile=s1.data,
        Voltage (electrode=source, startValue=2,vStep=-0.2,nSteps=50))


###############     Detector_simu1.pdm    ###################

Taurus {device}

define (width=1830000)
DefineDevice (name=Polymer meshFile="mesh.tdf" areafactor=$width)

include (Detector_physics.pdm)

Symbolic (carriers=0)
Solve {init}
#in factor, the diffusion carrier is exciton
Symbolic (carriers=1 Newton electron)
setBias (value=0.0) {Contact(name=drain  type=contactVoltage)}

# define quantum efficiency
define (eff=5.3e-3)

# define EHP generation rate at 520nm
define (genrate=5.64e19)

# define absorption factor
define (absfactor=-0.07)

setBias (value=0) {Contact(name=source,  type=contactVoltage)}

# define effective EHP generation rate
define (newgenrate=expr($genrate*$eff))

# this function can be activated only after activate the flag of PhotogenActive in file
Detector_physics.pdm
photogeneration (xstart=0 ystart=0.1 xend=0 yend=0.17 xmin=0 xmax=3
A3=$newgenrate A4=$absfactor uniform)
```

Reproduced with permission of the copyright owner. Further reproduction prohibited without permission.

```
solve{}

#ramp source voltage
Ramp (logfile=s2.data,
        Voltage (electrode=source, startValue=2,vStep=-0.2,nSteps=50))


############  Poole-Frenkel Field-Dependent Mobility Model  #########

######################  mobility.pdm ##############################

# include the data base for pre-defined variables
EquationDatabase{poissons.db,holecontinuity.db,electroncontinuity.db}

# define equation for mobility model
DefineEquation
(       Name=mymobility,
        Material=Silicon,
        IsDeviceEquation,
        VariableName=Dummy,
        Parameter(Name=Mup0, Default=3.2e-7)
       Parameter(Name=Mun0, Default=3.2e-9)

       Model (name=normfield
         expression{"sqrt(electricfield*electricfield)"})
```

define hole mobility model at low field, the formulation is the same as the followings. But it is flexible to define the field-dependence factor at different electric field.

```
       Model
              (Name=myholemobility,
              parameter(name=Ep0, default=4.8e4)
              expression{"Mup0*exp(sqrt(normfield/Ep0))"}
              )
        Model
              (Name=myholemobilityhigh,
              parameter(name=Ep1, default=4.8e4)
              expression{"Mup0*exp(sqrt(normfield/Ep1))"})

       Model
              (Name=myelectronmobility,
              parameter(name=En0, default=4.8e4)
              expression{"Mun0*exp(sqrt(normfield/En0))"})

       Model
              (Name=myelectronmobilityhigh,
```

Reproduced with permission of the copyright owner. Further reproduction prohibited without permission.

```
                parameter(name=En1, default=4.8e4)
                expression{"Mun0*exp(sqrt(normfield/En1))"})

        Expression{"dummy"}
)
################        End        ############################
```

Reproduced with permission of the copyright owner. Further reproduction prohibited without permission.

BIBLIOGRAPHY

[1] R.G.Smith and S.D.Personick, Receiver Design For Optical Fiber Communication Systems, *Semiconductor Devices For Optical Communication*, New York, Springer-Verlag, ch.4, 1980.

[2] S.R.Forrest, Sensitivity of Avalanche Photodetector Receiver for High Bit-Rate Long Wavelength Optical Communication Systems in Semiconductor and Semimetals, *Lightwave Communications Technology*, v.22D, 1985.

[3] M.Dentan and B.D.Cremoux, Numerical Simulation of The Nonlinear Response of a PIN Photodetector Under High Illumination, *Journal of Lightwave Technology*, v.8, n.8, p.1137-1144, 1990.

[4] M.Kyomasu, Development of An Integrated High Speed Silicon PIN Photodetector Sensor, *IEEE Transaction on Electron Devices*, v.42, n.6, p.1093-1099, 1995.

[5] B.W. Mullins, S.F.Soares, K.A.McArdle, C.M.Wilson, and S.R.J.Brueck, A Simple High-Speed Si Schottky Photodetector, *IEEE Photonics Technology Letters*, v.3, n.4, p.360-362, 1991.

[6] A.G.Dentai, R.Kuchibhotla, J.C.Campbell, C.Tsai, and C.Lei, High Quantum Efficiency, Long Wavelength InP/InGaAs Microcavity, *Electronics Letters*, v.27, n.23, p.2125-2127, 1991.

[7] Y.Liu,S.R.Forrest, J.Hladky, M.J.Lange, G.H.Olsen, and D.E.Ackley, A Planar InP/InGaAs Avalanche Photodetector With Floating Guard Ring And Double Diffused Junction, *Journal of Lightwave Technology*, v.10, n.2, p.182-193, 1992.

[8] R.Farrell, K.Vanderpuye, G.Entine, and M.R.Squillante, High Resolution, Low Energy Avalanche Photodetector X-ray Detectors, *IEEE Transactions on Nuclear Science,* v.38, n.2, p.144-147, 1991.

[9] S.J.Xu, S.J.Chua, T.Mei, X.C.Wang,X.H.Zhang, G.Karunasiri, W.J.Fan, C.H.Wang, J.Jiang, S.Wang, and X.G.Xie, Characteristics Of InGaAs Quantum Dot Infrared Photodectors, *Applied Physics Letters*, v.73, n.21, p.3153-3155, 1998.

[10] H.C.Lu, Quantun Dot Infrared Photodetector, *Opto-Electronics Review*, v.11, n.1 p.1-5, 2003.

Reproduced with permission of the copyright owner. Further reproduction prohibited without permission.

[11] S.D.Gunapala, J.S.Park, G.Sarusi, T.-L. Lin, J.K.Liu, P.D.Maker, R.E.Muller, C.A.Shott, and T.Hoelter, *IEEE Transactions on Electron Devices*, v.44, n.1, p.45-50, 1997.

[12] G.Hanain, B.F.Levine, S.Gunapala, and N.Chand, Large Photoconductive Gain In Quantum Well Infrared Photodetectors, *Applied Physics Letter*, v.57, n.6, p.608-610, 1990.

[13] M.Z,Tidrow, K.K.Choi, C.Y.Lee, W.H.Chang, F.J.Towner, and J.S.Ahearn, Voltage Tunable Three-Color Quantum Well Infrared Photodetector, *Applied Physics Letters,* v.64, n.10, p.1268-1270, 1994.

[14] H.P.Zappe, *Introduction to Semiconductor Integrated Optics*, Artech House, Inc., Norwood, 1995.

[15] S. K. Lower, Simon Fraser University, *Chemical Bonding A Chem1 Reference Text*, [online] http://www.chem1.com/acad/pdf/c1xbond.pdf.

[16] J.H.Burroughes, D.D.C.Bradley, A.R.Brown, R.N.Marks, K.MacKay, R.H.Friend, P.L.Burn, and A.B.Holmes, Light-Emitting Diodes Based On Conjugated Polymers, *Nature*, v.347, n.6293, p.539-541, 1990.

[17] N.S.Sariciftci, L.Smilowitz, A.J.Heeger, and F.Wudl, Photoinduced Electron Transfer From A Conducting Polymer To Buckminsterfullerene, *Science*, v.258, n.5087, p.1474-1476, 1992.

[18] N.S.Sariciftci, D.Braun, C.Zhang, V.I.Srdanov, A.J.Heeger, G.Stucky, and F.Wudl, Semiconducting Polymer-Buckminsterfullerene Heterojunctions: Diodes Photodiodes, and Photovoltaic Cells, *Applied Physics Letters*, v.62, n.6, p.585-587, 1993.

[19] R. J.O.M. Hoofman, M. P. de Haas, L. D.A. Siebbeles, and J.M. Warman, Highly Mobile Electrons And Holes On Isolated Chains Of The Semiconducting Polymer Poly(phenylene vinylene), *Nature*, v.392, n.6671, p.54-56, 1998.

[20] S.A. Carter, J.C. Scott, and P.J. Brock, Enhanced Luminance In Polymer Composite Light Emitting Devices, *Applied Physics Letters*, v.71, n.9, p.145-1147 1997.

[21] I.N.Kang, D.-H. Hwang, H.-K. Shim, T.Zyung, and J.-J. Kim, Highly Improved Quantum Efficiency In Blend Polymer LEDs, *Macromolecules*, v.29, n.1, p.165-169, 1996.

[22] J.J.M. Halls, C.A. Walsh, N.C. Greenham, E.A. Marseglia, R.H. Friend, S.C. Moratti, and A.B. Holmes, Efficient Photodiodes From Interpenetrating Polymer Networks, *Nature*, v.376, n.6540, p.498-500, 1995.

Reproduced with permission of the copyright owner. Further reproduction prohibited without permission.

[23] G. Yu, J.Gao, J.C. Hummelen, F. Wudl, and A.J. Heeger, Polymer Photovoltaic Cells: Enhanced Efficiencies Via A Network Of Internal Donor-Acceptor Heterojunctions, *Science*, v.270, n.5243, p.1789-1791, 1995.

[24] M. Granstrom, K. Petritsch, A.C. Arias, A. Lux, and M.R.Andersson, R.H. Friend, Laminated Fabrication Of Polymeric Photovoltaic Diodes, *Nature*, v.395, n.6699, p.257-260, 1998.

[25] L.Chen, D.W. McBranch, and D.Whitten, Super Quenching Behavior Between A Conjugated Polymer and Molecular Quenchers And Its Application In Biological/Chemical Sensors, *Proceedings of SPIE - The International Society for Optical Engineering*, v.3858, p.32-39, 1999.

[26] F.Hide, B.J.Schwartz, M.A.Díaz-García, and A.J.Heeger, Conjugated Polymers As Solid-State Laser Materials, *Synthetic Metals,* v.91, n.1-3, p.35-40, 1997.

[27] M.D.McGehee and A.J.Heeger, Semiconducting (Conjugated) Polymers As Materials For Solid-State Lasers, *Advanced Materials*, v.12, n.22, p.1655-1668, 2000.

[28] T.R.Hebner, C.C.Wu, D.Marcy, M.H.Lu, and J.C.Sturm, Ink-Jet Printing Of Doped Polymers For Organic Light Emitting Devices, *Applied Physics Letters,* v.72, n.5, p.519-521, 1998.

[29] H.Sirringhaus, T.Kawase, R.H.Friend, T.Shimoda, M.Inbasekaran, W.Wu, and E.P.Woo, High-Resolution Inkjet Printing Of All-Polymer Transistor Circuits, *Science*, v.290, n.5499, p.2123-2126, 2000.

[30] T.Granlun, T.Nyberg, L.S.Roman, M.Svensson, and O.Inganäs, Patterning Of Polymer Light-Emitting Diodes With Soft Lithography, *Advanced Materials*, v.12, n.4, p.269-273, 2000.

[31] J.C.Sturm, H. Gleskova; T.N.Jackson, S.J.Fonash, and S. Wagner, Enabling Technologies For Plastic Displays, *Proceedings of SPIE - The International Society for Optical Engineering*, v.4712, p.222-236, 2002.

[32] Z.Bao, J.A.Rogers, A.Dodabalapur, A.J.Lovinger, H.E.Katz, V.R.Raju, Z.Peng, and M.E.Galvin, Polymer Light Emitting Diodes: New Materials And Devices, *Optical Materials*, v.12, n.2-3, p.177-182, 1999.

[33] J.M.Leng, S.Jeglinski, X.Wei,R.E.Benner, Z.V.Vardeny, F.Guo, and S.Mazumdar, Optical Probes Of Excited States In Poly(p-phenylenevinylene), *Physical Review Letters*, v.72, n.1, p.156, 1994.

[34] M.Yan, L.J.Rothberg, E.W.Kwock, and T.M.Miller, Interchain Excitations In Conjugated Polymers, *Physical Review Letters*, v.75, n.10, p.1992,1995,

Reproduced with permission of the copyright owner. Further reproduction prohibited without permission.

[35] K.Pakbaz, C.H.Lee, A.J.Heeger, T.W.Hagler, and D.McBranch, Nature Of The Primary Photoexcitations In Poly(arylene-vinylenes), *Synthetic Metals*, v.64, n.2-3, p.295, 1994.

[36] R.H.Friend, D.D.C.Bradley, and P.D.Townsend, Photo-Excitation In Conjugated Polymers, *Journal of Physics D: Applied Physics*, v.20, n.11, p.1367, 1987.

[37] R.Kersting, U.Lemmer, M.Deussen, H.J.Bakker, R.F.Marhrt, H.Kurz, V.I. Arkhipov, H.Bässler, and E.O.Göbel, Ultrafast Field-Induced Dissociation Of Excitons In Conjugated Polymers, *Physical Review Letters*, v.73, n.10, p.1440, 1994.

[38] C. Kittel, Introduction To Solid State Physics, 7th edition, John Wiley & Sons, Inc, New York, p.311, 1996.

[39] K. Petritsch, Organic Solar Cell Architecture, Ph.D thesis, Technisch-Naturwissenschaftliche Fakult¨at der Technischen Universit¨at Graz, Austria, 2000.

[40] T.J.Savenije, J.M.Warman, and A.Goossens, Visible Light Sensitisation Of Titanium Dioxide Using A Phenylene Vinylene Polymer, *Chemical Physic Letters*, v.287, n.1, p.148, 1998.

[41] A.J Breeze, Z.Schlesinger, and S.A.Carter, Charge Transfer In TiO_2/MEH-PPV Polymer Photovoltaics, *Physical Review* ***B***, v.64, n.12, p.125205, 2001.

[42] H. B. Michaelson, The Workfunction Of The Elements And Its Periodicity, *Journal of Applied Physics*, v.48, p.4729-4733, 1977.

[43] M.D.Bullwinkel, J.Gu, G.A.Campbell, and P.C.Sukanek, The Effect Of Polymer Molecular Weight And Solvent Type On The Planarization Of Spin-Coated Films, *Journal of Electrochemical Society*, v.142, n.7, p.2389-2394, 1995.

[44] L.L.Spangler, J.M.Torkelson, and J.S.Royal, Influence Of Solvent And Molecular Weight On Thickness And Surface Topography Of Spin-Coated Polymer Films, *Polymer Engineering and Science*, v.30, n.11, p.644-653, 1990.

[45] D.W.Schubert, Spin Coating As A Method For Polymer Molecular Weight Determination, *Polymer Bulletin*, v.38, n.2, p.177-184, 1997.

[46] H.Yanagi and S.Okamoto, Orientation-Controlled Organic Electroluminescence Of p-Sexiphenyl Films, *Applied Physics Letters*, v.71, n.18, p.2563-2565, 1997.

[47] H.Yanagi, T.Morikawa, S. Hotta, and Kiyoshi Yase, Epitaxial Growth Of Thiophene/p-Phenylene co-Oligomers For Highly Polarized Light-Emitting Crystals, *Advanced Materials*, v.13, n.5, p.313, 2001.

Reproduced with permission of the copyright owner. Further reproduction prohibited without permission.

[48] B.Mueller, T.Kuhlmann, K.Lischka, H.Schwer, R.Resel, and G.Leising, MBE Growth Of Para-Hexaphenyl On GaAs(001)-2×4, *Surface Science*, v.418, n.1, p.256, 1998.

[49] S.E.Shaheen, R.Radspinner, N.Peyghambarian, and G.E.Jabbour, Fabrication Of Bulk Heterojunction Plastic Solar Cells By Screen Printing, *Applied Physics Letters*, v.79, n.18, p.2996-2998, 2001.

[50] N. C. Greenham, S. C. Moratti, D. D. C. Bradley, R. H. Friend, and A. B. Holmes, Efficient Light-Emitting Diodes Based On Polymers With High Electron Affinities, *Nature*, v.365, n.6447, p.628-630, 1993.

[51] F. Wudl and G. Srdanov, *U.S. Patent No.* 5189136, 1993.

[52] N. S. Sariciftci and A.J. Heeger, Role Of Buckminsterfullerene C60 In Organic Polymeric Photoelectric Devices, *Proceeding of SPIE - The International Society for Optical Engineering*, v.2530, p.76-86, 1995.

[53] G. R. Hayes, I. D. W. Samuel and R. T. Phillips, Ultrafast Dynamics Of Photoexcitations In Conjugated Polymers, *Synthetic Metals*, v.84, n.1-3, p.889-890, 1997.

[54] K. Petrisch and R. H. Friend, Ultrathin Organic Photovoltaic Devices, *Synthetic Metals*, v.102, n.1-3 pt.2, p.976, 1999.

[55] G. Pfister, Hopping Transport In A Molecularly Doped Organic Polymer, *Physical Review* ***B***, v.16, p.3676, 1977.

[56] F. L. Zhang, M. Johansson, M. R. Andersson, J. C. Hummelen, and O. Inganas, Polymer Solar Cells Based On MEH-PPV and PCBM, *Synthetic Metals*, v.137, n.1-3, p.1401, 2003.

[57] J. Y. Park, S. B. Lee, Y. S. Park, Y. W. Park, C. H. Lee, J. I. Lee, and H. K. Shim, Doping Effect Of Viologen On Photoconductive Device Made Of Poly (p-phenylenevinylene), *Applied Physics Letters*, v.72, n.22, p.2871-2873, 1998.

[58] J. J. Peon, X. Tan, J. D. Hoerner, C. Xia, Y. Luk, and B. Kohler, Excited State Dynamics of Methyl Viologen. Ultrafast Photoreduction In Methanol And Fluorescence In Acetonitrile, *Journal of Physical Chemistry A*, v.105, n.24, p.5768 -5777, 2001.

[59] C. Yang, G. He, R. Wang, and Y. Li, Addition Of Viologen In Luminescent Polymers For Polymer Light-Emitting Diodes, *Thin Solid Film*, v.363, n.1, p.218-220, 2000.

[60] H.S. Majumdar, A.Bolognesi, and A.J. Pal, Memory Applications Of A Thiophene Based Conjugated Polymer: Capacitance Measurements, *Journal of Physics D: Applied Physics,* v.36, n.2, p.211-215, 2003.

Reproduced with permission of the copyright owner. Further reproduction prohibited without permission.

[61] F. Feller, D.Geschke and A.P.Monkman, Spatial Distribution Of Space Charge In Conjugated Polymers, *Applied Physics Letters*, v.79, n.6, p.779, 2001.

[62] A.V. Yakimov, V.N.; Savvate'ev, and D. Davidov, Role Of Traps In Polymer-Based Light-Emitting Devices, *Synthetic Metals*, v.115, n.1, p.51-56, 2000.

[63] H.-E. Tseng, K.-Y. Peng, and S.-A. Chen, Molecular Oxygen And Moisture As Traps In Poly[2-methoxy-5(2 prime -ethylhexyloxy)-1,4-phenylene vinylene]: Locations And Detrapping By Chain Relaxation, *Applied Physics Letters*, v.82, n.23, p.4086-4088, 2003.

[64] P.Stallinga, H. L.Gomes, H. Rost, A.B. Holmes, M.G.Harrison, R.H.Friend, F. Biscarini, C. Taliani, G.W. Jones, and D.M.Taylor, Determination Of Deep And Shallow Levels In Conjugated Polymers By Electrical Methods, *Physica B: Condensed Materials*, v.273-274, p.923- 926, 1999.

[65] S. Chaudhary, M. Ozkan, and W.C.W. Chan, Trilayer Hybrid Polymer-Quantum Dot Light-Emitting Diodes, *Applied Physics Letters*, v.84, n.15, p.2925, 2004.

[66] L.Bakueva, S.Musikhin, M.A.Hines, T.-W.F.Chang, M.Tzolov, G.D.Scholes, and E.H.Sargent, Size-Tunable Infrared (1000-1600 nm) Electroluminescence From PbS Quantum-Dot Nanocrystals In A Semiconducting Polymer, *Applied Physics Letters*, v.82, n.17, p.2895, 2003.

[67] J.Liu, T.Tanaka, K.Sivula, A.P. Alivisatos, and J.M.J.Fréchet, Employing End-Functional Polythiophene To Control The Morphology Of Nanocrystal - Polymer Composites In Hybrid Solar Cells, *Journal of the American Chemical Society*, v.126, n.21, p.6550-6551, 2004.

[68] S. Kumar, and T. Nann, First Solar Cells Based On CdTe Nanoparticle/MEH-PPV Composites, *Journal of Materials Research*, v.19, n.7, p.1990-1994, 2004.

[69] D. J. Suh, O.O.Park, T.Ahn, and H.-K. Shim, Observation Of The Photorefractive Behaviors in The Polymer Nanocomposite Based On MEH-PPV/CdSe Nanoparticle Matrix, *Optical Materials*, v.21, n.1-2, p.365-371, 2002.

[70] S. Coe, W.-K. Woo M. Bawendi, and V. Bulovic, Electroluminescence From Single Monolayers Of Nanocrystals In Molecular Organic Devices, *Nature*, v.420, n.6917, p.800-803, 2002.

[71] T.-W. F. Chang, S.Musikhin, L. Bakueva, L. Levina, M.A. Hines, P.W. Cyr, and E.H.Sargent, Efficient Excitation Transfer From Polymer To Nanocrystals, *Applied Physics Letters*, v.84, n.21, p.4295-4297, 2004.

[72] S. Gorer, A. Albu-Yaron, and G.Hodes, Quantum Size Fffects In Chemically Deposited, Nanocrystalline Lead Selenide Films, *Journal of Physical Chemistry*, v.99, n.44, p.16442, 1995.

Reproduced with permission of the copyright owner. Further reproduction prohibited without permission.

[73] R. D. Schaller and V. I. Klimov, High Efficiency Carrier Multiplication In PbSe Nanocrystals: Implications For Solar Energy Conversion, *Physical Review Letters*, v.92, n.18, p.186601-1-186601-4, 2004.

[74] A.J. Nozik, Spectroscopy and Hot Electron Relaxation Dynamics In Semiconductor Quantum Wells and Quantum Dots, *Annual Review of Physical Chemistry*, v.52, p.193, 2001.

[75] L. Bozano, S.A. Carter, J.C. Scott, G.G. Malliaras, and P.J. Brock, Temperature-And Field-dependent Electron And Hole Mobilities In Polymer Light-Emitting Diodes, *Applied Physical Letters*, v.74, n.8, p.1132, 1999.

[76] T. W. Hagler, K. Pakbaz, and A. J. Heeger, Polarized-Electroabsorption Spectroscopy of a Soluble Derivative of Poly(*p*-phenylenevinylene) Oriented By Gel Processing In Polyethylene: Polarization Anisotropy, The Off-Axis Dipole Moment, And Excited-State Delocalization, *Physical Review* ***B***, v.49, n.16, p.10968-10975, 1994.

[77] T. Zyung and J. Kim, Photodegradation Of Poly(p- phenylenevinylene) By Laser Light At The Peak Wavelength Of Electroluminescence, *Applied Physics Letters*, v.67, n.23, p.3420-3422, 1995.

[78] M. Abdou and S. Holdcroft, Mechanisms Of Photodegradation Of Poly(3-alkylthiophenes) In Solution , *Macromolecules*, v.26, n.11, p.2954-2962, 1993.

[79] R. Khillan. Y. Su, and K. Varahramyan, Degradation of MEH-PPV Due To Oxygen/Moisture Traps Through C-V Analysis And Attenuated Total Reflection IR Spectroscopy, *Materials Research Society Symposium Proceeding*, v.814, p.I11.5.3, 2004.

[80] [online]http://www.newton.dep.anl.gov/newton/askasci/1993/chem/CHEM032.HTM

[81] I. Parker, Y. Cao, and C. Yang, Lifetime And Degradation Effects In Polymer Light-Emitting Diodes, *Journal of Applied Physics*, v.85, p.2441-2447, 1999.

[82] C. J. Brabec, F. Padinger, V. Dyakonov, J. C. Hummelen, R. A. J. Jansen, and N. S. Sarciftci, Realization Of Large Area Flexible Fullerene – Conjugated Polymer Photocells: A Route To Plastic Solar Cells, *Proceeding of the International Winterschool on Electronic Properties of Novel Materials-Progress in Molecular Nanostructures*, World Scientific Publishing, p.519, 1998.

[83] G.R. Hayes, I.D.W. Samuel, and R.T. Phillips, Ultrafast Dynamics Of Photoexcitations In Conjugated Polymers, *Synthetic Metals*, v.84, n.1-2 pt.1, p.889-890, 1997.

[84] Zhengchun Liu, Electrically Switchable Organic Memory Devices, PhD Dissertation, Louisiana Tech University, 2005.

Reproduced with permission of the copyright owner. Further reproduction prohibited without permission.

[85] V.Dyakonov, Mechanisms Controlling The Efficiency Of Polymer Solar Cells, *Applied Physics A: Materials Science and Processing*, v.79, n.1, p.21-25, 2004.

[86] D. Chirvase, Z.Chiguvare, M.Knipper, J.Parisi, V.Dyakonov, and J.C Hummelen, Electrical And Optical Design And Characterization Of Regioregular Poly(3-hexylthiophene-2,5diyl)/Fullerene-Based Heterojunction Polymer Solar Cells, *Synthetic Metals*, v.138, n.1-2, p.299, 2003.

[87] R. J.O.M. Hoofman, M. P. de Haas, L. D.A. Siebbeles, and J.M. Warman, Highly Mobile Electrons And Holes On Isolated Chains Of The Semiconducting Polymer Poly(phenylene vinylene), *Nature*, v.392, n.6671, p.54-56, 1998.

[88] D. McBranch, M. Sinclair, A.Hays, D.Moses, and A.J.Heeger, Picosecond Waveguide Modulation In Conjugated Polymers, *Synthetic Metals*, v.49, n.1-3, p.147, 1992.

[89] G Kranzelbinder and G.Leising, Organic Solid-State Lasers, *Representive Progress Physics,* v.63, n.729-762, 2000.

[90] H. Sirringhaus, P. J. Brown, R. H. Friend, M. M. Nielsen, K. Bechgaard, B. M. W. Langeveld-Voss, A. J. H. Spiering, R. A. J. Janssen, E. W. Meijer, P. Herwig, and D. M. de Leeuw, Two-Dimensional Charge Transport In Self-Organized, High-Mobility Conjugated Polymers, *Nature*, v.401, n.6754, p.685-688, 1999.

[91] B.-R. Yang and H.-N. Lin, Mobility Enhancement Of Electroluminescent Polymer Aggregates And Films Investigated By Conducting Atomic Force Microscopy, [online] http://www.mse.nthu.edu.tw/~hnlin/PDF/TCI-YBR.pdf.

[92] G.G.Malliaras, J.R.Salem, P.J.Brock, and C.Scott, Electrical Characteristics And Efficiency Of Single-Layer Organic Light-Emitting Diodes, *Physical Review* ***B***, v.58, n.20, p,R13411, 1998.

[93] O. J. Korovyanko, R. O¨ sterbacka, X. M. Jiang, and Z. V. Vardeny, and R. A. J. Janssen, Photoexcitation Dynamics In Regioregular And Regiorandom Polythiophene Films, *Physical Review* ***B***, v.64, p.235122, 2001.

[94] M. Tammer and A.P.Monkman, Measurement Of The Anisotropic Refractive Indices Of Spin Cast Thin Poly (2-methoxy-5-(2'-ethyl-hexyloxy)-p-phenylenevinylene) (MEH-PPV) Films, *Advanced Materials*, v.14, n.3, p.210-212, 2002.

[95] G.Leising, Anisotropy Of The Optical Constants Of Pure And Metallic Polyacetylene, *Physical Review* ***B***, v.38, n.15, p.10313-10322, 1988.

[96] D. Comoretto, R.Tubino, G. Dellepiane, G.F. Musso, A.Borghesi, A.Piaggi, and G.Lanzani, Optical Properties Of Highly Oriented Fibrous Polyacetylene, *Physical Review* ***B***, v.41, n.6, p.3534-3537, 1990.

Reproduced with permission of the copyright owner. Further reproduction prohibited without permission.

[97] E.K.Miller, G.S.Maskel, C.Y.Yang, and A.J.Heeger, Polarized Ultraviolet Absorption By An Oriented Derivative Of Poly(para-phenylene), *Physical Review* ***B***, v.60, n.11, p.8028, 1999.

[98] T.W.Hagler, K.Pakbaz, and A.J.Heeger, Polarized-Electroabsorption Spectroscopy Of A Soluble Derivative Of Poly(p-phenylenevinylene (Oriented By Gel Processing In Polyethylene: Polarization Anisotropy, The Off-Axis Dipole Moment, And Excited-State Delocalization, *Physical Review* ***B***, v.49, n.16, p.10968, 1994.

[99] F.Feller and A.P.Monkman, Optical Spectroscopy Of Oriented Films of Poly (2,5-pyridinediyl), *Physical Review* ***B***, v.61, n.20, p.13560-13564, 2000.

[100] T.Danno, J.Kürti, and H.Kuzmany, Optical Anisotropy And Raman Scattering From Highly Oriented Poly(octthiophene) Films, *Physical Review* ***B***, v.43, n.6, p.4809-4819, 1991.

[101] T.H.Cho, J.K.Lee and P.S.Ho, E.T.Ryan, and J.G.Pellerin, Dielectric Anisotropy And Molecular Orientation Of Fluorinated Polymers Confined In Submicron Trenches, *Journal of Vacuum Science Technology* ***B,*** v.18, n.1, p.208, 2000.

[102] D. Comoretto, G.Dellepiane, F.Marabelli, J.Cornil, D.A.dos Santos, J.L.Brédas, and D.Moses, Optical Constants Of Highly Stretch-Oriented Poly(p-phenylene-vinylene): Joint Experimental And Theoretical Study, *Physical Review* ***B***, v.62, n.15, p.10173-10184, 2000.

[103] M. Losurdo, G.Bruno, and E.A.Irene, Anisotropy of Optical Properties of Conjugate Polymer Thin Films by Spectroscopic Ellipsometry, *Journal of Applied Physics*, v.94, n.8, p.4923-4929, 2003.

[104] Harland G. Tompkins, and W.A.McGahan, Spectroscopic Ellipsometry And Reflectometry, Wiley-Interscience Publication, 1999.

[105] C.Kittel, Introduction To Solid State Physics, 7th edition, John Wiley & Sons, Inc., New York, p.311, 1996.

[106] D.McBranch, I.H.Campbell, and D.L.Smith, Optical Determination Of Chain Orientation In Electroluminescent Polymer Films, *Applied Physics Letters*, v.66, n.10, p.1175-1177, 1995.

[107] C.Heine, R.H.Morf, Submicrometer Gratings For Solar Energy Applications, *Applied Optics*, v.34, n.14, p.2476-2482, 1995.

[108] L.S.Roman, O.Inganäs, T.Granlund, T.Nyberg, M.Svensson, M.R.Andersson, and J.C.Hummelen, Trapping Light In Polymer Photodetectors With Soft Embossed Gratings, *Advanced Materials*, v.12, n.3, p.189-195, 2000.

Reproduced with permission of the copyright owner. Further reproduction prohibited without permission.

[109] V.Terrazzoni-Daudrix, J.Guillet, X.Niquille, L.Feitknecht, F.Freitas, P.Winkler, A.Shah, R. Morf, O.Parriaux, and D. Fischer, Enhanced Light Trapping In Thin Film Silicon Solar Cells Deposited On PET And Glass, *Proceedings of the 3rd World Conference on Photovoltaic Energy Conversion*, v.B, p.1596-1600, 2003.

[110] Younan Xia and George M. Whitesides, Soft Lithography, *Annual Review Material Sciences*, v.28, p.153-184, 1998.

[111] M.G.Moharam and T.K.Gaylord, Rigorous Coupled-Wave Analysis Of Metallic Surface-Relief Gratings, *Journal of Optical Society of America A*, v.3, n.11, p.1780-1787, 1986.

[112] M.G.Moharm, E.B.Grann, D.A.Pommet, and T.K.Gaylord, Formulation For Stable And Efficient Implementation Of The Rigorous Coupled-Wave Analysis Of Binary Gratings, *Journal of Optical Society of America A*, v.12, n.5, p.1068-1075, 1995.

[113] [online] www.luxpop.com

[114] H.Hoppe, N.S. Sariciftci, and D. Meissner, Optical Constants Of Conjugated Polymer/Fullerene Based Bulk-Heterojunction Organic Solar Cells,_*Molecular Crystals and Liquid Crystals Science and Technology Section A: Molecular Crystals and Liquid Crystals*, v.385, PART II, *Proceedings of the Fourth International Conference on Electronic Processes in Organic Materials*, p.[233]/113-[239]/119, 2002.

[115] A.J Breeze, Z.Schlesinger, and S.A.Carter, Charge Transfer In TiO_2/MEH-PPV Polymer Photovoltaics, *Physical Review **B***, v.64, n.12, p.125205, 2001.

[116] G.G.Malliaras, J.R.Salem, P.J.Brock, and C.Scott, Electrical Characteristics And Efficiency Of Single-Layer Organic Light-Emitting Diodes, *Physical Review **B***, v.58, n.20, p.R13411, 1998.

[117] Z.G.Yu, D.L.Smith, A.Saxena, R.L.Martin, and A.B.Bishop, Molecular Geometry Fluctuation Model For The Mobility Of Conjugated Polymer, *Physical Review Letters*, v.84, n.4, p.721-724, 2000.

[118] S.J.Martin and A.B.Walker, Electrical Transport Characteristics Of Single Layer Organic Devices From Theory And Experiment, Imperial College, London, United Kindom, [online]http://www.bath.ac.uk/~pysabw/research/organics/tpdpaper.pdf.

[119] L. Bozano, S. A. Cartera, J. C. Scott, G. G. Malliaras, and P. J. Brock, Temperature- And Field-Dependent Electron And Hole Mobilities In Polymer Light-Emitting Diodes, *Applied Physcis Letters*, v.74, n.8, p.10-17, 1999.

[120] J.G.Simmons, Poole-Frenkel Effect And Schottky Effect In Metal-Insulator-Metal Systems, *Physical Review*, v.155, n.3, p.657-660, 1967.

Reproduced with permission of the copyright owner. Further reproduction prohibited without permission.

[121] P.Peumans, A.Yakimov, and S.R.Forrest, Small Molecular Weight Organic Thin-Film Photodetectors And Solar Cells, *Journal of Applied Physics*, v.93, n.7, p.3693-3723, 2003.

[122] O. Inganäs and L.S.Roman, Organic Photodiodes: From diodes To Tlends, *Organic Photovoltaics*, p.249, Springer, 2003.

[123] L.B.Schein, A.Peled, and D.Glatz, The Electric Field Dependence Of The Mobility In Molecularly Doped Polymers, *Journal of Applied Physics*, v.66, n.2, p.686-692, 1989.

Reproduced with permission of the copyright owner. Further reproduction prohibited without permission.

VITA

EDUCATION

Sep 02-present
PH.D.- Engineering
IFM, Louisiana Tech University, Ruston, LA 71270

Sep 98-Apr 01
MS-Optical Engineering
Changchun Institute of Optics, Fine Mechanism and Physics, Chinese Academy of Sciences, Changchun, China 130022

Sep 88-July 92
BS- Mechanical Engineering
Yanshan University, Qinghuangdao, China 066004

PUBLICATIONS

1. Difei Qi, Hongbo Yang, etc, Applying NURBs to realize the reconstruction of aircraft blade data, *Optics and Precision Engineering (China),* v9, n3, p223-225, 2001.
2. Difei Qi, Michael Fischbein, Marija Drndic, and Sandra Selmic, Efficient polymer-nanocrystal quantum dot photodetectors, *Applied Physics Letters*, v86, 093103, Febuary 28, 2005.
3. Difei Qi, Michael Fischbein, Marija Drndic, and Sandra Selmic, Efficient polymer-nanocrystal quantum dot photodetectors, *Virtual Journal of Nanoscale Science & Technology*, v 11, n 9, March 7, 2005.
4. David Keith Chambers, Srikanth Karanam, Difei Qi, Sandra Selmic, Ya.B. Losovyj, Luis G. Rosa and P. A. Dowben, The Electronic Structure of Oriented poly(2-methoxy-5-(2,9-ethyl-hexyloxy)-1,4-phenylenevinylene), *Applied Physics A*, Materials Science & Processing, v 80, p 483-488, 2005.
5. Difei Qi, Kody Varahramyan, and Sandra Selmic, Polymer Photodetectors Based on MEH-PPV and Ethyl Viologen Dibromide (in submission).
6. Difei Qi, Kody Varahramyan, and Sandra Selmic, Fabrication and Photoelectrical Characteristics of Polymer-Organic-Blend Photodetectors, *Mat. Res. Soc. Symp. Proc.* v. 814, n I11.7.1-7.6, 2004.
7. Difei Qi, Jie Liu, and Sandra Selmic, Fabrication and Characterization of Conjugated Polymer Solar Cells Based on MEH-PPV and PCBM, *Environmental State of the State Conference IX.*

Reproduced with permission of the copyright owner. Further reproduction prohibited without permission.